FIBRE-OPTIC MICRORESONATORS AND SENSOR SYSTEMS

N.A.D. Stokes

Submitted for the degree of Ph.D.
University College, London
January, 1990

ProQuest Number: 10609966

All rights reserved

INFORMATION TO ALL USERS
The quality of this reproduction is dependent upon the quality of the copy submitted.

In the unlikely event that the author did not send a complete manuscript
and there are missing pages, these will be noted. Also, if material had to be removed,
a note will indicate the deletion.

ProQuest 10609966

Published by ProQuest LLC (2017). Copyright of the Dissertation is held by the Author.

All rights reserved.
This work is protected against unauthorized copying under Title 17, United States Code
Microform Edition © ProQuest LLC.

ProQuest LLC.
789 East Eisenhower Parkway
P.O. Box 1346
Ann Arbor, MI 48106 – 1346

Abstract

This thesis is concerned with the theoretical and experimental investigation of fibre-optic microresonators and sensor systems. Fibre-optic microresonators combine the advantages of resonator sensors and fibre-optics by using microfabricated silicon-based vibrating elements.

First the methods of microresonator fabrication are outlined, and a number of devices which have been fabricated in-house are described. Some significant features, which are expected to effect device performance, are also identified. The resonant behaviour of the microbeams is considered. Their response under the influence of a modulated exciting optical beam from a fibre-optic link is derived, and fabrication-induced effects are analysed. A two-source fibre-optic system is developed and the devices examined experimentally using this system. The response of both metal-coated silicon dioxide and metal-coated silicon microresonators is compared with the predicted behaviour.

The theory of the temperature and pressure dependences of the resonance frequencies of microresonator beams is developed. The effects of applied pressure and of a change in temperature on both metal-coated silicon dioxide and metal-coated silicon devices are examined using the two-source fibre-optic system. These experimental results are compared with the predictions and conclusions drawn regarding the suitability of the devices for different sensing applications.

A fibre-optic system for the activation and detection of the microresonator vibrations incorporating a single, unmodulated optical source is proposed. A possible mechanism for self-excitation of microbeams is described, and conditions for sustaining these vibrations are defined. Self-excitation of microbeams is demonstrated using such a system. The temperature variation of resonance frequency of a self-excited microresonator is measured, and two self-excited devices are multiplexed on a single-source fibre-optic system.

To my Mother and Father, Jill and Peter Stokes

Acknowledgements

I wish to express my special thanks to Dr Shalini Venkatesh for her enthusiasm and for all the encouragement she gave me.

I also wish to thank:
Dr.Mick Flanagan for his help and passionate discussions;
Dr.Gareth Parry for his support and optimism;
Rebwar Fatah for his collaboration, and for reminding me what is important;
and all my friends who have been good to me.

Thank-you BOC Healthcare, Schlumberger Industries and the SERC for financial support during this work.

CONTENTS

Contents	1
Glossary of Variables	4
Glossary of Abbreviations	5
Chapter 1: Introduction and General Review	6
1:1 Resonator sensors	7
1:2 Optically Powered Resonators	8
1:3 Fibre-Optic Sensors	9
1:4 Silicon Microfabrication	10
1:5 Electrical Microresonator Sensors	11
1:6 Optically Powered and Fibre-Optic Microresonators	12
1:7 The Need for Fibre-Optic Microresonators	15
1:8 Objectives of This Research Programme	17
References for Chapter 1	18
Chapter 2: Fabrication of Microresonators	21
2:1 Introduction	22
2:2 Beam Fabrication Techniques	23
2:2.1 Photolithographic Patterning	23
2:2.2 High Density Doping	24
2:2.3 Anisotropic Etching	26
2:2.4 Metal Coating Techniques	28
2:3 Consideration of Silicon Dioxide Beams	29
2:4 Devices Fabricated for this Project	32
2:4.1 Devices Fabricated In-House	32
2:4.2 Devices Fabricated Externally	35
2:5 Results of the Fabrication Programme	36
2:6 Conclusions	45
References for Chapter 2	46

Chapter 3: Analysis of Microresonator Vibrations 49
3:1 Introduction 50
3:2 Theory of Beam Resonance 51
3:2.1 Resonance Frequencies of Transverse Flexural Mode 51
3:2.1.1 Simple Beams 52
3:2.1.2 Beams with a wider central area or wings 53
3:2.1.3 Effect of Tension 54
3:2.1.4 Adjusting for Composite Strips 54
3:2.2 Resonance Frequencies of Torsional Modes 55
3:2.3 Quality Factor 55
3:3 Optical Excitation of Microresonators 56
3:3.1 Theory of Opto-Thermal Conversion of Energy 57
3:3.1.1 Consideration of Optical Loading 57
3:3.1.2 Steady Component of the Incident Light 59
3:3.1.3 Oscillatory Component of the Incident Light 62
3:3.1.4 Consideration of Quality Factors 67
3:4 Fabrication-Induced Effects in Microfabricated Devices 69
3:4.1 Fabrication-Induced Stress 69
3:4.1.1 Deflection of a Bent Beam 70
3:4.1.2 Stress in a Deflected Beam 71
3:4.2 Etch-Defined End Conditions 75
3:5 Conclusions 76
References for Chapter 3 77

Chapter 4: Observation of Microresonator Vibrations 78
4:1 Introduction 79
4:2 Experimental Methods 80
4:2.1 Two-Source Fibre-Optic System 80
4:2.2 Fibre-Optic System with Pigtailed Source 82
4:2.3 Phase-Lock System 83
4:3 Vibrational Characterisation 86
4:3.1 Detection and Activation Power 86
4:3.2 Silicon Dioxide Microresonators: Mode Relationships 90
4:3.3 Variation of Resonance Frequency with Beam Length 99
4:3.4 Variation with Metal Thickness 101
4:3.5 Silicon Microresonators: Mode Relationships 105
4:3.6 Consideration of Quality Factors 109
4:4 Electrical Excitation 111
4:4.2 Capacitive Drive 111
4:4.2 Resistive Drive 113
4:5 Conclusions 114
References for Chapter 4 115

Chapter 5: Pressure and Temperature Sensitivities of Microresonators 117
5:1 Introduction 118
5:2 Analysis 120
5:2.1 Effect of Applied Pressure 120
5:2.2 Effect of Change in Temperature 124
5:3 Experimental Method 128
5:4 Experimental Results 130
5:4.1 Effect of Applied Pressure 130
5:4.1.1 Silicon resonators 130
5:4.1.2 Silicon dioxide resonators 134
5:4.2 Effect of Change in Temperature 137
5:4.2.1 Silicon resonators 137
5:4.2.2 Silicon dioxide resonators 139
5:5 Discussion 141
5:5.1 Effect of Applied Pressure 141
5:5.2 Effect of Change in Temperature 142
5:6 Conclusions 146
References for Chapter 5 147

Chapter 6: Self Excitation of Microresonators 148
6:1 Introduction 149
6:2 Analysis 150
6:2.1 Mechanism of self-excitation 150
6:2.2 Conditions for self-excited vibrations 153
6:3 Experimental Method 155
6:4 Experimental Results 157
6:4.1 Initial observation of self-excitation 157
6:4.2 Further observations 158
6:4.3 Temperature variation of frequency 164
6:4.4 Multiplexing of self-excited devices 165
6:5 Conclusions 167
References for Chapter 6 168

Chapter 7: Summary, Conclusions and Recommendations 169
References for Chapter 7 174

Appendix A: Materials data 175
Appendix B: Publication List 176

Glossary of Variables

A	*cross-sectional area*
a	*beam thickness*
b	*beam width*
C	*torsional constant; material/geometrical constant; specific heat capacity*
c, c'	*constants*
D	*mean separation between fibre end and beam surface*
d	*separation between fibre end and beam surface; diaphragm thickness*
E	*Young's modulus*
e	*shape factor*
F	*interferometer finesse*
f	*frequency; resonance frequency*
G	*torsional modulus*
H	*stress parameter*
h	*dimensionless stress parameter*
I	*second moment of area*
I_p	*polar moment of area*
i	*mode number*
K	*absorption index*
k	*thermal conductivity*
L	*beam length (distance between beam supports)*
M	*mass*
m	*modulation depth*
n	*integer value*
P	*pressure; power*
Q	*quality factor; heat*
R	*damping constant; diaphragm radius*
r	*disc radius; distance from diaphragm centre; coefficient of reflectivity*
S	*extended beam length*
s	*element of distance along beam length*
T	*temperature*
t	*time*
w	*wafer thickness*
x	*distance co-ordinate along beam length (in the plane of the wafer)*
y	*distance co-ordinate perpendicular to wafer surface*
$z_{therm.}$	*thermal diffusion length*

...continued over

α	*linear thermal expansivity*
β	*absorption coefficient*
Δ, Δ'	*central deflection of beam; effective deflection*
Δ_0	*deflection at equilibrium*
ε	*strain*
η	*viscosity*
Θ	*temperature coefficient of Young's modulus*
κ	*thermal diffusivity*
λ	*wavelength*
ν	*Poisson's ratio*
ρ	*density*
σ	*stress; mean stress*
σ_A, σ_B	*magnitude of fabrication-induced stresses*
Φ_i	*dimensionless end-condition parameter*
χ	*curvature*
Ψ	*intensity*
ω	*angular frequency*

Glossary of Abbreviations

CAD	computer aided design
LRU	line replacable unit
PC	phase comparator
S	phase shifter
SEM	scanning electron microscope
SNR	signal-to-noise ratio
UCL	University College, London

CHAPTER 1: INTRODUCTION AND GENERAL REVIEW

1:1 Resonator Sensors

1:2 Optically Powered Resonators

1:3 Fibre-Optic Sensors

1:4 Silicon Microfabrication

1:5 Electrical Microresonator Sensors

1:6 Optically Powered and Fibre-Optic Microresonators

1:7 The Need for Fibre-Optic Microresonators

1:8 Objectives of This Research Programme

References for Chapter 1

CHAPTER 1:

INTRODUCTION AND GENERAL REVIEW

1:1 Resonator Sensors

Sensors are an essential part of all measurement and control systems, for which steady growth is predicted in the performance-sensitive markets of process control, military/aerospace and medical applications. Although the specific sensor requirements vary widely between these different industrial sectors, in many reviews the common need for sensors which are compatible with digital control systems, as well as being low-cost and reliable, is emphasised [1].

In the past sensors have been developed based on the measurement of analogue electrical parameters. These are not inherently suitable for digital control because they require an added analogue-to-digital conversion stage which increases the system complexity and cost. The development of sensors giving an intrinsically digital output is thus of major interest. One approach to this is to use resonators.

The principle behind resonator sensing is that the natural frequency of vibrations of a mechanical structure may be allied to an external parameter affecting the structure. Using a pulse counter to measure the resonant frequency provides an output related to that parameter which can be directly transmitted to a digital signal processor. Furthermore the frequency, being essentially determined by the mechanical and material properties of the vibrating structure, is insensitive to the electrical characteristics of the drive and detection circuitry.

Since about 1960 development has progressed on a range of such frequency-based sensors. Typically the stress in the resonator is applied to a bending beam or a pressure diaphragm. Alternatively the effective mass or inertia of the structure may be changed, for example by immersing it in a liquid or gas [2]. Altogether a wide range of parameters may be measured including viscosity [3], density [4], liquid level [5,6], temperature [7], pressure [8] and fluid flow [9].

There is one further characteristic of resonator sensors which is important for their practical application. They can be driven by relatively low power sources, since a vibrating device at resonance requires only enough power to overcome losses.

1:2 Optically Powered Resonators

Crystal quartz has been a commonly used material for resonators since it has highly stable elastic properties and is piezoelectric so that vibrations may be maintained by a simple electrical drive applied to a suitably arranged pair of electrodes [2]. The amplitude of vibrations may be detected by monitoring a second pair of electrodes so that the resonant frequency of the quartz structure can be tracked. Recently there has been some interest in avoiding direct electrical connection between the electrodes and the drive and detection circuitry and a system using fibre-optic links has been described [10] and is shown in figure 1.1.

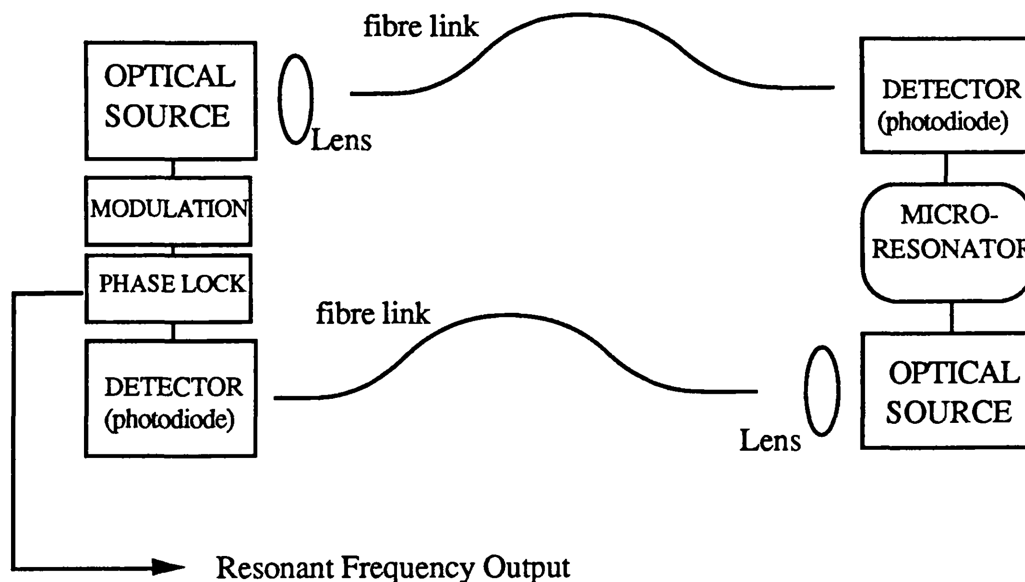

Figure 1.1: System for an Electrically Isolated Resonator Sensor.
(see [10])

In this system the electrical signals are converted to optical form at the fibre ends by using appropriate optical sources, and photodiodes are used to reconvert the received optical signals to electrical form. This low-powered sensor is thus electrically isolated. Further progress has been made suggesting commercially viable systems of this sort [11] but the mechanism of inducing vibrations of the resonator structure remains electrical.

The first presentation of optical activation of vibrations was made in 1981 [12]. A circular silicon membrane coated with black paint was driven into vibration by an unguided modulated optical beam of a few milliwatts. The moving membrane periodically blocked a second beam which was used to detect the vibrations. Subsequently a similar system was used to excite some simple metal-coated quartz devices [13], again using power levels of a few milliwatts. Here the vibrations were detected by the voltage piezoelectrically induced between two electrodes. Although no attempt was made to design or develop a system for sensing, these results demonstrated the feasibility of using optical power to drive the vibrations of simple resonator elements, and suggested the development of fibre-optic resonator sensors.

1:3 Fibre-Optic Sensors

Since the advent of the optical fibre in the field of high data-rate communications ten years ago much research effort has been directed at using optical fibre systems for the sensing of various physical quantities. It has been found that for many applications, without being inherently more costly, such system offer significant potential advantages over their electrical equivalents [14]. These include immunity to electromagnetic interference - important if the sensor is to be used in the vicinity of other, electrical, equipment - and intrinsic safety, which may be vital if the environment is hostile [15].

A wide range of techniques has been explored for both intrinsic and extrinsic sensors using all possible modulation methods and a number of devices developed based on the measurement of intensity, wavelength and polarization. The problems of fabrication and packaging to produce robust sensors are gradually being overcome

but there is still little penetration of fibre-optic sensors into the market. This is partly the result of the sensitivity of all intensity-based systems to variations in the performance of the source, detector and fibre link, caused by source, detector or component drifts, or to environmental perturbations. This may be counteracted by various referencing or calibration methods, but these increase the complexity of the system and only in very few cases have successful systems been produced [1].

There is thus potential in combining the resonator and fibre-optic sensor technologies by the development of an interrogated mechanical resonator. Such an approach neatly avoids the problems of instability associated with fibre-optic sensors since the absolute intensity of the output signal is not important. To fully exploit the advantages of optical sensing it is necessary to use direct optical activation as well as detection of vibrations, best achieved by attaching the device directly onto a fibre end. However, such a device, able to be sustained in oscillation by optical power, needs to be extremely small, ideally with the length of the vibrating element less than the outer diameter of the fibre - typically a few hundred microns. This requirement may be met using silicon microfabrication techniques.

1:4 Silicon Microfabrication

Since silicon revolutionised the electronics industry its properties and those of its compounds have been extensively researched. The exploitation of silicon's electrical properties has lead to the development of a range of processing methods including oxidation techniques, photolithography, dopant implantation and diffusion, chemical etching techniques and metallisation, which allow the microfabrication of devices reliably and in large numbers. More recently these methods have been borrowed for the fabrication of mechanical devices comparable in size with the electronic ones [16]. Structures have been made which range from a simple strip [17] to an entire gas chromatograph fabricated on a single silicon wafer [18]. Details of silicon microfabrication techniques are described in Chapter 2.

These technologies enable the fabrication of silicon-based resonator sensor heads with dimensions compatible with optical fibres, and capable of being driven into

vibration by reasonably low levels of optical power, and allow the costs of these microsensors to be kept relatively low.

1:5 Electrical Microresonator Sensors

Initially the silicon fabrication technology developed for the microelectronics industry was used to develop electrically powered miniaturised sensors. The first such microresonator was proposed in 1981 [19] and subsequently developed as a pressure sensing element with a frequency output [20, 21]. This consisted of a free-standing silicon resonator plate suspended above a diaphragm fabricated from the same silicon wafer, so that pressure changes across the diaphragm strained the plates and changed their characteristic resonance frequency. The device was excited by applying a drive signal across electrodes deposited on a glass substrate mounted parallel to the resonator, as shown in figure 1.2. Vibrations were detected by monitoring the change in capacitance between the resonator and the electrodes, and the system could be maintained at resonance by electrical feedback.

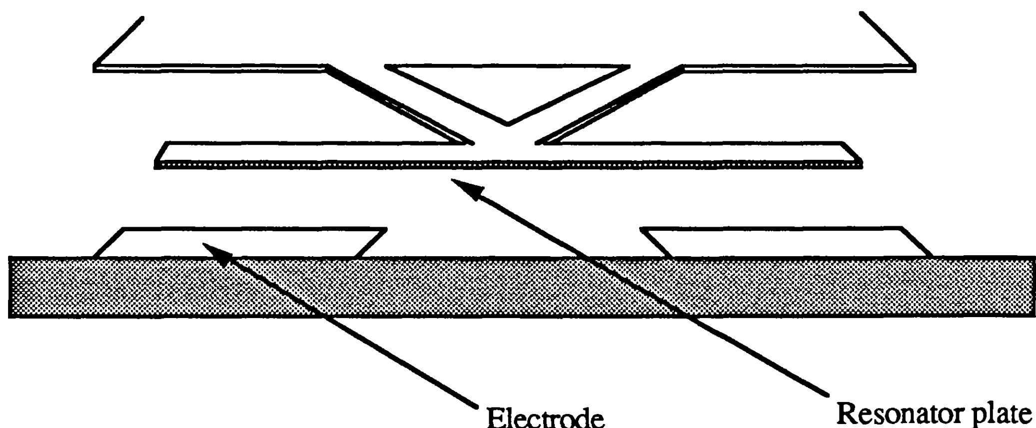

Figure 1.2: Cross-section of electrostatically excited silicon microresonator. (see [20])

A variety of devices with dimensions of the order of 100μm have been developed using electrostatic, piezo-electric or electrothermal mechanisms of excitation and electrical detection, including silicon accelerometers [22] and chemical sensors [23].Recently a strain gauge has been designed as a torsionally vibrating silicon paddle sustained in vibrations by magnetic induction forces which could maintain itself at resonance by reflecting some part of a light beam from the paddle itself onto a photodiode whose output controlled the activating magnetic field [24].

These devices have not only attracted interest from the transducers market themselves but also paved the way for optically powered microresonators to follow.

1:6 Optically Powered and Fibre-Optic Microresonators

Most published results in this area are simply of resonance without any sensing action. The first experimental measurements to be made on optically powered microresonators were reported in 1985. These were carried out by Venkatesh *et al.* at Strathclyde University [25,26]. The system used is shown in figure 1.3.

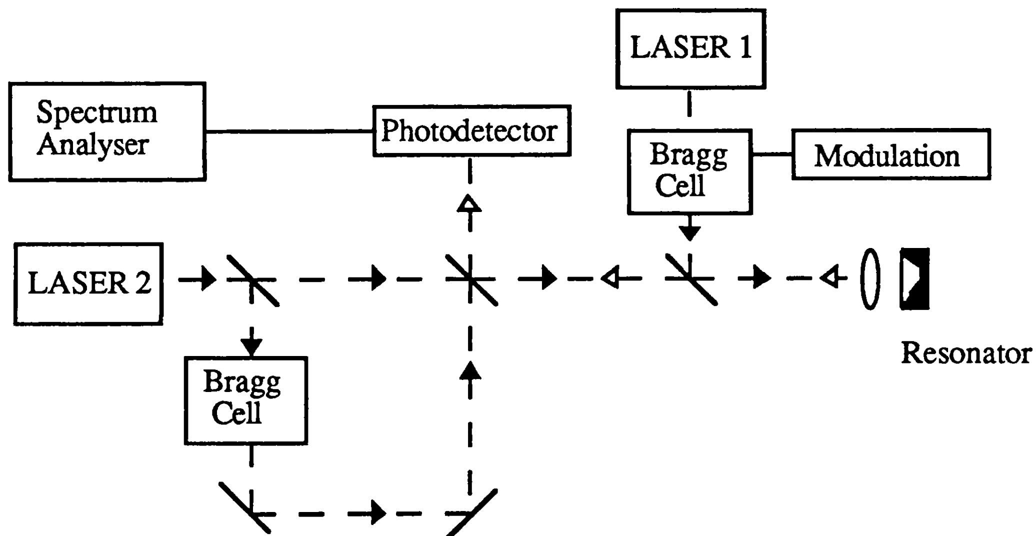

Figure 1.3: Bulk optical resonator system. (see [26])

A 1μm thick strip of metal-coated silicon dioxide approximately 200μm long and 5μm wide was maintained in flexural vibrations by a few tens of microwatts of optical power directed onto its surface from an intensity modulated laser. The response of the strip was detected using an interferometric technic technique involving a second laser.

Since then several research groups have worked on this type of system. In 1986 at Surrey University a partially fibre-optic system was used with the silicon plate microresonator shown in section above (figure 1.2) [27]. Laser pulses of approximately 1 milliwatt were guided by a multimode fibre and focused onto the resonator surface, and vibrations detected using an interferometric optical fibre technique employing a second, single-mode fibre [28]. The positions of the activating and probe beams could be independently adjusted under observation so that the modes could be studied in detail. It was demonstrated that the complex type of resonator structure used did not enable the most efficient possible optical activation.

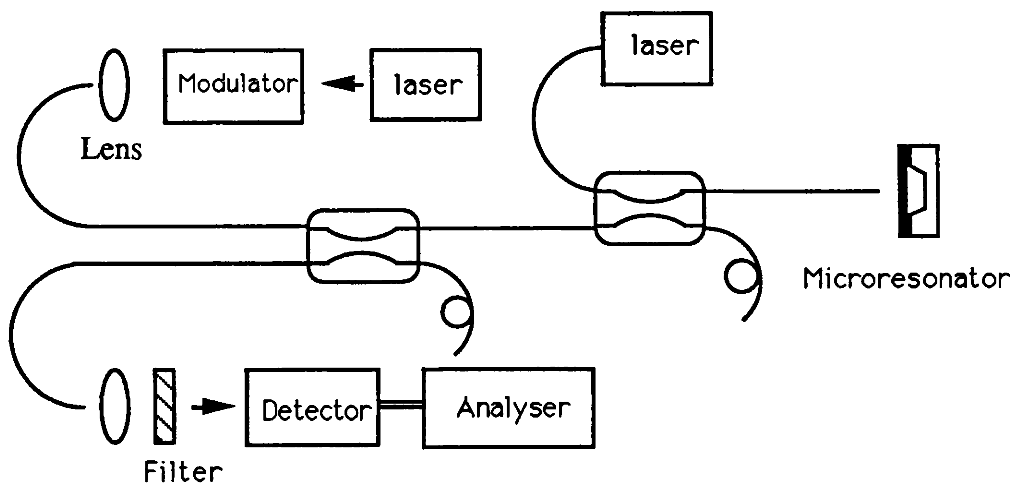

Figure 1.4: Single-mode Fibre-optic System for Activation and Detection of Vibrations.

The first *all fibre-optic* system was described in 1986 by the group at University College London [29]. This was an all-single-mode-fibre system in which the drive and probe beams were directed onto the resonator surface from a single fibre, allowing the sensor head to be particularly small. The system is shown in figure 1.4.

In 1987 a group at Strathclyde were working on a bulk optical system to demonstrate the sensing capabilities of optically activated silicon microresonators. They have used a similar system to that shown in figure 1.3 to excite aluminium coated diaphragms a few microns thick and less than 1mm across, and shown that, as predicted by simple theory, the resonant frequencies of these devices vary with temperature [33]. At the University of Twente silicon diaphragms of similar dimensions have been developed as fibre-optic pressure and force sensors. These used three multimode fibres lying in grooves in the planes of the wafers in which the microstructures were realised, rather than being perpendicularly directed at the wafer surface [34]. They succeeded in demonstrating that fibre-optic sensing systems could be designed using vibrating mechanical microstructures. At Strathclyde results were published in 1987 showing a shift in resonant frequency of a 2.5μm thick silicon beam attached to a 65μm silicon diaphragm with pressure of 0.02% per millibar, although unguided light was used for excitation and detection [35]. This is the largest shift observed with such a device.

In 1986 it became clear to the group at University College, London, that for the practical development of fibre-optic micro resonators it was important first to improve the activation and detection schemes. Subsequently a detailed experimental characterisation of the vibrations of microbeams could be made.

It became evident that if the beams could maintain themselves at resonance by means of optical feedback within the sensor itself the fibre-optic system could be greatly simplified. This technique, known as *self-excitation*, would also allow the multiplexing of several sensors without having to input a different modulation frequency for each one. While experimental work was being carried out towards this aim at U.C.L., the development was formally proposed independently by Langdon *et al.* [36]. Experiments on polyester cantilevers approximately 10mm long were reported in which vibrations were excited for very short periods, using an incident

optical power of about 1 milliwatt; however they were unable to sustain optical self-excitation in micromechanical devices.

1:7 The Need for Fibre-Optic Microresonators

In considering the developments described above, the framework of a significant research programme was beginning to emerge. However, before starting on such a programme, it was desirable to identify the needs for fibre-optic microresonators.

The future of the field looks extremely promising with great interest being expressed in sensor applications of silicon-based fibre-optic micromechanical resonators [37]. They are an attractive option for the measurement of a range of parameters. Particular stress has been placed on pressure-sensing applications because there is such a broad market. In the automotive market fibre-optic sensor systems offer significant advantages over conventional electrical systems for measuring pressure and temperature, and are considered to have the best potential for satisfying the high integrity requirement for 'intelligent' closed-loop engine management systems [38]. The increased complexity of automobile control has created a need for sensors which have a high performance in environments where they may be exposed to large variations in temperature, road dirt, ice and oil, which have a long lifetime and are protected against electrical transients [39].

In aero-engine (and airframe) applications there is already considerable investment in this field. The sensor environment is particularly hostile with temperatures ranging from -60 to +250 ^{0}C, and vibrations of typically 5g up to around 2000Hz. Accuracy and temperature stability requirements are also particularly tight up to pressures of around 70 bar, see table 1. The sensor head must be a line replaceable unit (LRU), and a technique is required which allows the multiplexing of a number of sensors into a single opto-electronics package.

An application with very different requirements is that of an arterial pressure monitor. In this case the accuracy and stability requirements are not so tight, but the sensor heads must be cheap since they would probably be disposable. A fibre-based sensor

is particularly attractive for central venous catheter introduction and subcutaneous channelling because of the small diameter (less than 0.5mm) and flexibility of an optical fibre.

There is increasing interest in transmission-line neutral fibre-optic sensors whose optical output signal is not affected by loss effects on the signal transmission lines [31]. For downhole measurement of temperature and pressure in a producing oil well, transmission line neutrality is crucial and measurements have to be made over distances up to 20km. Temperature must be measured over a range of 0 to 200^{0}C to within an accuracy of $\pm 1^0$C. Oil company internal reports, not available for general circulation, indicate that this is not currently achievable and that the benefits of developing a device of this accuracy for remote operation would be considerable.

Magnetic and electric field sensors can be constructed from microresonators, by using magnetostrictive materials, so that the stress in the structure becomes a function of the field. This may be done by directly sputtering metallic glasses onto the surface of the silicon or silicon dioxide resonators [40]. Gravimetric sensors can also be considered since extremely small variations in the mass of the low mass microstructures should be detectable [41]. These variations may be effected by adsorption on the resonator surface, or temperature changes of the resonator may be brought about by catalytic combustion of oxidisable gases. Such devices may be the basis of gas-detection, biological and chemical sensors.

A number of practical problems have yet to be solved before these ideas can be implemented in practical systems, in particular the necessity for temperature compensation schemes, and that of bonding the silicon-based sensor heads onto optical fibres. Very little has been published directly relevant to these requirements [42] but since they are of commercial importance as well as technical interest, it is expected that effort will be directed in these directions as the development of fibre-optic microresonator sensors draws closer to fulfillment.

1:8 Objectives of This Research Programme

In view of the wide range of possible applications which we have discussed in the previous section, a programme of research was set up directed towards examining the underlying principles and limitations of fibre-optic microresonators, and towards determining the suitability of these devices for development in some of these applications. The project objectives were therefore as follows:

1. To establish a straightforward procedure for the design and fabrication of metal coated silicon dioxide microresonator devices encorporating beams between 80μm and 250μm long, using readily available oxidised silicon wafers in a class 100/10,000 clean-room environment.

2. To identify any features peculiar to these micron-scale resonators, and to predict how these might effect the device performance.

3. To develop the theory of microresonator vibrations and thus to suggest hypotheses of sensor operation which could be tested experimentally.

4. To carry out experiments using different types of microresonator - differing by dimensions, configurations, and materials - to test the above hypotheses and to establish the magnitudes of the principal parameters.

5. To examine the sensors experimentally in their role as pressure and temperature measurement devices, and to determine their suitability for development in these roles.

6. To identify whether operation of the sensors could be simplified by using a single source for driving the sensor and measuring its response and, if so, to explore the features of this type of operation.

References for Chapter 1

1. G.R. Jordan; "*Sensor Technologies Of The Future*"; J.Phys.E.: Sci.Instrum, Vol. 18, pp729-735, 1985
2. R.M. Langdon; "*Resonator Sensors - A Review*"; J.Phys.E.: Sci.Instrum., Vol. 18, pp103-115, 1985
3. G.J. Beukema & J.Mellama; "*Measuring System For Complex Shear Modulus Of Liquids Using Torsionally Vibrating Quartz Crystals*"; J.Phys.E.: Sci.Instrum., Vol.14, pp418-420, 1981
4. B.W. Balls; "*A New On-Line Density Meter For Viscous Liquids And SlurriesI*"; ISA Trans., Vol.20, No.3, pp67-75, 1981
5. R.M. Langdon; "*Vibrating Transducers In Measurement*"; The Chemical Engineer Vol.397, pp33-35, 1983
6. N.S. Ageeva; "*Ultrasonic Method For Measuring The Height Of The Fluid Level In A Vessel By Means Of Flexural Oscillations Of A Thin Elastic Strip*"; Sov.Phys.-Acoust. Vol.6, pp16-17, 1960
7. U. Priess; "*Quartz Detectors For High Resolution Temperature Meaurement*"; Toute Electronique, Vol.485, pp60-62, 1983
8. E.N. Kauffman; "*Pressed By Pressure Measurements?*"; Instruments and Control Systems, Vol.47-Aug, pp53-54, 1974
9. G. Macdonald; "*A Vibrating Vane Mass Flowmeter*"; European Conf. on Sensors and their Applications, Manchester, 1983, pp58-59
10. S.M. McGlade *et al.*; "*An Optically Powered Vibrating Quartz Force Sensor*"; The GEC J. of Research, Vol. 2, pp135-138, 1984
11. R.C.Spooncer *et al.*; "*A Pulse Modulated Optical Fibre Quartz Temperature Sensor*"; Proc. SPIE Conference on Fibre-Optic Sensors II, The Hague, pp137-141, 1987
12. E. Dieulesaint *et al.*; "*Mechanical Excitation Of A Membrane By An Optical Beam*"; Proc. IEEE Ultrasonic Symposium, IEE New York, pp802-805, 1981
13. E. Dieulesaint *et al.* ; "*Optical Excitation of Quartz Resonators* ; Electronics Lett., Vol.18, pp381-382, 1982
14. T.G. Giallorenzi *et al.* ; "*Optical Fibre Sensor Technology*"; IEEE J. Quantum Electron., Vol.QE-18, No.4, pp626-665, 1982

15. J.P. Dakin; "*Optical Fibre Sensors - Principles And Applications*"; Proc. SPIE, vol. 374, pp172-177, 1983

16. K.E. Peterson; "*Silicon As A Mechanical Material*"; Proc. IEEE, Vol.70, pp420-457, 1982

17. S. Venkatesh *et al.*; "*Optically Activated Resonator Sensor*"; Proc. SPIE conference on Fibre Optic and Laser Sensors III, San Diego, pp110-113, 1985

18. S.J.B.Terry; "*A Gas Cromotography System Fabricated On A Silicon Wafer Using Integrated Circuit Technology*"; Ph.D Thesis, Stanford University, Technical Report No.4603-1, 1975

19. J.C. Greenwood; 1987 British Patent No. 1 588 669 (filed 1977, pub.1981)

20. J.C.Greenwood; "*Etched Silicon Vibrating Sensor*"; J.Phys.E.: Sci.Instrum., Vol.17, pp650-652, 1984

21. J.C. Greenwood; "*Resonant Silicon Sensors at STL* ; Abstracts of Eurosensors, 3rd Conf. on Sensors and their Applications, Cambridge, 1987, pp14-15

22. W. Benecke *et al.* ; " *A Frequency Selective, Piezo-Resistive Silicon Vibration Sensor*"; Proc. Int. Conf. on Solid State Sensors and Actuators - Transducers '85, Boston, 1985, pp105-108

23. R.T. Howe *et al.* ; "*Integrated Resonant Microbridge Vapour Sensor*"; Tech. Digest IEEE Inst. Electron Devices Meeting, San Francisco, 1984, pp213-216

24. J.M. Naden *et al.* ; "*An Optically Addressed Silicon Strain Sensor*"; Abstracts of Eurosensors, 3rd Conf. on Sensors and their Applications, Cambridge, 1987, pp16-17

25. S. Venkatesh et al.; "*Optically Activated Vibrations In A Micromachined Silica Structure*"; Electronics Lett. Vol. 21, pp 315-317, 1985

26. S. Venkatesh *et al.* ; "*Optically Activated Resonator Sensors*"; Proc. SPIE conference on Fibre Optic and Laser Sensors III, San Diego, pp 110-113, 1985

27. M.V. Andres *et al.* ; "*Optical Activation Of A Silicon Vibrating Sensor*"; Electronics Lett., Vol.22, pp1097-1099, 1986

28. M.V. Andres *et al.* ; "*Analysis of An Interferometric Optical Fibre Detection Technique Applied To Silicon Vibrating Sensors*"; Electronics Lett., Vol.23, pp952-954, 1987

29. S. Venkatesh *et al.*; "*Fibreoptic Detection Of Optothermal Vibrations*"; Technical Digest of OFS '86, Tokyo, PD-2 - PD-5, 1986

30. S. Venkatesh *et al.* ; "*Mechanical Resonators In Fibre-Optic Systems*"; Optics Lett., Vol.12, pp129-131, 1987
31. H. Wolfelschneider *et al.*; "*Optically Excited And Interrogated Micromechanical Silicon Cantilever Structure*"; Proc. SPIE Conf. on Fibre-Optic Sensors II, The Hague, 1987, pp61-66
32. W. Benecke *et al.* ; "*A frequency-Selective, Piezoresistive Silicon Vibration Sensor*"; Proc. Int. Conf. on Solid-State Sensors and Actuators - Transducers '85, Boston, June 1985, pp105-108
33. K.E.B. Thornton *et al.*; "*Temperature Dependance Of Resonance Frequency In Optically Excited Diaphragms*"; Electronics Lett., Vol.22, pp 1232-1234, 1987
34. T.S.J. Lammerink *et al.* ; "*Fibre-Optic Sensors Based On Resonating Mechanical Structures*"; Proc. SPIE Conf. on Fibre-Optic Sensors II, The Hague, 1987, pp67-71
35. D. Uttamchandani *et al.*; "*Optically Excited Resonant Diaphragm Sensor*"; Electronics Lett. Vol. 23, pp 1333-1334, 1987
36. R.M. Langdon *et al.* ; "Photo-acoustic Oscillator Sensors"; Proc. SPIE Conf. on Fibre-Optic Sensors II, The Hague, 1987, pp86-93
37. G.D. Pitt *et al.* ; "Optical Fibre Sensors"; IEE Proc. J. Optoelectron., vol.132, pp214-248, 1985
38. R.T.Murray *et al.*; "Fibre-Optic Sensors For Automobiles"; I.Mech.E., 5th International CVonf. on Automotive Electronics, 1985, pp337-342
39. J.R. Mastroianni; "*Automotive Applications Of Silicon-Based Sensors*"; I.Mech.E., 5th International CVonf. on Automotive Electronics, 1985, pp317-323
40. S. Tyagi *et al.* ; "*Characterisation Of Highly Magnetostrictive Metallic Glass Coatings*"; J.Appl.Phys., Vol.57(1), 1985, pp3496-3498
41. M. Johnson; "*Optical Powering Techniques For Microstructure Fibre Sensors*"; Proc. Fibre Optic Communications & Local Area Networks Exposition - EFOC/LAN, 1988, pp219-222
42. S. Venkatesh; "*Optical Microresonator Sensor Systems*"; J.IERE, Vol.58, no.5 (Supplement), ppS79-S84, 1988

CHAPTER 2:
FABRICATION OF MICRORESONATORS

2:1 Introduction

2:2 Beam Fabrication Techniques
- 2:2.1 Photolithographic Patterning
- 2:2.2 High Density Doping
- 2:2.3 Anisotropic Etching
- 2:2.4 Metal Coating Techniques

2:3 Consideration of Silicon Dioxide Beams

2:4 Devices Fabricated for this Project
- 2:4.1 Devices Fabricated In-House
- 2:4.2 Devices Fabricated Externally

2:5 Results of the Fabrication Programme

2:6 Conclusions

References for Chapter 2

CHAPTER 2

FABRICATION OF MICRORESONATORS

2:1 Introduction

It was thought that advantage might arise during the course of this project by allowing scope for changing the specification of the devices used as the work proceeded, in the light of early results. To avoid the long lead times associated with outside suppliers, and in order to obtain the modified structures rapidly, most of the devices used on this project were manufactured in-house at U.C.L. using the clean-room and associated facilities there. By adopting this procedure I was able to control the complete process of design, manufacture from standard oxidised silicon wafers, and experimentation.

This chapter describes the principles involved in the manufacture of silicon and silicon dioxide devices. First we discuss the commonly used microstructure fabrication techniques and describe general processes, and those used outside U.C.L. to fabricate the silicon beams used as part of this project. We describe the procedures used in the fabrication of silicon dioxide beams in-house at U.C.L., including an outline of the metal-coating techniques.

The resulting structures which were subsequently used in the experimental phase of the programme are described in this chapter. We also identify some features of the devices which we predict will effect their behaviour, and compare the silicon devices fabricated for this project.

2:2 Fabrication Techniques

2:2.1 Photolithographic Patterning

High quality silicon crystals and precise photolithographic methods of patterning the crystal surfaces are now available, and etching techniques have been studied which allow the precise fabrication of silicon devices on the scale of microns. Specific areas of research exploiting this capability have included preparation of thin silicon membranes [1-3], development of integrated circuit technology [4-6], X-ray mask formation [7] and fabrication of electromechanical devices [8] amongst a wide variety of active and passive three-dimensional structures.

Currently used silicon microfabrication methods begin with photolithography, which transfers copies of a photographically reduced pattern onto a wafer surface. The process involves the use of a glass plate or mask onto which the pattern has been printed in metal opaque to ultraviolet radiation. A thin layer of a photosensitive organic polymer known as a photoresist is deposited onto the wafer surface, which is then exposed to ultraviolet radiation through the mask. The mask is commonly kept in contact with the coated surface - and the process is then known as surface contact photolithography. The ultraviolet radiation affects the solubility of the exposed areas of photoresist, weakening it if it is a *positive* photoresist or strengthening if it is a *negative* photoresist. The irradiated wafer is rinsed in a developing solution which removes the more soluble areas. The remaining photoresist is hard baked and acts as a protecting mask for etching the substrate.

To form a three-dimensional structure from a wafer pattern in this way the silicon substrate must be etched in a well-controlled manner. The principal shaping methods which have been explored are high-density doping followed by anisotropic etching; and growth or deposition of another material onto the wafer surface followed by anisotropic etching.

2:2.2 High Density Doping

High density doping involves infusing areas of the silicon wafer with a high level of impurity atoms. At sufficiently high doping levels - about 10^{20} atoms cm^{-3} - the solubility of silicon in certain etch solutions is drastically reduced [9,10]. For example, silicon doped with boron (p-type) at concentrations of about $5x10^{19}cm^{-3}$ is insoluble in an ethylene diamine/pyrocatechol/water etch [9,11]. This allows three-dimensional structures, such as beams, to be defined, since by using boron doping the etch may be stopped at a predetermined point.

A common fabrication method involves the definition of the areas to be doped by the selective photoresist masking. An example of this method is shown in figure 2.1. Free-standing structures are formed by anisotropic etching of the undoped silicon as described below in section 2:2.3 [12].

The required level of doping can be reduced if an electrical bias is applied to the wafer. In this case different parts of the silicon are doped p-type and n-type they may be effectively insulated from one another, held at different potentials and etched at different rates [13]. However the anisotropic electrochemical etch-stops are more difficult to use than the boron etch-stop and are not as yet widespread.

It should be noted that this method of microfabrication puts the silicon under stress. In silicon highly doped with boron the silicon is put under tension [14] since the boron atoms, which enter the silicon lattice substitutionally, are smaller than the silicon atoms.

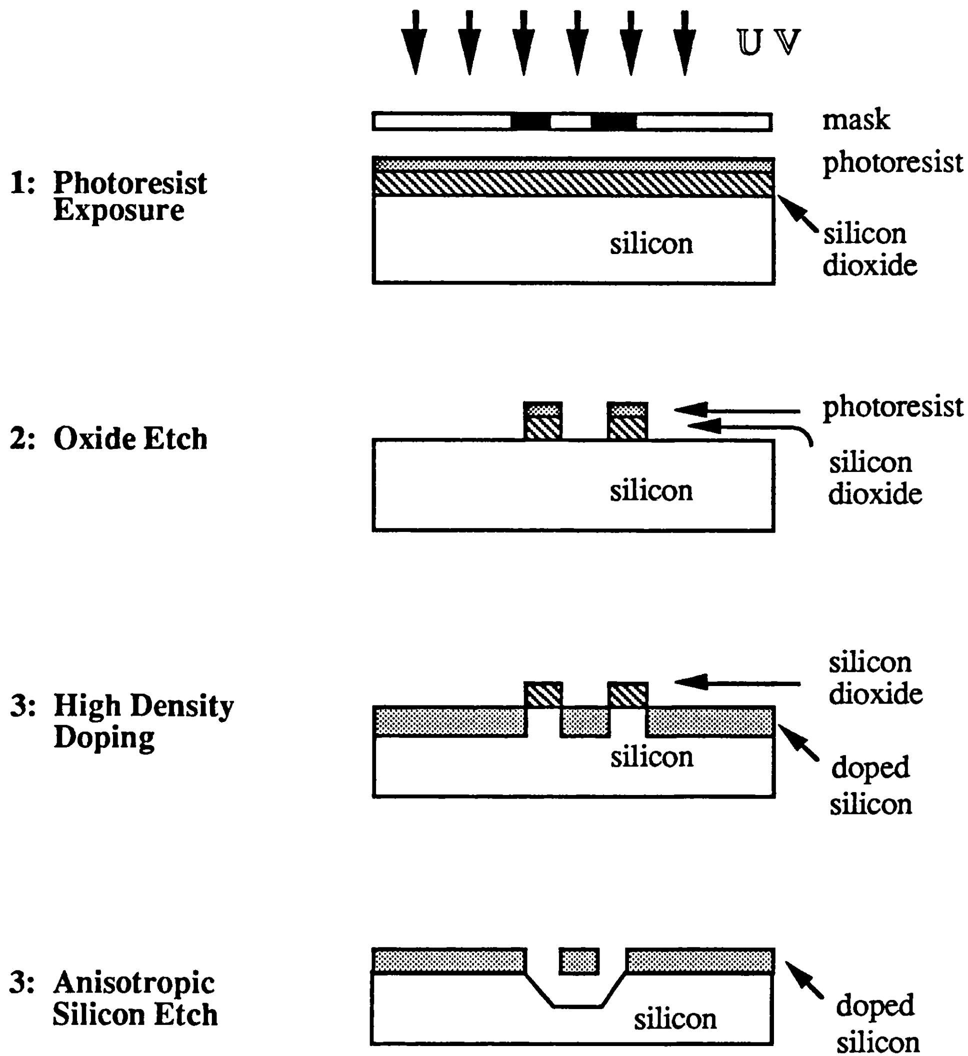

Figure 2.1: Fabrication of silicon structures using photolithography, high-density doping and anisotropic etching.

2:2.3 Anisotropic Etching

Anisotropic etching can be used to form structures of highly doped silicon, or of another material grown on or deposited onto the silicon surface, such as thermally grown silicon dioxide.

In certain etchant solutions the different crystallographic planes of single-crystal silicon etch at significantly different rates. This is thought to result from the differing densities of surface free bonds along these planes. The lower Miller index silicon planes are of particular interest. The position of some of these planes relative to the cubic crystal structure of the silicon is shown in figure 2.2.

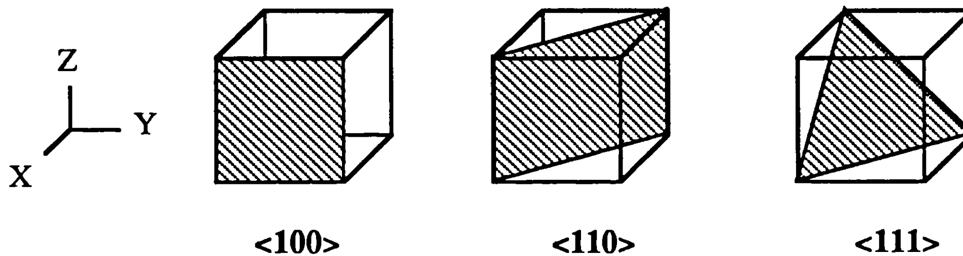

Figure 2.2: Examples of lower index planes.

Anisotropic etchants attack the silicon in the <100> and <110> directions at considerable etch rates, but attack in the <111> direction at a rate typically about 50 times slower [15], and ratios of several hundred to one have been achieved [16]. The available geometries are generally obtained by etching either (100) or (110) oriented crystals through masking windows. High quality silicon wafers of (100) orientation and of (110) orientation [17] are widely available. Silicon dioxide, which is compatible with most device fabrication processes and has a low etch rate in the common anisotropic etch solutions, is commonly used as a mask [18,19]. The high-density doping process described in the previous section uses the doped silicon as a mask.

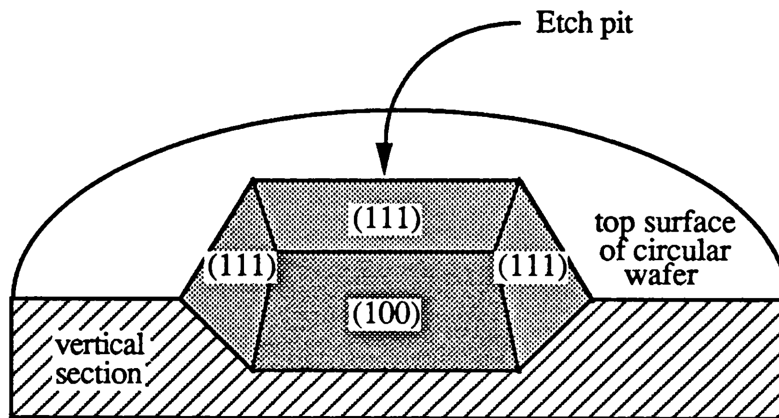

Figure 2.3: Isometric sketch of section through a circular (100) wafer anisotropically etched through rectangular hole.

A (100) silicon wafer has four convergent sets of (111) etch planes 54.74^{o} to the wafer surface plane. These (111) low etch rate planes are at 90° to each other. If the masking window edges are aligned parallel to these planes, forming a rectangle on the (100) surface, the (111) planes will define the angular sidewalls of an anisotropically etched cavity as shown in figure 2.3.

Alternative results are obtained by using (110) wafers, although these were not used in this project. A (110) silicon wafer has two sets of (111) etch planes to the wafer surface plane. These intersect at 90° and 70.52^{o}. It is therefore possible, by aligning the mask window edges precisely parallel to these angles, to form a structure with flat, vertical walls.

The effect of mis-aligning a window on a (100) wafer is to increase the size of the etch hole. This is due to under-etching of the oxide opening, enlarging the hole until its sides are aligned to the nearest (111) planes which enclose the opening. It is thus possible to form undercut oxide strips, producing free-standing oxide bridges, by aligning their sides at 45° to the <110> directions.

The etch stage in the majority of the recently reported work on microfabrication of

resonators is a wet chemical process carried out above room temperature. The most popular orientation-dependent wet etchants have been reviewed elsewhere [20]. Usually alkaline solutions above room temperature are used. The two most widely used are solutions of potassium hydroxide and iso-propanol; or of ethylene diamine and pyrocatechol.

The etch rate in the faster directions is uniform for specific etchant solutions. A flat surface can be propagated retaining flatness to better than one part in 400 [21], enabling very finely thinned pressure diaphragms to be fabricated. However, the final surface may feature regular or irregular pyramid formations, their existance and form depending upon the concentration and purity of the etchants and the temperature and duration of the etching process.

An alternative to the wet chemical etch method is reactive ion etching. This involves mounting the sample to be etched on a water-cooled cathode to which r.f power is capacitatively coupled, causing a discharge between the electrodes [22]. The etching process is a combination of physical and chemical reactions: the chemical mechanism being necessary for anisotropy, since physical bombardment alone is directional, producing negligible sideways etching.

Research on anisotropic or orientation dependent etching of silicon has already produced a wide range of device geometries including silicon V-groove arrays [17], metal microtools [23], optical waveguides [24,25], nozzles [18] and micromechanical devices [26, 27].

2:2.4 Metal Coating Techniques

The preferred methods for the deposition of high quality thin metal films are cathode sputtering and vacuum deposition, both of which have been used for this project [28].

Cathode sputtering involves the production of a glow discharge in an inert gas between an anode and a cathode made from the metal to be deposited. The sample

onto which the film is to be deposited is placed on the anode. The positive ions of the gas bombard the cathode and sputter the metal, some of which condense on the sample.

Vacuum evaporation involves heating the source metal in a chamber at low pressure. Evaporated metal particles travel at their thermal velocities away from the source, and some are deposited onto the sample.

Thin films of evaporated or sputtered metal are known to be under fabrication-induced stress at room temperature [29]. A number of mechanisms are proposed for explaining the experimentally observed stresses, both thermal and intrinsic [30]. During deposition the energy carried by the deposited atoms and, in the case of evaporated metal, radiation from the evaporator filament, causes the temperature of the top layers of the deposit to be raised. Cooling below the recrystallization temperature causes a thermal tensile stress to be developed [31]. Intrinsic stresses have several causes, including the movement of grain-boundaries and imperfections during film growth. These stresses are typically tensile [29]. The absence of a model which can adequately explain all the experimental results [30] makes a quantitive estimate of the total fabrication-induced stress difficult to make. However an order-of-magnitude estimate can be obtained from Murbach & Wilman [31] who measured the mean tensile stress in a layer of evaporated aluminium about 1000-3000Å thick to be about $100kgcm^{-2}$, which is approximately equal to 10^7Nm^{-2}.

2:3 Consideration of Silicon Dioxide Beams

The above discussion has focussed mainly upon silicon structures. Silicon dioxide beams can be formed from oxidised (100) silicon wafers by a combination of photolithographic patterning and anisotropic etching. This process is shown in figure 2.4 below. The oxidation is achieved by holding the silicon wafers in a furnace at high temperature (900-1200^{0}C) while oxygen passes over the wafer surfaces.

It should be noted that in order to produce undercut oxide beams, the sidewalls of the rectangular etch pit are aligned parallel to the (111) planes of the (100) silicon wafer,

so that the (111) planes will define the angular sidewalls of an anisotropically etched cavity as shown in figure 2.3. The beam sides are aligned at 45° to this direction so that undercutting of the beam can take place.

Consideration of the different material properties exhibited by silicon dioxide when compared with silicon lead to the view that the fabrication of structures from silicon dioxide itself might result in sensor devices with practical advantages. Theoretical considerations predict that the stresses which build up during fabrication of a three-dimensional silicon dioxide structure are not tensile but instead cause bending of the resulting beam. As discussed below, this condition is an advantage in a temperature sensor.

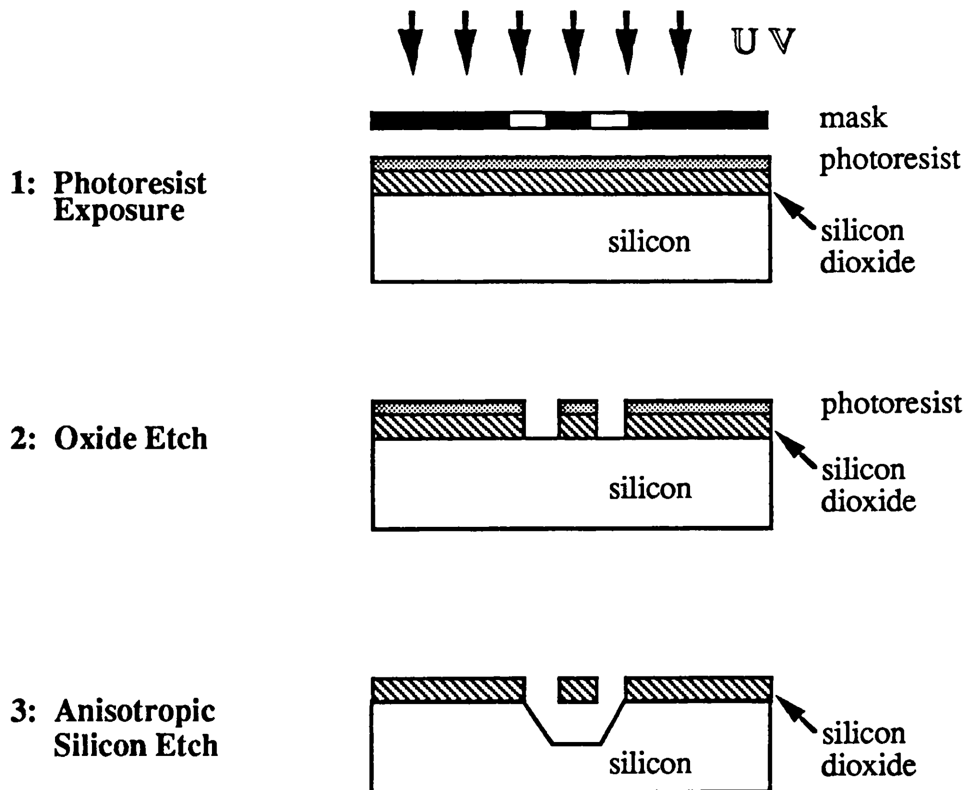

Figure 2.4: Fabrication of silicon dioxide beams.

When silicon is thermally oxidised, the silicon dioxide grown is in a state of compression [32]. Hence when a silicon dioxide beam is defined by etching the silicon beneath an oxide strip it deflects either upward or downward to relieve this compressive stress.

The compression is due to a combination of intrinsic stress and thermal stress. The intrinsic stress is attributed to the volume expansion resulting from the conversion of silicon to its oxide [33]. The thermal stress is induced when the wafer is cooled to room temperature, a process which causes the silicon wafer, on which the oxide has been grown, to contract more than the oxide itself. The total stress in SiO_2 thermally grown on (100) silicon at 900^oC without annealing is typically about $2.5x10^8Nm^{-2}$ [34], although it may be significantly greater (up to around $5x10^9Nm^{-2}$) if the oxide thickness is less than 30nm. When the beam is undercut and allowed to deflect, nearly all the stress is relieved [35].

The resonance frequency of such a beam is predicted in Chapter 5, Section 5:2.1, to be relatively insensitive to pressure changes across the substrate wafer. If this prediction is correct, it would constitute an advantage in the use of sensors developed to measure temperature, for performance in this role would be largely independent of environmental pressure within which the sensor was operating.

Similar considerations lead to the prediction that the performance of the silicon dioxide sensor will not be greatly influenced by epoxy bonding of the device to the optical fibre to which it is to be attached, which itself may introduce stresses into the device structure. If this is confirmed by experiment, a cost advantage would result in the development of commercial manufacturing arrangements.

A practical research programme was therefore needed to determine whether the theoretical hypotheses relating to the practical performance of silicon dioxide devices could be substantiated. A decision was made to devote the first part of this project to establishing first, the feasibility of silicon dioxide devices as resonators, and secondly, whether the advantages predicted could be achieved.

This decision also lead to other advantages. The clean room at University College,

together with the associated equipment, was suitable for the production of silicon dioxide structures. I was therefore able to carry out both the processes of design and of manufacture from standard oxidised wafers as well as the experimentation programme. Perhaps more important was the ability to change device specification within relatively short lead times - thus allowing flexibility in the choice of devices for testing and experiment.

2:4 Devices Fabricated for this Project

This section describes the microresonator devices fabricated for this project. The geometry of a simple silicon beam with constant width before metal coating is shown in figure 2.5. The beam, which has length L, thickness a, and width b, is supported between two opposite corners of an etched pit in a silicon wafer of thickness w.

On completion of the fabrication process, physical dimensions of several beams in each batch were measured using a calibrated scanning electron microscope (S.E.M.). Device surface dimensions (lengths and widths) were measured in this way to an accuracy of ± 5%. Beam substrate thicknesses were estimated using a tilted sample stage on the S.E.M. to an accuracy of ± 10%. Metal thicknesses were measured using a talystep to an accuracy of ± 20%. This was limited by the variation in the metal thicknesses across the area of the sample wafers which were coated. The thicknesses of the thinned wafers were measured using a Logitech table micrometer to an accuracy of ± 10%. Batch standard deviations were estimated using standard statistical techniques based on sample range, assuming a Normal Distribution [36].

2:4.1 Devices Fabricated In-House

A manufacturing programme was undertaken to produce resonator devices, comprising metal-coated silicon dioxide beams across an etched pit in a silicon substrate. All were symmetrical in a horizontal plane about the beam centre.

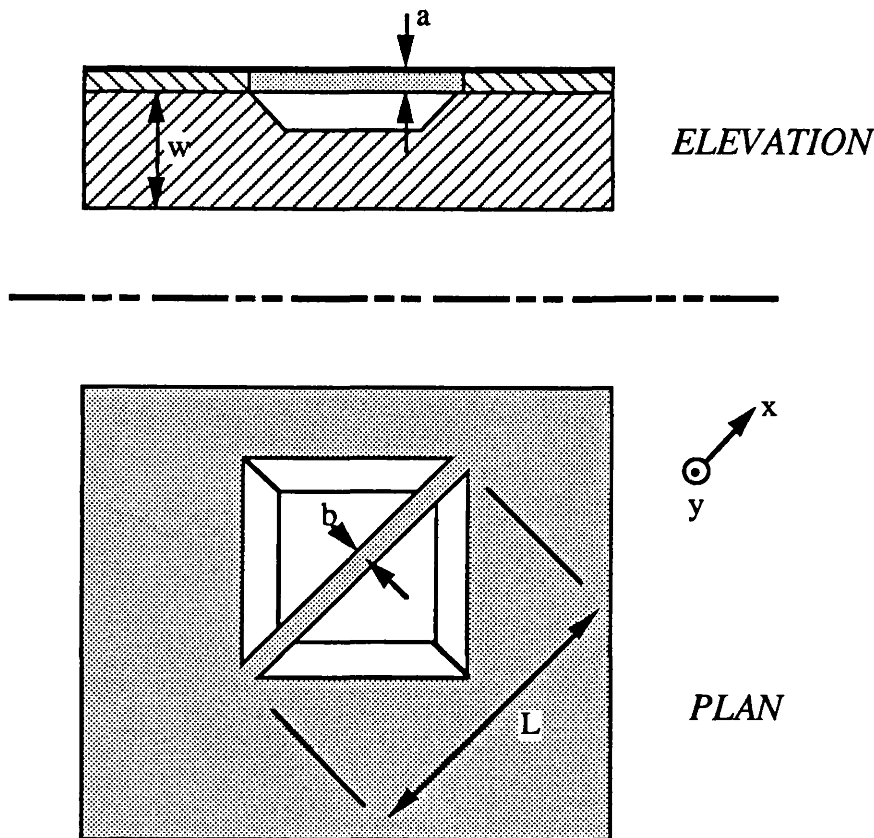

Figure 2.5: Sketch projection of a simple beam resonator. The beam is typically approximately 200μm long, 5μm wide and 0.5μm thick.

Beams of constant width, as shown in figure 2.5, and beams with a wider central area as shown in figure 2.6, referred to as paddle beams, were used in the detailed experimental work described in the following chapters. The paddle beams were designed to have a wider central area to increase the intensity of the light absorbed from the activating beam and reflected from the detecting beam. In addition the beams with the geometries shown in figure 2.6 were also fabricated. These were beams with holes or slots, beams with wings, and beams with modified ends. Experimental work carried out on devices of these kinds is described elsewhere [37].

The stages of fabrication can be summarised as follows, carried out at University College unless otherwise stated:

1. *Mask design,* involving use of the *GAELIC* C.A.D. program for the E-beam mask fabrication facility at the Rutherford Appleton Laboratory.
2. *Photolithographic patterning and oxide etch* using the clean room at University College and associated equipment.
3. *Wet anisotropic silicon etch* using a potassium hydroxide solution.
4. *Metal coating* - evaporation coating with aluminium or sputter coating with gold.
5. *Product selection* - to select those produced within the required specification, necessary because of variations in etching rates, difficulties with handling, etc.
6. *Wafer cutting* to separate the individual resonator elements from the large matrix of mixed elements (approximately 100) normally fabricated on a single silicon wafer.
7. *Wafer thinning* was also carried out on selected devices in order to improve their sensitivity (see Chapter 5).

The entire process could be carried out for a new device design in about 3 months.

A typical photolithographic patterning and oxide etch stage was characterised by the following steps, carried out in the U.C.L. class 100/10,000 clean room:

1. Si (100) 2-inch or 4-inch wafer with 0.5μm or 1.0μm layer of thermally grown SiO_2 obtained externally (Middlesex Polytechnic Electronics Department).
2. Wafer Cut into required pieces using diamond scribe parallel or perpendicular to (110) direction, identified by wafer flat.
3. Wafer pieces agitated in Decon solution to clean.
4. Rinsed in deionised water.
5. Blow-dried with nitrogen.
6. Oven-dried at 120° C for 15 minutes.
7. Spin-coated with photoresist ("AZ4110") at 4000rpm for 30 seconds.
8. Baked at 80°C for 20 minutes.
9. Exposed to U.V. under contact mask for 5.0 seconds, aligning strip sides at approximately 45° to wafer flat.
10. Developed in "351" developing solution for 60 seconds.

11. Baked at 120° C for 30 minutes.
12. Etched with BHF (buffered HF solution, $7H_2O$:1HF by volume) for 4 minutes (0.5μm SiO_2 wafers).
13. Rinsed in acetone.
14. Rinsed in deionised water.
15. Blow dried with nitrogen.

A wet anisotropic silicon etch stage was characterised by the following steps:

1. Solution made up from 25g KOH and 100ml deionised water.
2. Solution heated in flask over stirred oil bath to 82° C $\pm$ 2° C.
3. Sample introduced into solution and left at constant temperature for 30 minutes with slow magnetic stirrer.
4. Sample removed, rinsed in deionised water and blow dried with nitrogen.

The wafer thinning was carried out using a chemical etch method. The back of the silicon wafer pieces to be thinned were exposed to an composition of aqueous HF, nitric acid and acetic acid, typically $1HF:4HNO_3:5CH_3COOH$ by volume.

2:4.2 Devices Fabricated Externally

For purposes of comparison, it was decided to carry out experimental work on metal-coated silicon devices also. Silicon fabrication facilities were already established at Southampton University and they were asked to produce several batches of silicon devices using masks designed at U.C.L. for this project. The devices were subsequently metal-coated at University College and selected devices chemically thinned in a similar way to the silicon dioxide devices fabricated in-house.

Devices fabricated from silicon dioxide deposited at a relatively low temperature (i.e. around 600^{0}C) were also considered. Beams of this nature were also produced at Southampton University using masks designed at U.C.L. for this project. By comparing these with beams fabricated from thermally-grown silicon dioxide, the more suitable could be selected for further experimental work.

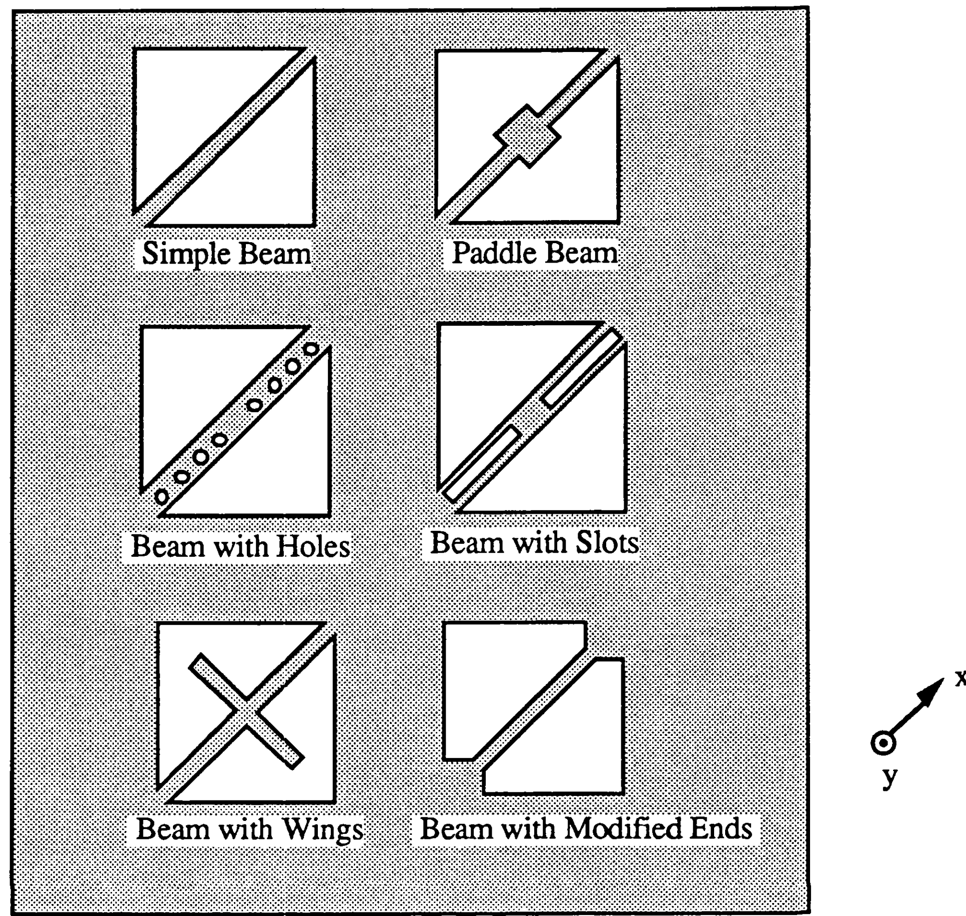

Figure 2.6: Sketch plans of beam geometries fabricated.

2:5 Results of the Fabrication Programme

Metal-coated silicon dioxide devices of all the geometries shown in figure 2.5 and figure 2.6 were successfully fabricated. The beams were typically of thickness 0.5μm, length between 80μm and 250μm and width between 2μm and 8μm. The metal coating thickness was typically between 50nm and 200nm. Scanning electron micrographs of examples of metal-coated silicon dioxide devices fabricated at U.C.L. are shown in figure 2.7 and figure 2.8. The beams shown are fabricated on silicon wafers with a 0.5μm thick layer of thermally-grown silicon dioxide, and coated with 200nm of sputtered gold. Both beams have a wider central area.

Scanning electron micrographs of examples of silicon devices metal-coated at U.C.L. are shown in figure 2.9 and figure 2.10. The beams shown in figure 2.9 and figure 2.10 are fabricated on silicon wafers with a 0.5μm thick layer of boron doped silicon, and coated with 200nm of sputtered gold. The beam shown in figure 2.10 has been designed with several holes.

The batch standard deviation of beam lengths was estimated using a batch of six samples to be 8%, and of beam thicknesses to be 26%. Details of typical bathes are described in Chapter 4, Section 4:3.2.

In addition, using the chemical thinning method, it was possible to thin the silicon wafers on which beams had been fabricated. The nominal thickness of the standard silicon wafers used was 375μm and this could be reduced to approximately 180μm. The method produced wafers of non-uniform thickness. Alternative methods, particularly the use of an etch-stop layer to define a thinned diaphragm structure [38], are available for this part of the fabrication process.

A number of significant physical features of these devices were examined. These include webbing at the beam ends, non-rectangular beam cross-sections, and beam bending. These features are described in the following discussion.

All the devices examined featured a ledge of material overhanging the edges of the etched pit in the silicon substrate. This can be seen in figure 2.7, figure 2.8, figure 2.9 and figure 2.10 as thin strips of lighter material along the edges of the etched pits. This lighter material is, in the case of figure 2.7 and figure 2.8, undercut oxide, and in the case of figure 2.9 and figure 2.10, undercut doped silicon.

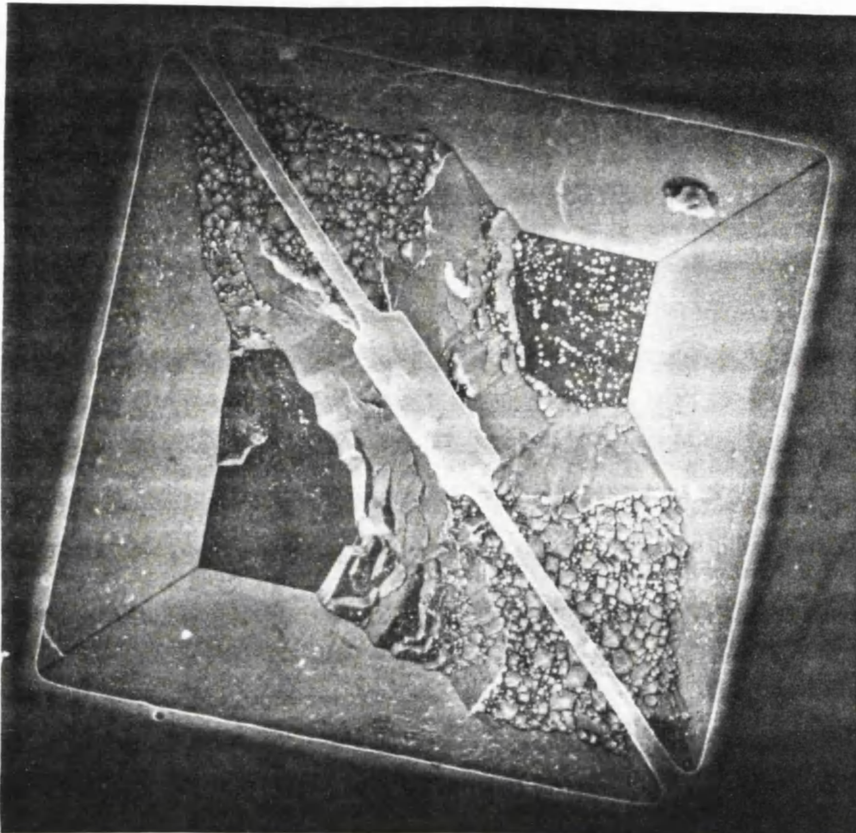

Figure 2.7: Scanning electron micrograph of gold coated SiO_2 paddle beam (beam length 230μm).

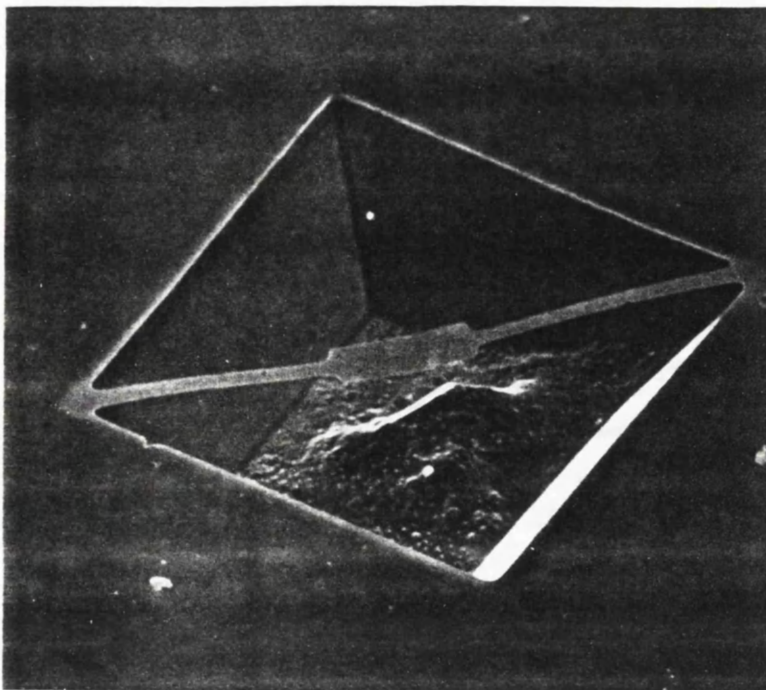

Figure 2.8: Scanning electron micrograph of gold coated SiO_2 paddle beam (beam length 185μm).

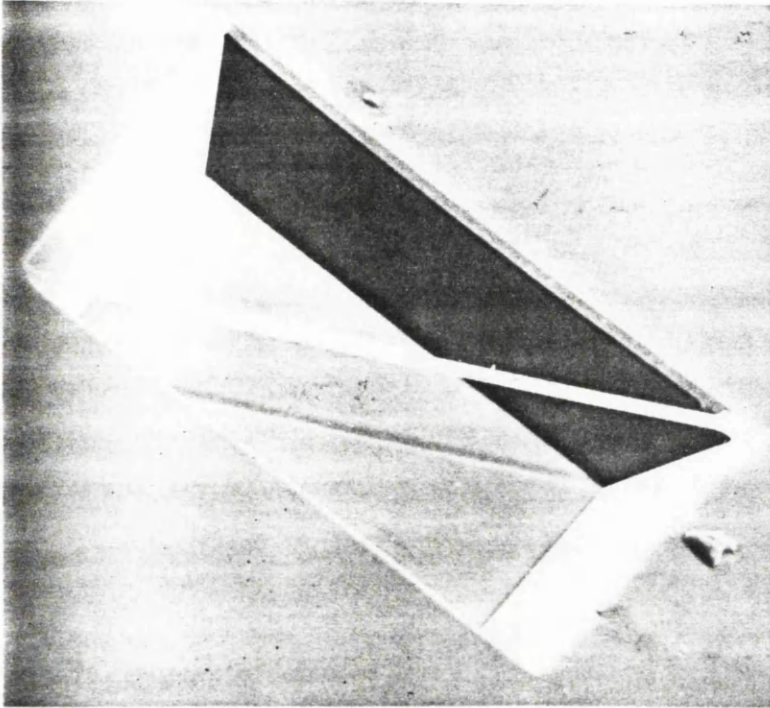

Figure 2.9: Scanning electron micrograph of gold coated Si simple beam (beam length 185μm).

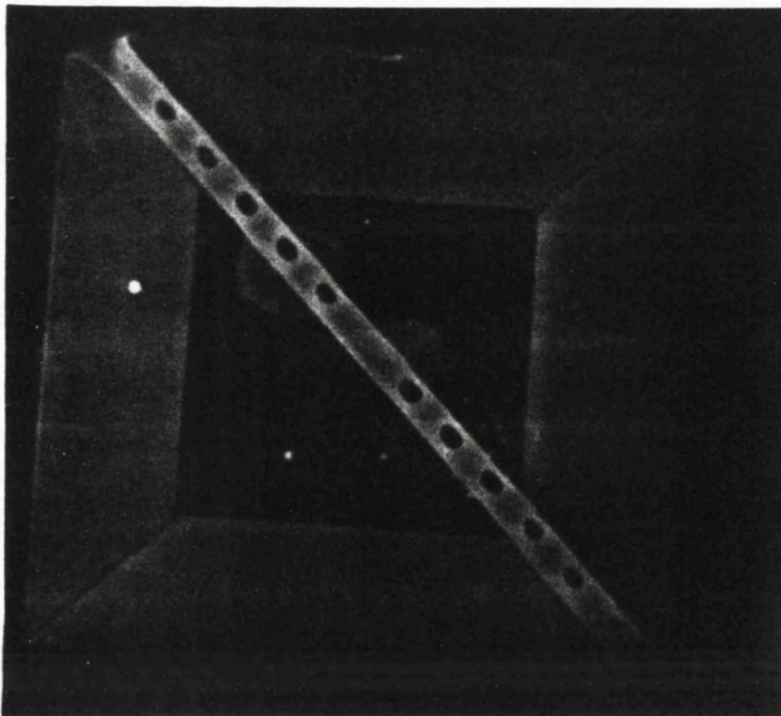

Figure 2.10: Scanning electron micrograph of gold coated Si beam with holes (length 180μm).

The formation of a ledge is partly a result of the finite etch rate of the silicon (111) planes, so that during the silicon etch stage of the fabrication process the pit sides are etched sideways, and partly of the imperfect alignment of the etch mask relative to the silicon wafer. The effect of misalignment is illustrated in figure 2.11 which shows a silicon dioxide ledge of varying width overhanging a silicon pit. In this case etching of planes other than the (111) sidewalls has been possible at the pit sides. Etching of the pit sidewalls also takes place at the pit corners, so that the beam ends are attached to the supporting silicon wafer by means of webbing.

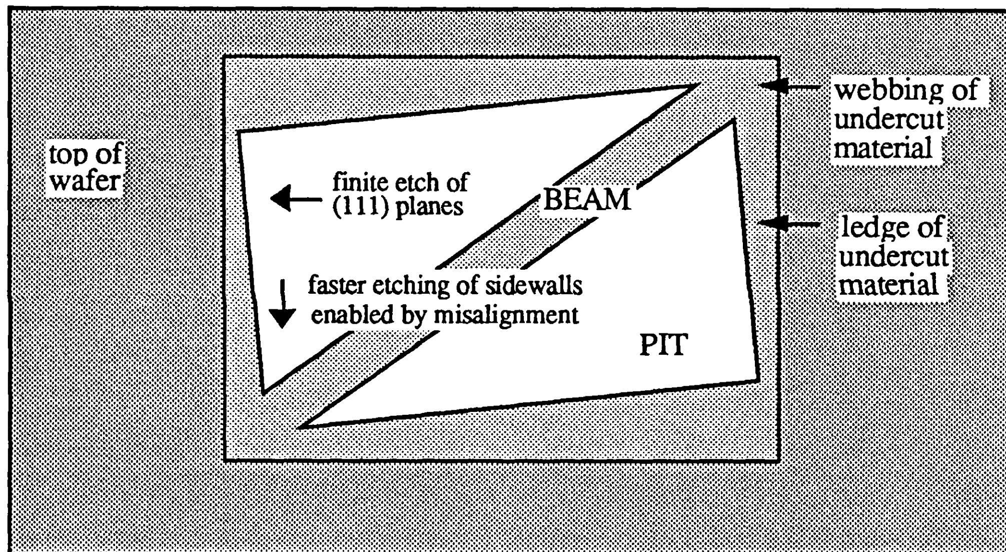

Figure 2.11:Sketch plan of beam microfabricated on a silicon wafer, showing the effect of etching of the sidewalls.

Figure 2.12 shows a pit etched in a silicon wafer whose edges have been misaligned by several degrees from the (111) planes. This has enabled a silicon dioxide ledge of varying width to be formed. In this case the silicon dioxide beam has been destroyed.

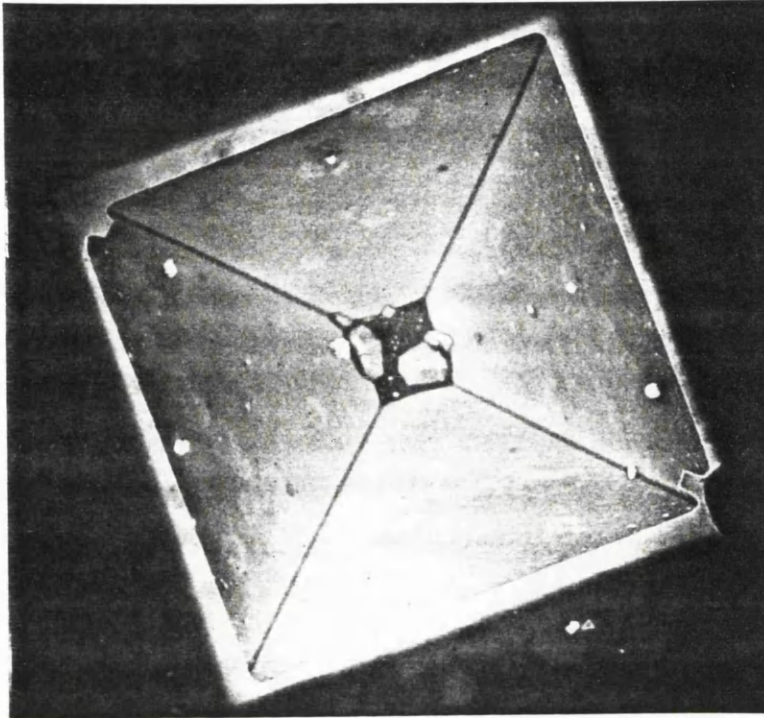

Figure 2.12: Scanning electron micrograph of misaligned etched pit in Si wafer (pit side length 130μm).

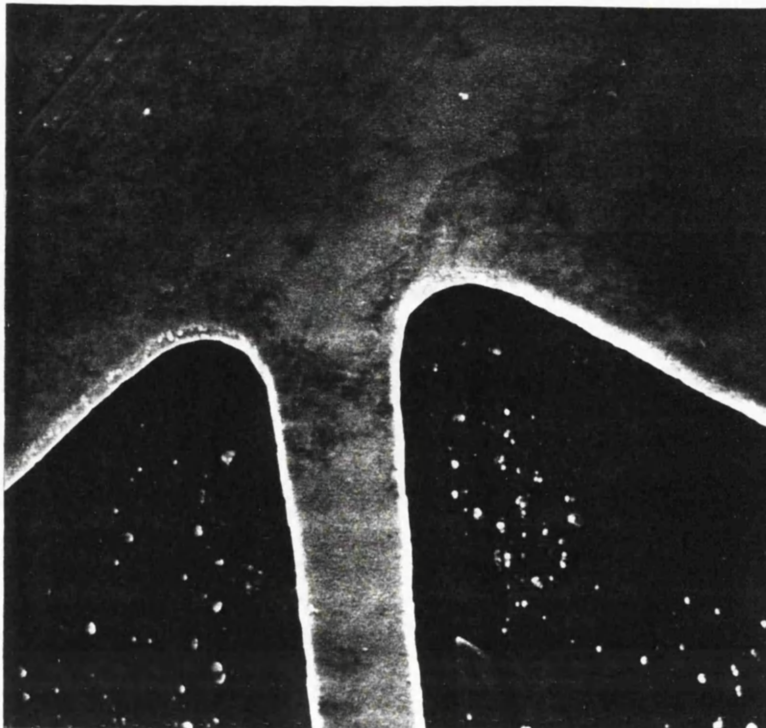

Figure 2.13: Scanning electron micrograph of gold coated SiO_2 paddle beam webbed corner (beam width 5μm).

A detail of a webbed beam end is shown in figure 2.13. This figure shows detail of a silicon dioxide beam fabricated on a silicon wafer with a 0.5μm thick layer of thermally-grown silicon dioxide, and coated with 200nm of sputtered gold. The undercut oxide webbing can be seen as an area of lighter material around the beam end. The width of the oxide ledge for a typical beam of this kind is of the order of 5μm. The extent of the webbing at each end of such a beam in the direction of its length is of the order of 10μm.

The effect of these webbed beam ends is discussed in the following chapter.

The silicon dioxide devices were observed to have non-uniform widths, and to have tapering cross-sections as shown in figure 2.14.

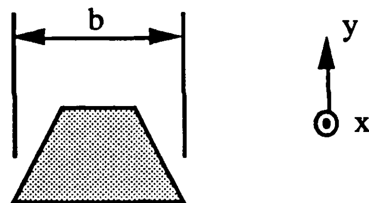

Figure 2.14:Sketch of tapering vertical cross-section of oxide beam.

This is thought to be a result of sideways etching during the oxide etch stage of the fabrication process. The total extent of the taper is small, so that the width of the top surface of the beam was estimated from scanning electron micrographs to be more than 90% of the width of the bottom surface even for a narrow beam of the order of 2μm mean width. A similar but more pronounced effect was observed for the silicon devices, so that the width of the top surface of the beam was estimated to be a minimum of 70% of the width of the bottom surface for a beam of the order of 2μm mean width.

The silicon dioxide beams examined were all noticeably bent, as predicted in Section 2:3 of this chapter. The extent of the bend was estimated from scanning electron micrographs. A typical paddle beam is shown photographed on a tilted S.E.M. stage in figure 2.15. Both silicon dioxide beams have length 185μm, stem width 5.0μm and thickness 0.5μm, and are coated with sputtered gold of thickness 200nm. For this beam the maximum deflection, which was at the beam centre (Δ' in figure 2.15), was measured using a tilted S.E.M. stage to be 6μm ± 1μm.

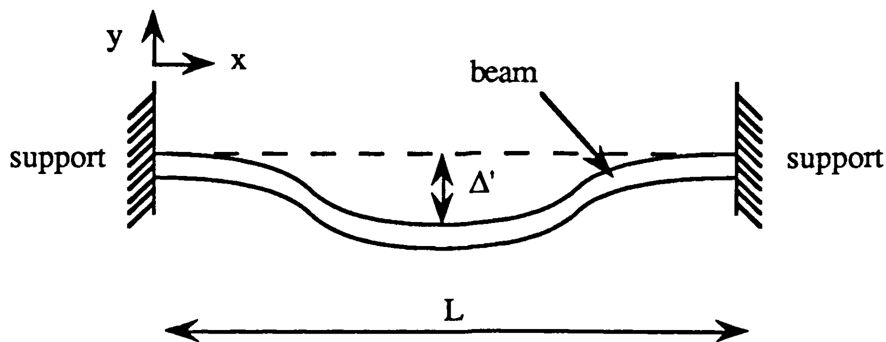

Figure 2.15: Sketch of deflected beam.

Devices of similar dimensions fabricated from silicon dioxide deposited at a relatively low temperature (i.e. around 600^0C) were also examined. The central deflections of these beams were significantly greater than those of the beams fabricated from thermally grown oxide, and further experimental work concentrated on the thermally grown oxide devices.

Finally it is noted that the thicknesses of the oxide beams are in general found to be less than the original thickness of the thermally grown oxide layer on the silicon wafers on which the beams are fabricated. This difference is due to the finite etch rate of the oxide in the silicon etch, which also results in a reduction in the beam widths.

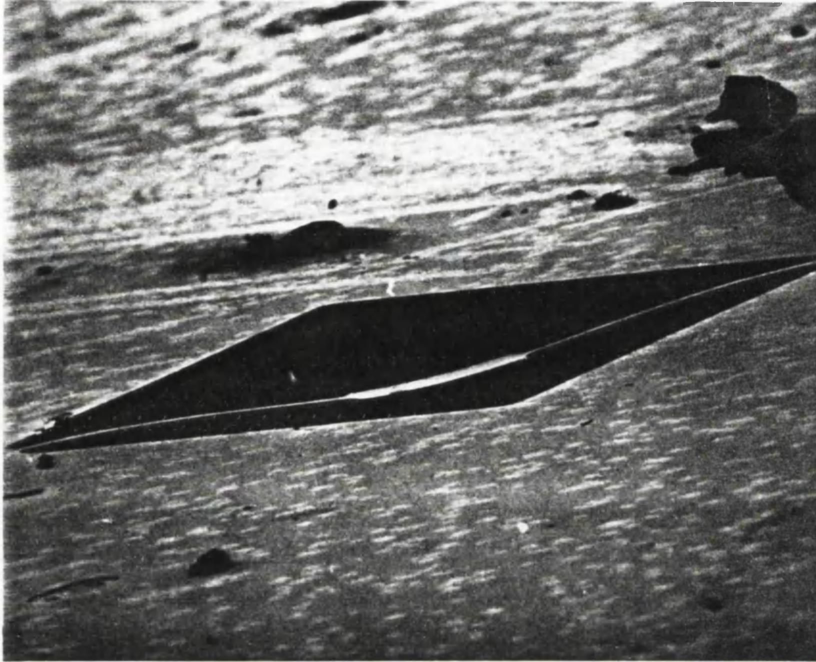

Figure 2.16: Scanning electron micrograph of gold coated SiO_2 paddle beam (beam length 185μm).

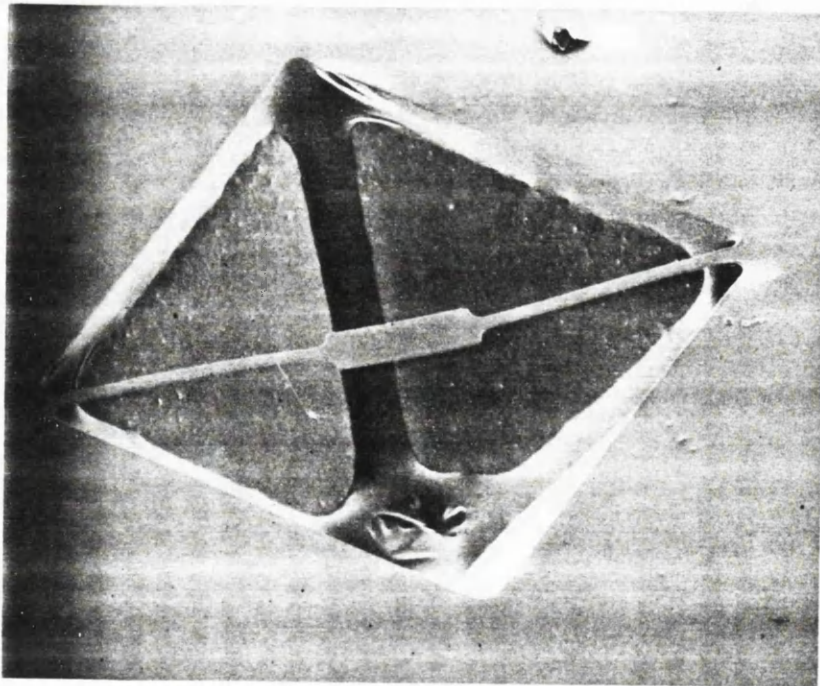

Figure 2.17: Scanning electron micrograph of gold coated SiO_2 paddle beam (beam length 185μm).

The oxide etch rate, which can be estimated by measurements of the oxide beam widths before and after the silicon etch stage, is observed to be dependent on the etch conditions. For the conditions specified in Appendix A the oxide etch rate is approximately 6nm / min.

It is therefore possible to fabricate thin silicon dioxide beams by prolonging the silicon etch stage of the fabrication process. Such a beam is shown in figure 2.17. In this case the silicon etch time has been increased from the standard 30 minutes to 50 minutes. It can be seen that the etch pit is significantly deeper than that shown in figure 2.7 because of the greater etch time. The beam shown in figure 2.17 has an oxide thickness of 150nm and a gold coating thickness of 350nm.

2:6 Conclusions

We have established a straightforward procedure for the design and fabrication of metal coated silicon dioxide microresonator devices using oxidised silicon wafers in a class 100/10,1000 clean-room environment. Metal-coated silicon dioxide structures of a number of designs have been fabricated. In addition, silicon structures, designed and specified within this project, have been fabricated elsewhere.

A number of important features were observed and measured. These include an overhang of the beam substrate material around the etched pit in the silicon wafer. This was caused by slow sideways etching of the pit sidewalls, and is expected to be significant only for microstructures whose dimensions are comparable with those of the ledge. At the beam ends this overhang took a complex shape called webbing.

In addition the silicon dioxide beams fabricated in-house were observed to be deflected from the surface plane of the silicon wafer. This is consistent with the effect of a compressive stress, induced in the oxide during the thermal growth process, and relieved when the silicon beneath the beams is removed. In line with prediction, no such deflection was observed for the silicon beams.

References for Chapter 2

1. C.J.Schmidt *et al.*; "*Preparation Of Thin Windows In Silicon Masks for X-ray Lithography*"; J.Appl.Phys.46, p4080, 1975
2. C.L.Huang & T.Van Duzer; "*Schottky Diodes And Other Devices On Thin Silicon Membranes*"; IEEE Trans.Electron Dev.ED-23, pp579-583, 1976
3. S.K.Clark & K.D.Wise; "*Pressure Sensitivity In Anisotropically Etched Thin-Diaphragm Pressure Sensors*"; IEEE Trans.Electron Dev.ED-26, pp1887-1896, 1979
4. T.J.Rodgers & J.D.Meindl; "*Epitaxial V-groove Bipolar Integrated Circuit Process*"; IEEE Trans.Electron Dev.ED-20, pp 226-232, 1973
5. T.J.Rodgers & J.D.Meindl; "*VMOS: High Speed TTL Compatible MOS Logic*"; IEE J.Solid-State Circ.SC-9, pp 239-249, 1974
6. M.J.Declercq; "*A New C-MOS Technology Using Anisotropic Etching Of Silicon*"; IEE J.Solid-State Circ.SC-10, pp191-197, 1975
7. D.L.Spears & H.I.Smith; "*X-ray Lithography: A New High Resolution Replication Process*"; Solid State Technol., vol.15, pp 21-26, 1972
8. H.Guckel *et al.*; "*Electromechanical Devices Utilising Thin Si Diaphragms*"; Appl.Phys.Lett., vol.31, pp618-619, 1977
9. J.C.Greenwood; "*Ethylene diamine-catechol-water mixture shows preferential etching of p-n junction*"; J.Electrochem.Soc.116, pp 1325-1326, 1969
10. E.D.Palik *et al.*; "*Ellipsometric Studies in Heavily Doped Silicon*"; J.Electrochem.Soc.132, pp 135-141, 1985
11. A.Bogh; "Ethelyne Diamine-Pyrocatechol-Water Mixture Shows Etching Anomaly in Boron Doped Silicon"; J.Electrochem.Soc.118, pp401-402, 1971
12. J.C.Greenwood; "*Etched Silicon Vibrating Sensor*"; J.Phys.E.: Sci.Instrum., Vol.17, pp650-652, 1984
13. O.J.Glembrocki & R.E.Stahlbush; "*Bias-Dependent Etching of Silicon In Aqueous KOH*"; J.Electrochem.Soc.132, pp 145-151, 1985
14. K.E. Peterson; "*Silicon As A Mechanical Material*"; Proc. IEEE, Vol.70, pp420-457, 1982

15. K.D.Wise; "Silicon Micromachining and its Application to High-Performance Integrated Sensors"; *'Micromachining and Micropackaging of Transducers'*, ed. C.D.Fung, P.W.Cheung, W.H.Ko, D.G.Fleming; Elsevier, Amsterdam
16. G. Kaminsky; *"Micromachining Of Silicon Mechanical Structures"*; J.Vac.Sci.Technol. B 3(4), pp 1015-1024, 1985
17. D.L.Kendall & G.R. de Guel; *"Orientations of the Third Kind: The Coming of Age of (110) Silicon"*; "Micromachining and Micropackaging of Transducers", ed. C.D.Fung, P.W.Cheung, W.H.Ko & D.G.Fleming, Elsevier, Amsterdam.
18. E.Bassous; *"Fabrication Of Novel Three-Dimensional Microstructures By The Anisotropic Etching of (100) and (110) Silicon"*; IEEE Trans.Electron Dev.ED-25, pp1178-1185, 1978
19. E.D.Palik *et al.*; *"Ellipsometric Study Of Orientation-Dependent Etching Of Silicon In Aqueous KOH"*, J.Electronchem.Soc., 132, pp871-884, 1985
20. K.E. Bean; *"Anisotropic Etching Of Silicon"*; IEEE Trans.Electron Dev.ED-25, pp1185-1193, 1978
21. J.Greenwood;*"Silicon Based Sensors: Technology Overview"* IOP Short Meetings Series No.3 *'Silicon Based Sensors'*; pp1-13, 1986
22. S.Somech; *"Introduction to Ion and Plasma Etching"*; J.Vac.Sci.Technol. 13, pp1003-1007, 1976
23. D.A.Kiewit; *"Microtool Fabrication By Etch Pit Replication"*; Rev.Sci.Instrum., Vol.44, pp1741-1742, 1973
24. W.T.Tsang, C.C.Tseng & S.Wang; *"Optical Waveguides Fabricated By Preferential Etching"*; Appl.Opt., vol.14, pp1200-1206, 1975
25. J.S.Harper & P.F.Heidrich; *"High Density Multichannel Optical Waveguides With Integrated Couplers"*; Wave Electronics, vol.2, pp369-377, 1976
26. S.C.Terry; *"A Gas Chromatography System Fabricated On A Silicon Wafer Using Integrated Circuit Technology"*; Ph.D.dissertation, Stanford University Elec.Eng.Dept., 1975
27. R.E.Peterson; *"Micromechanical Light Modulator Array Fabricated On Silicon"*; Appl.Phys.Lett., vol.31, pp 521-523, 1987
28. I.Brodie & J.J.Muray; "The Physics of Microfabrication"; Plenum Press, New York, 1982
29. L.Eckertova "Physics of Thin Films", Plenum Press, New York, 1977

30. L.I.Maissel & R.Glang; "Handbook of Thin Film Technology", McGraw Hill, New York, 1970
31. H.P.Murbach & H.Wilman; *"The Origin of Stress in Metal Layers Condensed from the Vapour in High Vacuum"*; Proc.Phys.Soc.London, vol.66B, pp905-910, 1953
32. R.J.Jaccodine & W.A.Schlegel; *"Measurement of Strain at Si-SiO_2 Interface"*; J.Appl.Phys., vol.27, pp2429-2434, 1966
33. S.Alexandrova *et al.*; *"Stress in Silicon Dioxide Films"*; Phil. Magazine Lett., vol. 58, pp33-36, 1988
34. T.P.Ma; *"Stresses in SiO_2-on-Si Structures"*; EMIS Datareview RN15733, pp650-661, 1987
35. S.C.H.Lin & I.Pugacz-Muraszkiewiz; *"Local stress measurement in thin thermal SiO2 films on Si substrates"*; J Appl Phys, vol.43, pp119-125, 1972
36. D.V.Lindley & J.C.P.Miller; "Cambridge Elementary Statistical Tables", CUP, Cambridge, 1953
37. R.M.A.Fatah, N.A.D.Stokes and S.Venkatesh; *"Activation of Silicon Micromechanical Resonators in Fibre Optic Systems"*; European Fibre Optic Communication and Local Area Networks Exposition, Amsterdam, June 1989
38. K.D.Wise; *"Silicon Micromachining and its Application to High-Performance Integrated Sensors"*; "Micromachining and Micropackaging of Transducers", ed. C.D.Fung, P.W.Cheung, W.H.Ko & D.G.Fleming, Elsevier, Amsterdam, 1985.

CHAPTER 3:
ANALYSIS OF MICRORESONATOR VIBRATIONS

3:1 Introduction

3:2 Theory of Beam Resonance

3:2.1 Resonance Frequencies of Transverse Flexural Modes

3:2.1.1 Simple Beams

3:2.1.2 Beams with a wider central area or wings

3:2.1.3 Effect of Tension

3:2.1.4 Adjusting for Composite Strips

3:2.2 Resonance Frequencies of Torsional Modes

3:2.3 Quality Factor

3:3 Optical Excitation of Microresonators

3:3.1 Theory of Opto-Thermal Conversion of Energy

3:3.1.1 Consideration of Optical Loading

3:3.1.2 Steady Component of the Incident Light

3:3.1.3 Oscillatory Component of the Incident Light

3:3.1.4 Consideration of Quality Factors

3:4 Fabrication-Induced Effects in Microfabricated Devices

3:4.1 Fabrication-Induced Stress

3:4.1.1 Deflection of a Bent Beam

3:4.1.2 Stress in a Deflected Beam

3:4.2 Etch-Defined End Conditions

3:5 Conclusions

References for Chapter 3

CHAPTER 3

ANALYSIS OF MICRORESONATOR VIBRATIONS

3:1 Introduction

The resonance frequencies of devices such as those described in the previous chapter depend on the dimensions of the devices and on the mode of vibration excited. The mechanical behaviour of these beams can be modelled using the hypothesis that standard beam theory developed for studying macrostructures can be extrapolated to describe these microstructures also. It will then be possible to examine by experiment whether the behaviour of microresonators diverges from this model.

It is noted that the physical configuration of the beams fabricated as described in Chapter 2 are significantly different from the simple beams which are modelled and provide the basis for standard beam theory. Differences include a non-rectangular and varying beam cross-section, webbing at the beam ends, tension and compression in the beam materials, and beam bending. The vibrational model can be extended to include the effects of these features.

In order to examine the effect of an optical drive on a microresonator beam, the energy conversion process involved in the excitation of vibrations is modelled analytically for beams such as those used in this project. In this way the amplitude of vibrations can be predicted.

The theoretical results derived in this chapter are used as a basis for much of the experimental work which follows.

3:2 Standard Theory of Beam Resonance

The mechanical behaviour of microresonator beams is initially modelled using standard theory developed for studying macrostructures. This theory gives formulae for the frequencies of vibrations of beams in several configurations relevant to this project. This section summarises these results.

3:2.1 Resonance Frequencies of Transverse Modes

A simple beam resonator fabricated on a silicon wafer is shown diagrammatically in figure 2.5, reproduced as figure 3.1 below.

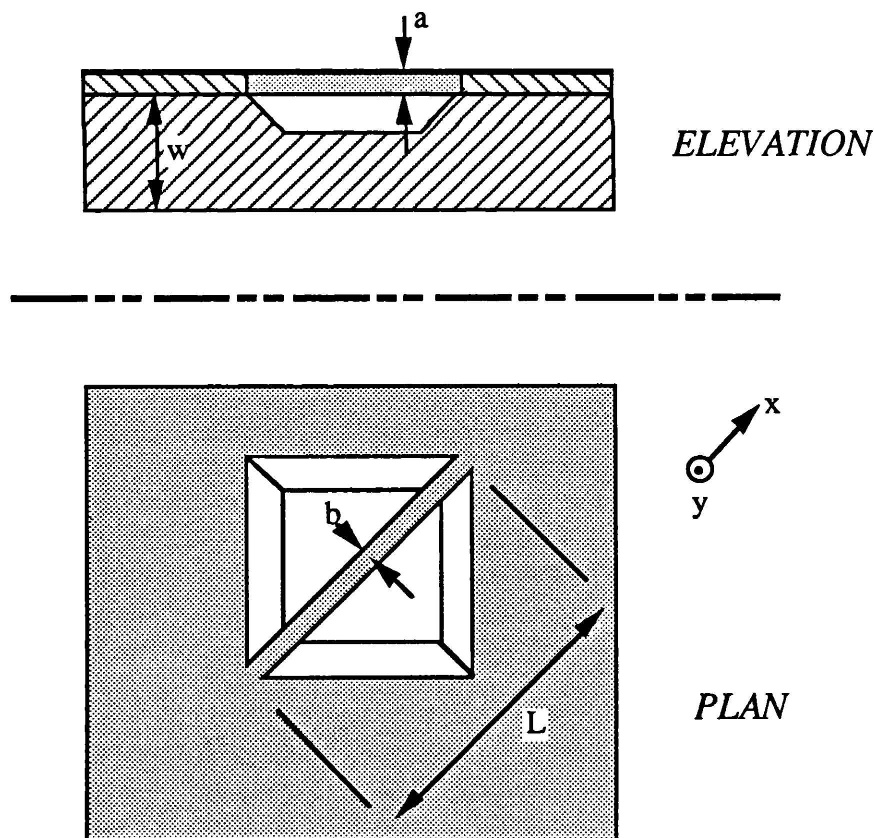

Figure 3.1: Projection of a simple prismatic beam resonator.

The principal vibrations considered are those of transverse modes in the x-y plane. The co-ordinate system used is shown in figure 3.1, with $x = y = 0$ at the beam end. a is the beam thickness, b is the beam width, L is the beam length, and w is the thickness of the silicon wafer on which the beam has been fabricated.

3:2.1.1 Simple Beams

Formulae for frequencies of resonance vibrations of a simple prismatic beam (figure 3.1) can be derived by making the following simplifying assumptions [1]:

Plane sections remain plane

The beam is uniform, homogeneous and linearly elastic

Rotary inertia and shear deformation may be ignored

Deflections are small

The natural frequencies of transverse vibrations may be derived by considering the forces on a small beam element [1], as

$$f_i = \frac{\phi_i^2 \pi}{2L^2} \sqrt{\frac{EI}{\rho A}} \qquad \{3.1\}$$

where E is the Young's modulus of the beam; I is the second moment of area of the beam; A is the beam's cross-sectional area; ρ is the density; i signifies the ith mode; and ϕ_i is a dimensionless parameter which depends on the end conditions of the vibrating beam. For a beam of rectangular cross-section:

$$I = \frac{a^3 b}{12} \qquad \text{and} \qquad A = a\,b$$

whence

$$f_i = \left[\frac{\phi_i^2 \pi}{4\sqrt{3}}\right]\left[\frac{a}{L^2}\right]\sqrt{\frac{E}{\rho}} \qquad \{3.2\}$$

The relevant standard end conditions are as follows:

Clamped ($y = \delta y/\delta x = 0$) at both ends, for which $\phi_i = (i + 1/2)$

Pinned ($y = \delta^2 y/\delta x^2 = 0$) at both ends, for which $\phi_i = i$.

3:2.1.2 Beams with a wider central area or wings

Several types of beam have been excited. The most common variation from the simple beam is the addition of a wider central area, known as a paddle beam. The resonance frequency of transverse vibrations for beams with a wider central area or wings, as shown in figure 3.2, are expected to be lower than those predicted by eqn.{3.2} because of the additional mass.

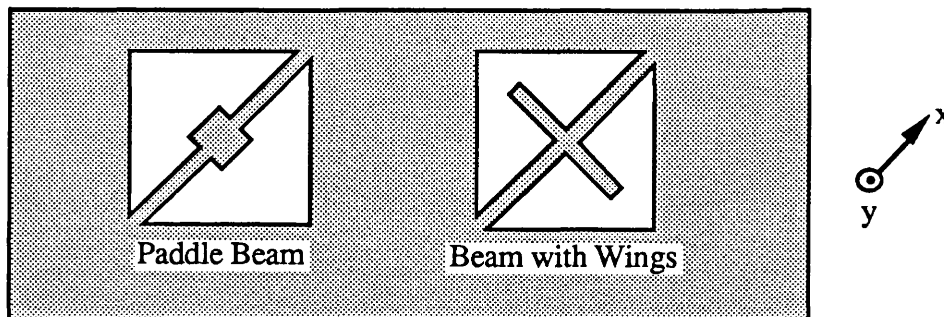

Figure 3.2: Sketch plans of paddle beam and beam with wings.

The correction factor may be estimated by approximating this additional mass to be concentrated in the centre of the beam. In this case the fundamental natural frequency is given by [2]:

$$f_i^* = f_i \left[\frac{2.7\,M}{M_b} + 1 \right]^{-\frac{1}{2}} \qquad \{3.3\}$$

where M_b and M are respectively the mass of the *additional* central area and the mass of the beam exclusive of the additional central area, and f_i is the fundamental natural resonance frequency predicted from eqn.{3.2}, using the clamped end condition.

3:2.1.3 Effect of Tension

In order to calculate the variation of resonance frequency of a beam with pressure or temperature it is necessary to know the effect of introduced tension. Tension or compression introduced into the resonator beams will change the resonance frequencies because of the additional bending moment which results [1]. The shift in resonance frequency, Δf, for a beam of rectangular cross-section subjected to an axial force F, can be calculated from [3]:

$$\frac{\Delta f}{f_0} = \pm c \, \frac{F L^2}{E b a^3} \qquad \{3.4\}$$

where f_0 is the resonance frequency of the relaxed beam; and c is a constant with value 0.147. The positive and the negative signs are, respectively, applied to the applications of tensile and compressive forces.

The shift in resonance frequency may be expressed in terms of stress $\sigma = F / ab$ by

$$\frac{\Delta f}{f_0} = \pm c \, \frac{\sigma L^2}{E a^2} \qquad \{3.5\}$$

3:2.1.4 Composite Strips

The frequency equation for transverse flexural vibrations can be adjusted to apply to composite strips by calculating an equivalent EI product (known as the flexural rigidity) for the applied moments in equation {3.1}. For a simple beam of rectangular cross-section of substrate thickness a_p coated with metal of thickness a_m the equivalent EI product is given by [1]:

$$E I_{equiv.} = \frac{w a_p^3 \, a_m E_p E_m}{12 \left(a_m E_m + a_p E_p \right)} \times$$

$$\left[4 + 6 \frac{a_m}{a_p} + 4 \left(\frac{a_m}{a_p} \right)^2 + \frac{E_m}{E_p} \left(\frac{a_m}{a_p} \right)^3 + \frac{E_p}{E_m} \frac{a_p}{a_m} \right] \qquad \{3.6\}$$

where E_m and E_p are the Young's moduli of the metal and of the substrate material.

3:2.2 Resonance Frequencies of Torsional Modes

It may be possible to excite torsional vibrations as well as transverse vibrations in microresonator beams. The natural frequencies of torsional vibrations of a beam under the assumptions previously outlined, but accounting for rotary inertia, are [2]:

$$f_i = \frac{i}{2L} \left(\frac{C.G}{\rho.I_p} \right) \qquad \{3.7\}$$

where I_p is the polar moment of area; G is the torsional modulus; and

$$C = \frac{e.a^3.b^3}{a^2 + b^2} \qquad \{3.8\}$$

where the shape factor e is determined by the ratio b:a as follows:

b/a :	1	2	4	8	∞
e :	0.281	0.286	0.299	0.312	1/3

3:2.3 Quality Factor

The quality factor (Q) of resonance is important because it is a measure of the energy losses. This determines the width of the resonance peak and hence the accuracy to which it may be measured. The quality factor may be defined as the ratio of the amplitude of motion at resonance to the amplitude of motion as the drive frequency tends to zero [1]:

$$Q = \frac{y_{0\ (res.)}}{y_{0\ (f'\ 0)}} \qquad \{3.9\}$$

If the beam of mass M experiences a damping force with a damping constant R due to internal friction and viscous losses, and a restoring force per unit displacement k, then the angular frequency at resonance $\omega = 2\pi f$ may be derived as [1]

$$\omega_{res} = \sqrt{\frac{k}{M}} \qquad \{3.10\}$$

and the quality factor as

$$Q = \frac{\sqrt{Mk}}{R} \qquad \{3.11\}$$

3:3 Optical Excitation of Microresonators

In the last section we looked at the general way in which beams are expected to behave mechanically. In this section we consider the method of excitation, and analyse the way in which an optical beam, emerging from an optical fibre, may be expected to activate and sustain vibrations of beams such as those described in Chapter 2, Section 2:4.

It was intended that mechanical vibrations of the microresonators should be excited and detected by light from laser beams emerging from a single optical fibre end positioned a few microns from the device surface. A number of activation methods are possible, all of which involve the absorption of some of the incident light. At the same time, the optical detection of vibrations involves the reflection of light from the device surface back into the optical fibre end. For this reason the microresonator beams are all metal coated.

The method considered initially, which was used as the basis of all the experimental work described in Chapter 4 and Chapter 5, is that of using an intensity modulated laser for the activation of vibrations and a second, unmodulated, laser at a different wavelength for the detection of vibrations. The fibre-optic system is described in detail in Chapter 4, Section 4:2.1.

3:3.1 Theory of Opto-Thermal Conversion of Energy

When an intensity modulated optical source is directed onto the metal-coated surface of a resonator beam, some of the energy is absorbed, causing localised periodic heating. This results in periodic expansion and contraction of the structure, leading in turn to flexural vibrations. Optical energy is thus converted to mechanical energy via an intermediate thermal stage. This process is known as the *photothermal effect* and has been used in a number of applications including spectroscopy [4] and microscopy [5]. The optically-induced thermal wave may also generate an acoustic wave which may itself be measured; this closely allied process has been used in similar applications [6,7] and is known as the *photoacoustic effect*. Theory published on the photoacoustic effect is also relevant to the photothermal effect [8,9].

In order to examine qualitatively and quantitively the effect of an optical drive on a microresonator beam, this process is modelled analytically for beams such as those used in this project.

3:3.1.1 Consideration of Optical Loading

The incident light intensity on the resonator strip from the modulated activating laser is of the form

$$\Psi_{act.} = \Psi_0 \left(1 + m \cos 2\pi f t \right) \qquad \{3.12\}$$

where m is the modulation depth and f is the modulation frequency. It may be noted that non-linearities in or over-drive of the Bragg cell can produce modulation harmonics at integer multiples of the drive frequency.

The incident light intensity can be considered as a superposition of a steady component Ψ_0 and a time varying component $m\Psi_0 \cos 2\pi ft$. The intensity is assumed to be uniform over a small area b^2 at the centre of the beam, where b is the beam width, superimposed on the steady intensity from the detecting laser $\Psi_{det.}$. This is illustrated in figure 3.3.

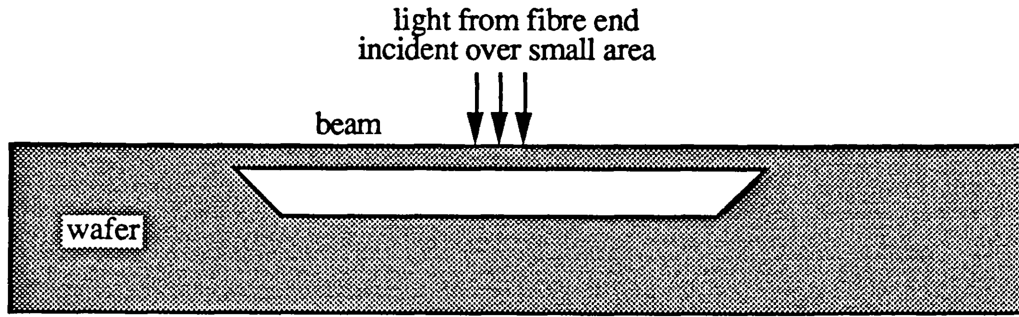

Figure 3.3: Sketch of simple beam on which light is incident.

For example, let us consider a simple beam of thermally grown silicon dioxide of length 230µm, width 5.0µm and thickness 0.5µm coated with evaporated aluminium of thickness 200nm. These dimensions are typical of those of the beams examined in this project.

In this case the intensity of the incident light is assumed to be uniform over a 5µm by 5µm square area on the surface of the beam. In order for the beam to be driven into vibration, some of this light must be absorbed. The absorption coefficient β depends on the optical frequency of the incident light:

$$\beta = \frac{4\pi}{\lambda} K \qquad \{3.13\}$$

where K is the absorption index of the metal and λ is the wavelength of the light. In the bulk material the energy density falls by a factor of e over a depth of $u_{opt.}$ where

$$u_{opt.} = \frac{1}{\beta} = \frac{\lambda}{4\pi K} \qquad \{3.14\}$$

The metals under consideration have $K > 4$, and we are concerned with wavelengths of 1.3µm or less. The optical penetration depths are therefore less than 26nm, and the metals may be considered optically thick.

3:3.1.2 Steady Component of the Incident Light

Consider first the steady component of absorbed intensity

$$\Psi_{steady} = \Psi_0 + \Psi_{det} \qquad \{3.15\}$$

Convection and radiation losses from the beam are negligible, and thus to a first approximation the heat flow may be considered to occur only longitudinally through the beam so that surfaces of sectional planes are isothermals. The relatively large area of metal coating the remainder of the wafer will act as a heat sink and is assumed to be at room temperature. Thus the heat is conducted along each half of the beam. In this case Fourier's Law of heat conduction [10] gives

$$dQ = k\, A \frac{T}{L/2}\, dt \qquad \{3.16\}$$

where dQ is the heat transferred across the metal cross-sectional area A in time dt, k is the thermal conductivity of the metal, T is the temperature rise at the centre of the beam, and L is the beam length. Conduction of heat through the beam substrate is ignored since the thermal conductivity of silicon dioxide is about 0.1% of that of aluminium.

Since we are considering each half of the beam,

$$\frac{dQ}{dt} = \frac{\Psi_{steady}}{2} \qquad \{3.17\}$$

From eqn.{3.16} we derive that

$$T = \frac{(\Psi_0 + \Psi_{det.})\, \beta L}{4 k A} \qquad \{3.18\}$$

We obtain a value of $T \approx 4K$ for values of $\Psi_0 = 100\mu W$, $\Psi_{det.} = 100\mu W$, $\beta = 0.08$, material data (given in Appendix A) and dimensions as given above, we obtain $T \approx 4K$. This model for steady heat flux is as shown in figure 3.4.

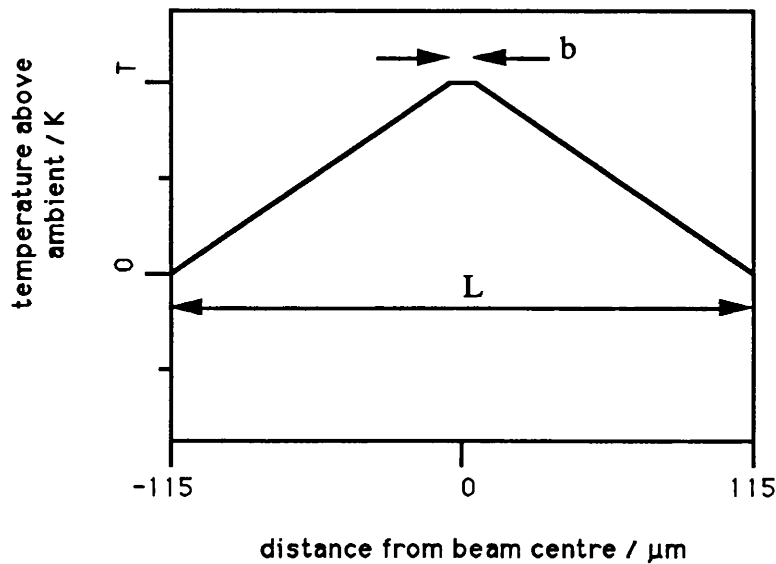

Figure 3.4: Steady component of temperature of beam coating.

Since $b \ll L$, the mean steady temperature rise across the length of the beam is therefore

$$T_{mean} = \frac{T}{2} \qquad \{3.19\}$$

In this case, $T_{mean} \approx 2K$.

The curvature of a bimaterial strip element subjected to an overall temperature rise ΔT is [11]

$$\chi = \frac{6(\alpha_1 - \alpha_2)\Delta T}{\left\{(E_1 a_1^2 - E_2 a_2^2)^2 / (E_1 E_2 a_1 a_2 (a_1 + a_2))\right\} + 4(a_1 + a_2)}$$

{3.20}

where a is the material thickness, and the suffixes 1 and 2 denote the materials of higher and lower expansivity. The bend shape of the beam is approximated to the standard buckle shape

$$y = X\left(1 - \cos\frac{2\pi x}{L}\right) \qquad \{3.21\}$$

Although the form of the optical excitation is expected to distort the bend shape, the standard buckle shape nevertheless provides a useful approximation for our model. Then for small deflections

$$\chi = \frac{\dfrac{d^2y}{dx^2}}{\left\{1 + \left(\dfrac{dy}{dx}\right)^2\right\}^{3/2}} \approx \frac{d^2y}{dx^2} = X\left(\frac{2\pi}{L}\right)^2 \cos\frac{2\pi x}{L} \qquad \{3.22\}$$

The curvature at the beam ends is therefore of the opposite polarity to the curvature in the beam centre. This can be seen in figure 3.5, which shows a sketch graph of the curvature along the beam length. The effect of the differential temperature rise near the beam ends, which is smaller than the differential temperature rise at the centre (figure 2.3), is therefore to decrease the central deflection.

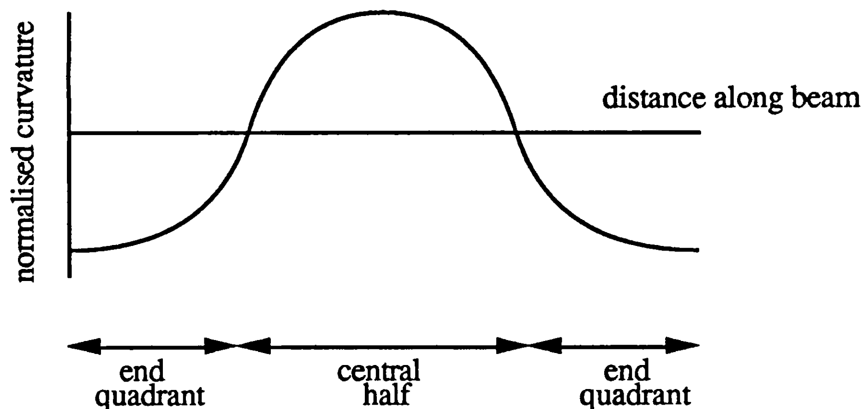

Figure 3.5: Sketch graph of curvature along beam length.

In order to calculate the central deflection Δ_0 using eqn.{3.20} we may account for this bend shape by substituting an appropriately biased temperature for δT. This is calculated by assuming a differential temperature over the central half only. The effect of the differential temperature over the end quadrants is accounted for by subtracting the mean differential temperature over the end quadrants from that over the central quadrants, which gives a mean temperature of $T/2$.

Since we have assumed a differential temperature over the central half only, we substitute $T/4$ into eqn.{3.20}.

Then for the typical beam described above, we obtain $\chi \approx 41 m^{-1}$, and from simple geometry, we calculate that $\Delta_0 \approx \underline{0.3 \mu m}$

3:3.1.3 Oscillatory Component of the Incident Light

Consideration of the oscillatory component of the incident light will allow us to derive an expression for the amplitude of resonant vibrations. Fourier's equation cannot be applied to the oscillatory component of heat flux since the frequency of applied energy is too high. The penetration depth of thermal waves is of the order of the thermal diffusion length $z_{therm.}$ where

$$z_{therm.} = \sqrt{\frac{2k}{\rho \omega C}} \qquad \{3.23\}$$

where ω is the angular modulation frequency and C is the thermal capacity.

Thermal diffusion lengths at 100KHz for the materials under consideration here are as shown in table 3.1.

Material:	SiO_2	Si	Al	Au
$u_{therm.}$ / μm:	0.65	17	17	20

Table 3.1: Thermal diffusion lengths at 100KHz.

The beams may therefore be considered thermally thin, that is their thicknesses are significantly smaller than their thermal diffusion lengths, but not thermally short, since their lengths are not significantly smaller than their thermal diffusion lengths. It is therefore necessary to analyse the heat flow along the length of the beams.

To analyse heat flow we consider the beam to be a strip of metal insulated along its upper and lower surfaces except at an infinitesimal centre spot where the laser-light is incident. In the case of a silicon dioxide beam such as that specified above, at the frequencies considered here the heat flow through the substrate along the length of the beam will be negligible since the diffusion length is so small (see above). Since the beam is thermally thin, we can model the heat as being generated at a cross-sectional plane at the beam centre, as shown in figure 3:5.

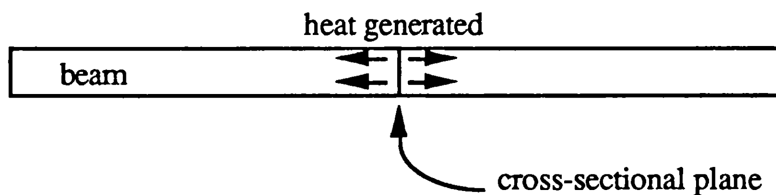

Figure 3.5: Model of beam with heat generated at cross-sectional plane.

Each half of the beam can now be considered as a slice from a semi-infinite solid illuminated by an optical flux of intensity

$$\Psi_0 \, m \cos(2\pi ft) / A_m$$

where A_m is the cross-sectional area of the metal.

This is shown in figure 3.6. Each beam half is effectively illuminated at its end surface.

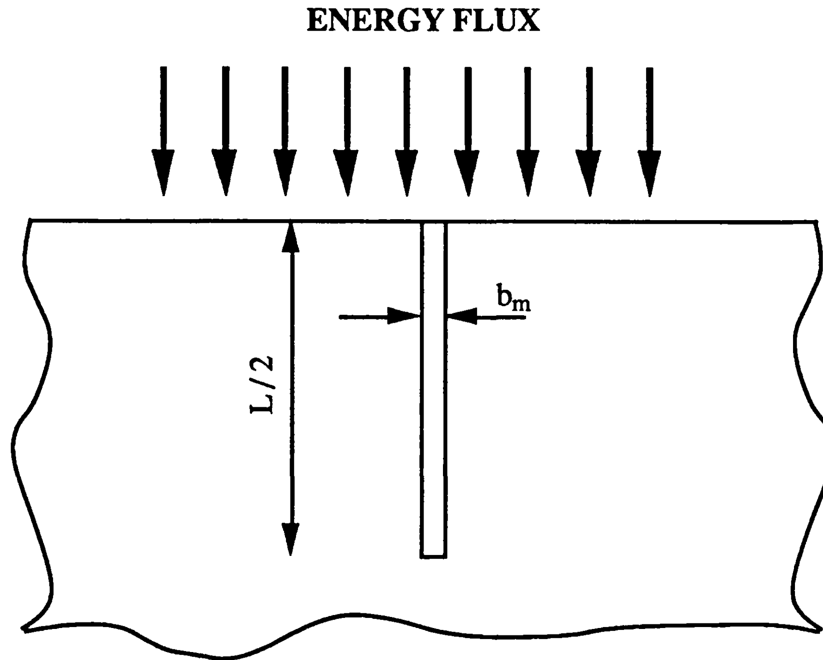

Figure 3.6: Half-beam considered as a strip from an illuminated semi-infinite solid.

The oscillatory component of temperature can then be found by solving the diffusion equation [10]

$$\nabla^2 T - \frac{1}{\kappa} \cdot \frac{\delta T}{\delta t} = 0 \qquad \{3.24\}$$

where T is the oscillatory component of temperature and κ is the thermal diffusivity of the metal so that

$$\kappa = \frac{k}{\rho C} \qquad \{3.25\}$$

Solving the diffusion equation gives us a distribution of the oscillatory component of temperature at a distance x from the beam centre in either direction

$$T = \frac{\beta \Psi_0}{A m \sqrt{k \rho C \omega}} \exp\left\{ -x \sqrt{\frac{\omega}{2\kappa}} \right\} \cos\left\{ \omega t - x \sqrt{\frac{\omega}{2\kappa}} - \frac{\pi}{4} \right\}$$

{3.26}

The form of this temperature distribution along the beam length is shown in figure 3.7 at intervals of one eighth of a cycle, relative to an arbitrary phase θ.

The mean oscillatory component of temperature along the beam length is therefore

$$T_{mean} \approx \frac{2 \beta \Psi_0}{L A m \sqrt{k \rho C \omega}} \int_0^{L/2} \exp\{-\phi x\} \cos\{\omega t - \phi x - \frac{\pi}{4}\} \, dx \qquad \{3.27\}$$

where $\phi = \sqrt{\frac{\omega}{2\kappa}}$

whence

$$T_{mean} \approx \frac{\beta \Psi_0}{\phi L A m \sqrt{k \rho C \omega}} \left(\cos\{\omega t - \frac{\pi}{4}\} + \sin\{\omega t - \frac{\pi}{4}\} \right)$$

$$= \frac{\sqrt{2}\, \beta \Psi_0}{\phi L A m \sqrt{k \rho C \omega}} \cos\{\omega t - \frac{\pi}{2}\} \qquad \{3.28\}$$

In the case of a silicon dioxide beam such as that specified above, although at the frequencies considered here the heat flow through the substrate along the length of the beam will be negligible, heat flow through the thickness of the beam is significant; the substrate will act as a heat storage element so that the effective specific heat capacity of the strip is raised. This factor will depend on the modulation frequency f but to a first approximation we might say that the effective specific heat capacity

$$C_{eff.} = C_m + 0.5 \frac{a_s}{a_m} C_s \qquad \{3.29\}$$

where the suffixes m and s denote the metal and the substrate.

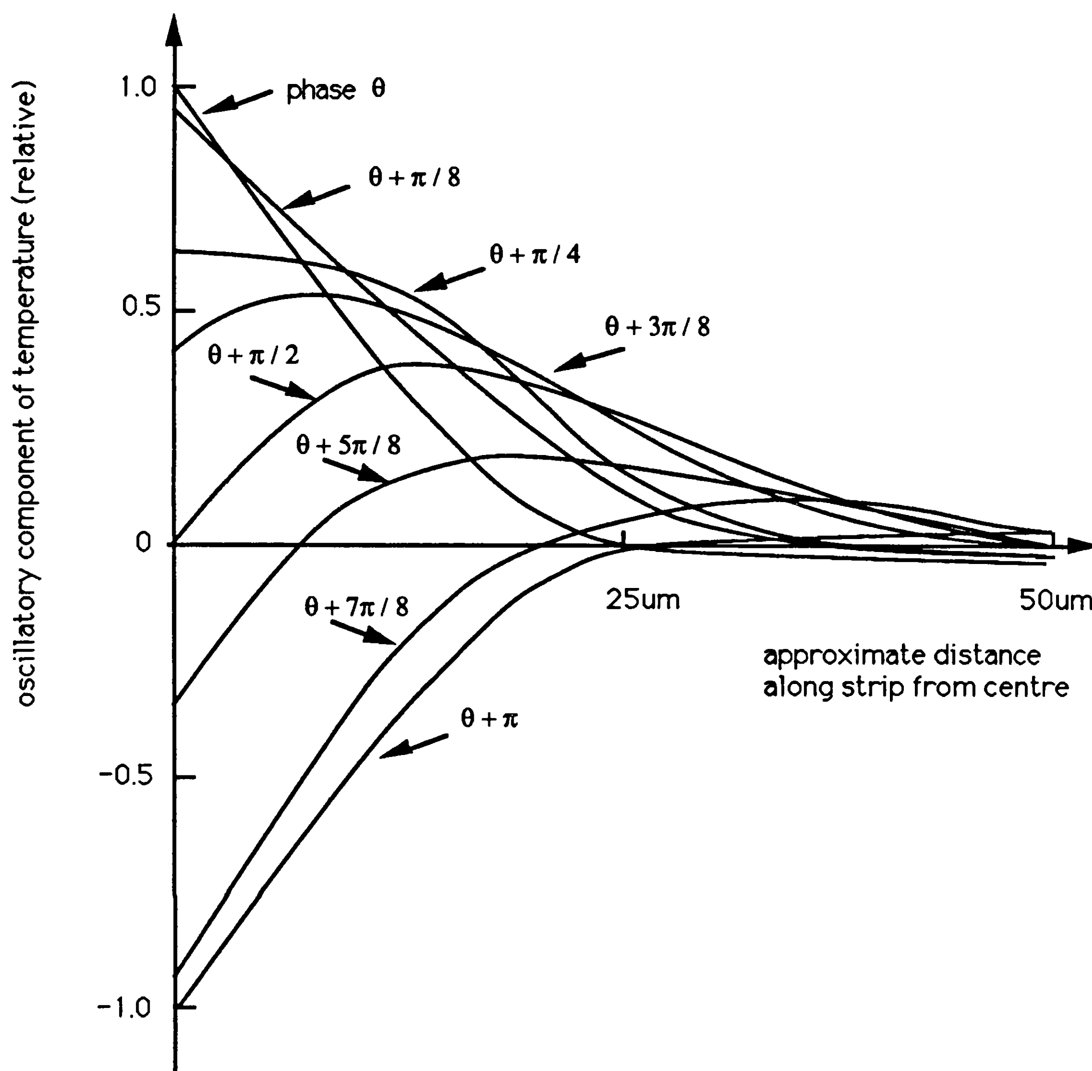

Figure 3.7: Distribution of oscillatory component of temperature along beam at intervals of one eighth of a cycle.

Values of $\Psi_0 = 100\mu W$, $\beta = 0.08$, $m = 1$ and material data (given in Appendix A) are substituted with $C_{eff.}$ as given in eqn.{3.29} and the geometrical values specified above are used so that

$$\frac{\beta \Psi_0}{A m \sqrt{k \rho C \omega}} \approx 0.3 \text{ Kelvin} \qquad \{3.30\}$$

We substitute for L and ϕ in eqn.{3.28} and find

$$T_{mean} \approx 0.02 \text{ Kelvin } \left(\cos\{\omega t - \frac{\pi}{2}\} \right) \qquad \{3.31\}$$

I have assumed that the spatially averaged a.c. component of the thermal energy determines the extent of the photothermal activation, and that the amplitude of vibrations is determined by the maximum value of this averaged quantity. Then substituting T_{mean} into eqn.{3.20} then from simple geometry the oscillatory component of the central beam deflection is $\Delta_{osc.} \approx 0.01\mu m$. The amplitude of resonant vibrations

$$\Delta_{res.} = Q \Delta_{osc.} \qquad \{3.32\}$$

Consideration of Quality Factors

It is first necessary to derive a theoretical expression for the quality factor (Q) of microbeam vibrations, in order to predict the amplitude of resonant vibrations. An expression for the quality factor may be derived from eqn.{3.10} and eqn.{3.11} so that

$$Q = \frac{m \omega_{res}}{R} \qquad \{3.33\}$$

We may obtain an approximate expression for the Q of vibrations of a beam clamped at both ends by substituting ω_{res} for the first mode ($i = 1$) from eqn.{3.2}, and putting $m = \rho a b L$, so that

$$Q \approx \frac{9 \pi^2}{8 \sqrt{3}} \frac{a b^2}{L} \frac{\sqrt{E \rho}}{R} \qquad \{3.34\}$$

At ambient pressures of above around 10^4 Nm^{-2} the dominant mechanism of damping is assumed to be viscous drag [12]. If the air is assumed to be acting as a viscous

fluid, the damping constant may be derived from Stokes' law. Stokes' law for the viscous drag on a circular disc of radius r moving edge on in a fluid of viscosity η gives [10]

$$R = \frac{32\, r\, \eta}{3} \qquad \{3.35\}$$

An approximate value of R for a beam of $b \ll L$ may be obtained by putting $r = L/2$. This value may be substituted into eqn.{3.34} so that

$$Q \approx 0.4\, \frac{a\, b^2}{L^2}\, \frac{\sqrt{E\, \rho}}{\eta_{air}} \qquad \{3.36\}$$

Substituting this expression into eqn.{3.32} using the dimensions given above, and material parameters for SiO_2, gives a quality factor $Q \approx 13$ and amplitude of resonant vibrations $\Delta_{res.} \approx 100\mathrm{nm}$.

It should be remembered that this is an order-of-magnitude estimate of the amplitude of resonant vibrations. This amplitude is clearly sufficient to allow multimode detection schemes, and is also of the same order as the spatial period of interferometric fringes set up between the fibre end and the strip surface. This suggests that not only detection but also activation of vibrations may be possible by using these fringes as a source of temporal intensity modulation. This possibility is further explored in Chapter 6 of this thesis.

It should be noted however that the forgoing discussion and analysis has been based on standard beam theory. We next consider how the microstructures considered in this project may behave in a different way from that suggested by this model.

3:4 Fabrication Induced Effects in Microfabricated Devices

We noted in Chapter 2, Section 2:5, that a number of features of the microresonators fabricated for this project which are expected to effect their performance were observed. In this section we consider the fabrication-induced stress in the beams, and the etch-defined end conditions.

3:4.1 Fabrication-Induced Stress

The description of the fabrication of metal-coated beams as part of silicon microstructures in Chapter 2, Section 2:2, showed how both the silicon beam and the metal layer superimposed upon it were expected to be under fabrication-induced stress.

In order to estimate the effect of these stresses on the resonance frequencies of a metal-coated silicon beam, a mean value for the beam stress σ is substituted into eqn.{3.5}, which relates the resonance frequency of a simple beam to the stress in that beam. This mean stress may be calculated as

$$\sigma = \frac{a_m \sigma_m + a_s \sigma_s}{(a_m + a_s)} \qquad \{3.37\}$$

where σ_m is the mean stress in the metal and σ_s is the mean stress in the silicon.

In practice, after fabrication, the metal-coated silicon beam takes up the position of a stretched element under tension, thus forming a straight beam between the corners of the supporting wafer.

The stress in metal-coated silicon dioxide beams can also be calculated from eqn.{3.37}, where in this case σ_m is the mean stress in the metal and σ_s is the mean stress in the silicon dioxide. The fabrication-induced stress in the oxide is, however, compressive, so that beam bending and stress relief occurs as described in Chapter 2, Section 2:3, and these stress values σ_m and σ_s are no longer the same as the fabrication-induced stresses in the metal and the oxide.

We may calculate the values of the stress in the oxide and in the metal by first deriving an expression for the deflection of the bent beam.

3:4.1.1 Deflection of a Bent Beam

The shape of a bent beam clamped at both ends may be described by [13]

$$y = \Delta' \left\{ 1 - \cos \frac{2\pi x}{L} \right\} \qquad \{3.38\}$$

where Δ' is the central deflection of the bent beam.

Now let δs be a small element along the beam length, as shown in figure 3.8.

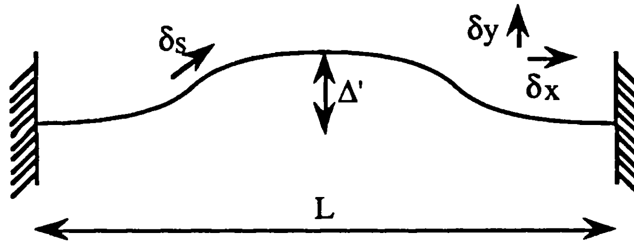

Figure 3.8: Diagram of deflected beam.

Now

$$\left(\frac{\delta s}{\delta x}\right)^2 = 1 + \left(\frac{\delta y}{\delta x}\right)^2 \qquad \{3.39\}$$

Therefore

$$\frac{ds}{dx} = \left\{ 1 + \Delta'^2 \left(\frac{2\pi}{L}\right)^2 \sin^2\left(\frac{2\pi x}{L}\right) \right\}^{1/2} \qquad \{3.40\}$$

and since $\Delta \ll 1$,

$$\frac{ds}{dx} \approx \left\{ 1 + \frac{2\pi^2 \Delta'^2}{L^2} \sin^2\left(\frac{2\pi x}{L}\right) \right\} \qquad \{3.41\}$$

then

$$\int_0^S ds \approx \int_0^L \left\{ 1 + \frac{2\pi^2 \Delta'^2}{L^2} \sin^2\left(\frac{2\pi x}{L}\right) \right\} dx \qquad \{3.42\}$$

where S is the extended beam length, so that

$$S = L + \Delta L = L + \frac{\pi^2 \Delta'^2}{L} \qquad \{3.43\}$$

$$\Delta L = \frac{\pi^2 \Delta'^2}{L} \qquad \{3.44\}$$

We now use this expression to calculate the stress in the deflected beam.

3:4.1.2 Stress in a Deflected Beam

An approximate expression for the beam stress may be derived by ignoring any stress distributions through the oxide or through metal, so that mean stresses σ_m and σ_s are assumed to apply throughout the beam.

When the deflected oxide beam is metal-coated, some of the tension in the metal will be relieved by straightening (shortening) of the beam, putting the oxide back under compression. The equilibrium deflection can be found by considering the internal forces in the bimaterial beam. Using this model, which is an approximation to the real case, we may consider the vertical components of the equal and opposite forces on the metal and the substrate, shown in figure 3.9.

However we know that the central deflection Δ' of a beam clamped at both ends under the influence of such a force of magnitude F is [14]

$$\Delta' = \frac{F L^3}{384 E I} \qquad \{3.45\}$$

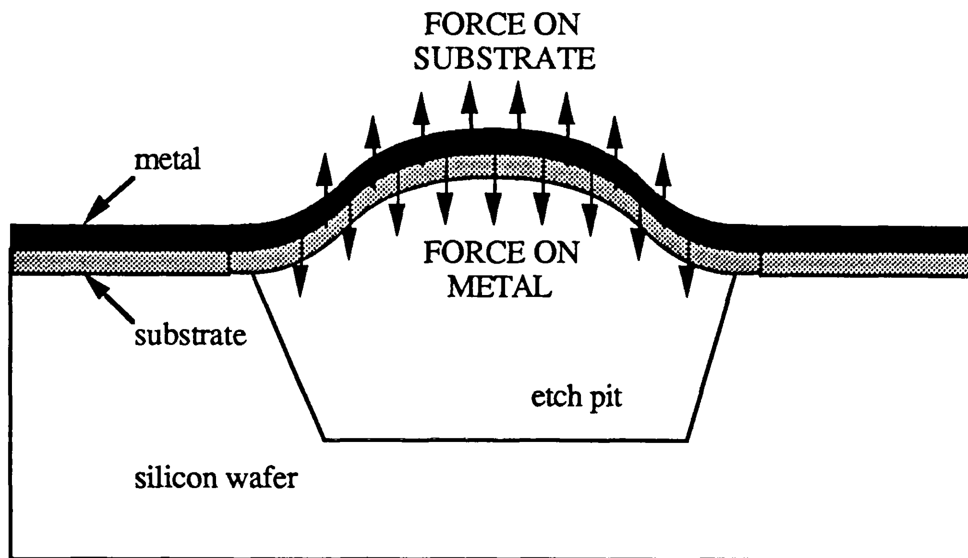

Figure 3.9 Internal forces in metal-coated silicon dioxide beam.

The equilibrium central deflection of the beam will be

$$\Delta_o = \Delta_s + \Delta'_s = \Delta_m - \Delta'_m \qquad \{3.46\}$$

where Δ_s is the deflection at which the stress in the oxide is zero (i.e. the deflection before the beam is metal-coated), and Δ_m is the deflection at which the stress in the metal is zero. Note that Δ'_s is the effective deflection of the oxide, and Δ'_m is the effective deflection of the metal.

Therefore, using eqn.{3.45}

$$(\Delta_o - \Delta_s)\left(\frac{384\, E_s I_s}{L^3}\right) = (\Delta_m - \Delta_o)\left(\frac{384\, E_m I_m}{L^3}\right) \qquad \{3.47\}$$

whence

$$\frac{(\Delta_o - \Delta_s)}{(\Delta_m - \Delta_o)} = \frac{E_m a_m^3}{E_s a_s^3} \qquad \{3.48\}$$

From eqn.{3.43} above the strain equivalent to a central deflection Δ' is

$$\varepsilon = \frac{\pi^2 \Delta'^2}{L^2} \qquad \{3.49\}$$

Therefore, substituting from {3.46}

$$\frac{\varepsilon_s}{\varepsilon_m} = \frac{E_m^2}{E_s^2}\,\frac{a_m^6}{a_s^6} \qquad \{3.50\}$$

Whence

$$\frac{\sigma_s}{\sigma_m} = \frac{E_m}{E_s}\,\frac{a_m^6}{a_s^6} \qquad \{3.51\}$$

The overall force in the beam causing an additional bending moment term in eqn.{3.1} may to a first approximation be considered to be the sum of the oxide and metal forces. Thus it can be seen from eqn.{3.51} that if $a_m < a_s$ then the nett stress is tensile so that the resonance frequency will be higher than predicted by eqn.{3.2}. If $a_m > a_s$ then the nett stress is compressive and the resonance frequency will be lower than predicted by eqn.{3.2}. The effect of fabrication-induced stress is thus to reduce the resonance frequency as the metal thickness is increased.

A general expression for the mean stress in the metal-coated silicon dioxide beam is obtained as follows: rearranging eqn.{3.51} and substituting values for Young's modulus for silicon dioxide and aluminium or gold,

$$\Delta_0 (1+h) = \Delta_s + h\,\Delta_m \qquad \{3.52\}$$

where $h \equiv (a_m/a_s)^3$. Then, using eqn.{3.49}, we obtain

$$\Delta_0 = \frac{L}{(1+h)\,\pi}\left[\sqrt{\frac{\sigma_A}{E_s}} + h\sqrt{\frac{\sigma_A}{E_s} - \frac{\sigma_B}{E_m}}\right] \qquad \{3.53\}$$

where σ_A is the magnitude of the fabrication-induced compression in the silicon dioxide, σ_B is the magnitude of the fabrication-induced tension in the metal, and it is assumed that $\sigma_A > \sigma_B$.

The stress in the silicon dioxide σ_s is derived from this to be

$$\sigma_s = -\sigma_A + H E_s \qquad \{3.54\}$$

and the stress in the metal to be

$$\sigma_m = \sigma_B - \sigma_A + H E_m \qquad \{3.55\}$$

where

$$H \equiv \frac{1}{(1+h)^2}\left[\sqrt{\frac{\sigma_A}{E_s}} + h\sqrt{\frac{\sigma_A}{E_s} - \frac{\sigma_B}{E_m}}\right]^2 \qquad \{3.56\}$$

Using eqn.{3.37} for the mean beam stress in terms of the stress in the oxide and the stress in the metal, the mean beam stress is

$$\sigma = \frac{a_m(\sigma_B - [\sigma_A - H E_m]) + a_s(\sigma_A - H E_s)}{a_m + a_s} \qquad \{3.57\}$$

And if $E_m = E_s$ then

$$\sigma = \left\{\frac{a_m}{a_m + a_s}\right\}\sigma_B - \sigma_A + \frac{\left\{\sqrt{\sigma_A} + h\sqrt{\sigma_A - \sigma_B}\right\}^2}{(1+h)^2} \qquad \{3.58\}$$

This general approximate expression for the mean beam stress may also be used to predict the temperature-dependent behaviour of a metal-coated silicon dioxide beam. This analysis is carried out in Chapter 5, Section 5:2.2.

3:4.2 Effect of Etch-Defined End Conditions

The webbed beam ends described in Chapter 2, Section 2:4.1, cannot be described by the clamped or pinned conditions used in the standard theory described earlier in this chapter in Section 3:2.1.1. This is because the beams are restrained over a significant proportion of their lengths.

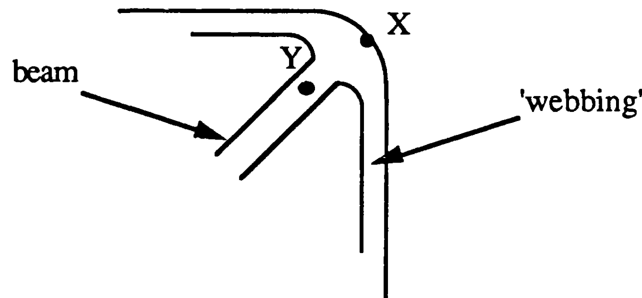

Figure 3.10: Schematic Plan of beam end.

A webbed beam end is illustrated in figure 3.10 and can be described in approximate terms as follows:
At the point 'X' in figure 3.10 the beam material (SiO_2 or doped Si) can be thought of as clamped to the silicon substrate, since here the beam material cannot separate from the bulk of the wafer so that dy/dx, the upward slope of the beam material, will be zero. Between the points 'X' and 'Y' the beam is still restrained, here by the ledges of beam material. Along this section of the beam is expected to be a dramatic change in restoring force.

It is suggested that this non-trivial end-condition may allow two sets of vibrational modes, so that an alternative end condition parameter may be substituted in the equation for the resonance frequencies of the beam (eqn.{3.2}), modelling both the clamped beam ends and the points near the ends. The experimental behaviour of the resonators is therefore to be tested against this hypothesis.

3:4 Conclusions

We have modelled the mechanical behaviour of these beams using the hypothesis that standard beam theory developed for studying macrostructures can be extrapolated to describe these microstructures also.

The standard beam theory is considered to be adequate for an analysis of experimental results in terms of the geometry, materials and end-conditions microresonators. A notable exception is the case of the variation of resonance frequency of an SiO2 beam with metal coating thickness. In this case the stress distribution through the beam is more complex and a model is proposed in which the deflected shape of the beam changes to accommodate some of the fabrication-induced stress in the metal. In addition the non-standard etch-defined end conditions result in more complex structures which may exhibit additional modes, and an additional analysis is required to test this hypothesis. The experimental characterisation and analysis is carried out in the following chapter.

We have also modelled the opto-thermal excitation process quantitively, and the amplitude of resonance vibrations is calculated to be of the order of 100nm superimposed on a steady beam deflection. The amplitude is clearly sufficient to allow multimode detection schemes, and is also of the same order as the spatial period of interferometric fringes set up between the fibre end and the strip surface. This suggests that not only detection but also activation of vibrations may be possible by using these fringes as a source of temporal intensity modulation. The possibility is further explored in Chapter 6 of this thesis.

In addition it is noted here that the feasibility of a finite element method of analysis has also been explored using a general purpose engineering analysis system. The finite element model has been used to predict resonance frequencies of simple microresonator beams broadly in agreement with those predicted by the standard beam theory. The detailed results of this analysis are complex, and outside the scope of this thesis.

References for Chapter 3

1. S.P.Timoshenko *et al.*; "Vibration problems in Engineering"; John Wiley and Sons, 1974
2. Blevins; "Formulas for Natural Frequency and Mode Shape"; Van Nostrand Reinhold Company, New York, 1979
3. W.C.Albert; *"Vibrating Quartz Crystal Accelerometer"*; 28th int.instrum.symp., Las Vegas, USA, 1982, pp33-34
4. C.R.Pelts & H.K.Wickramasinghe; *"Photothermal Spectroscopy on a Microscopic Scale"*; 1981 Ultrasonics Symposium, pp832-836
5. A.Rosencwaig & G.Busse; *"High Resolution Photoacoustic Thermal Wave Microscopy"*; App. Phys. Lett., vol.36(9), 1980
6. G.Busse & A.Rosencwaig; *"Subsurface Imaging with Photoacoustics"*; App.Phys.Lett., vol.36(10), 1980
7. H.K.Wickramasinghe *et al.*; *"Photoacoustics on a Microscopic Scale"*; App.Phys.Lett., vol.33(11), 1978
8. F.A.McDonald & G.C.Jr.Wetsel; *"Generalized Theory of the Photoacoustic Effect"*; J.Appl.Phys., Vol.49(4), 1978
9. A.Rosencwaig & A.Gersho; *"Theory of the Photoacoustic Effect with Solids"*; J.Appl.Phys., vol.47(1), 1976
10. T.S.E.Thomas; *"Physical Formulae"* (Methuen & Co. Ltd., London, 1953)
11. L.E.Andreeva; "Elastic Elements of Instruments"; IPST Ltd., Moscow, 1980, pp180-182
12. W.E.Newell; *"Miniaturisation Of Tuning Forks"*; Science, Vol. 161, pp1320-1326, 1968
13. D.L.Shodek; "Structures"; Prentice Hall, London, 1980
14. Cambridge University Engineering Department; "Structural Data, Formulae and Section Tables"; 1973 (unpublished)

CHAPTER 4: OBSERVATION OF MICRORESONATOR VIBRATIONS

4:1 Introduction

4:2 Experimental Methods
- 4:2.1 Two-Source Fibre-Optic System
- 4:2.2 Fibre-Optic System with Pigtailed Source
- 4:2.3 Phase-Lock System

4:3 Vibrational Characterisation
- 4:3.1 Detection and Activation Power
- 4:3.2 Silicon Dioxide Microresonators: Mode Relationships
- 4:3.3 Variation of Resonance Frequency with Beam Length
- 4:3.4 Variation of Resonance Frequency with Metal Thickness
- 4:3.5 Silicon Microresonators: Mode Relationships
- 4:3.6 Consideration of Quality Factors

4:4 Electrical Excitation
- 4:4.2 Capacitive Drive
- 4:4.2 Resistive Drive

4:5 Conclusions

References for Chapter 4

CHAPTER 4

OBSERVATION OF MICRORESONATOR VIBRATIONS

4:1 Introduction

The devices described in Chapter 2 may be manufactured relatively easily and cheaply on a large scale using the micromachining technologies developed for the microelectronics industry; they are small enough to be driven into oscillation using low values of optical power (tens of microwatts) and to be physically compatible with a fibre probe. There is to date no published experimental work from elsewhere on the vibrational behaviour of optically excited micoresonators similar to those described here.

When this project commenced in 1986, in line with the objectives outlined in Chapter 1, we concentrated initially on improving the activation and detection schemes and making an experimental characterisation of the vibrations of these microbeams. The behaviour of the beams may be compared with the mathematical model described in Chapter 3. Attempts were also made to vibrate beams of different silicon-based materials but of the same or similar geometries and using the same fibre-optic system, and to examine some electrical methods of exciting our devices.

4:2 Experimental Methods

Systematic studies of the vibrational behaviour of simple optically excited microresonator beams were carried out. Since the objective was to develop a fibre-optic probe sensor involving no bulk optical components an all-fibre system has been developed for this work. This system has been developed from one involving heterodyne detection [1] and originally from a bulk optics system [2].

4:2.1 Two-Source Fibre-Optic System

The activation and detection of vibrations is achieved using the single-mode fibre system shown schematically in figure 4.1. The fibre is single-moded at 820nm. Two identical fused fibre directional couplers with a split ratio of 50% at 820nm and an insertion loss at this wavelength of less than 0.2dB are spliced together as shown. The optical drive is provided by a 2mW HeNe laser emitting at 633nm modulated by a Bragg cell driven at 80MHz. The modulation drive for the Bragg cell is a microprocessor controlled synthesiser/function generator (hp3325A) which may be programmed to sweep a sinusoidal output over a preselected range of frequencies for a duration of up to 99 seconds. The light from this laser is coupled into the first fibre coupler using a x20 microscope objective. At 633nm the fibre supports two modes and the couplers have a split ratio of approximately 3:1. They are arranged so that the light from this laser passes through to the micromechanical device under study in the direction of maximum power throughput. The second source, which is used for detection of vibrations, is a GaAs 1.5mW laser emitting at 820nm. The light from this laser is coupled into the second fibre coupler in the same direction as the 633nm light using a x10 microscope objective.

The fibre end from the second coupler was held within a few microns of the surface of the micromechanical device under study. Using an optical microscope, the fibre end was butted against the wafer surface, and then the wafer moved away, with the distance being measured on the voltage-controlled three-axis micropositioner on which the micromechanical device is mounted. The micropositioner has a manual range of travel of 1cm and resolution of $\pm 5\mu m$ and a voltage-controlled range of $15\mu m$ and resolution of $\pm 50nm$ after calibration. The fibre is orientated perpendicular

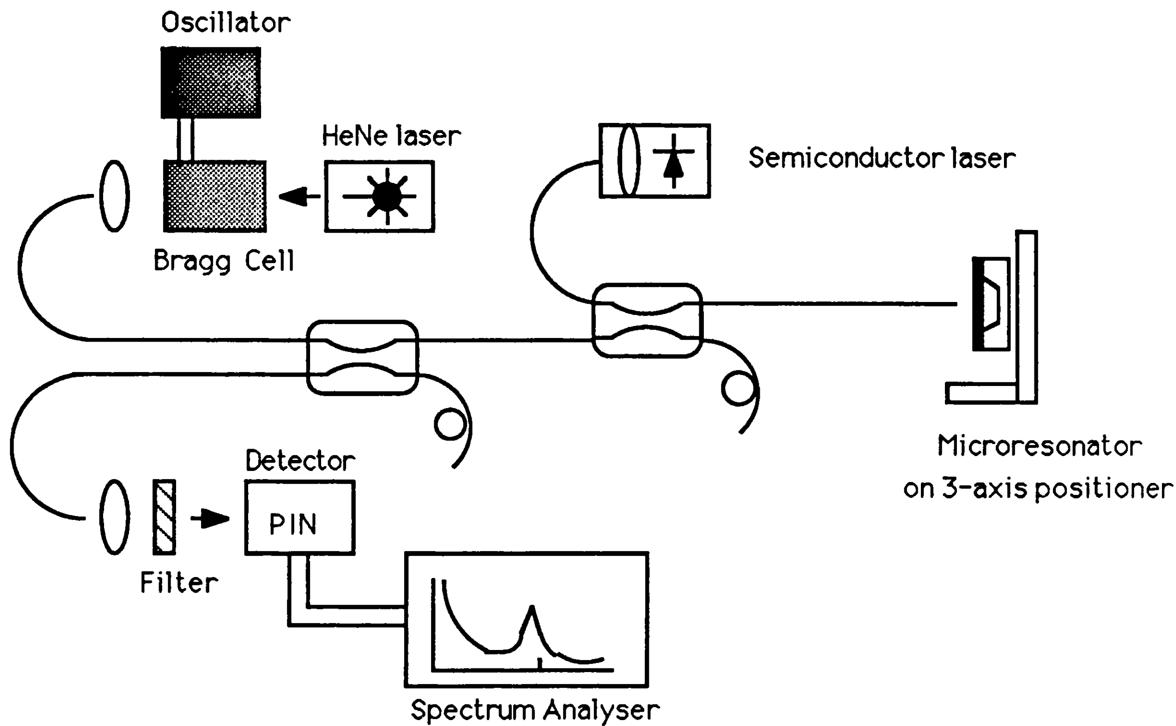

Figure 4.1 Schematic of two-source fibre-optic system for activation and addressing of microresonator vibrations.

to the device to within about 5 degrees. The fibre end is cleaned with iso-propyl alcohol. A proportion of the light reflected back from the metal-coated surface of the micromechanical device under study is thus launched back into the same fibre. A proportion of this light is then guided through the couplers, and focused onto the photodetector using a x10 microscope objective. The reflected light from the activating laser is filtered out using a wavelength-selective filter centred at 633nm with a throughput of 0.05dB at 633nm and a throughput loss of less than 0.1dB at 820nm. The photodetector is constructed using a silicon PIN diode and has a measured flat frequency response from 0 to 50MHz with a 10dB cut-off at 80MHz. The amplified output of the photodiode is examined with a spectrum analyser (hp8568B, 100Hz-1.5GHz) or CRO.

The light emerging from the fibre end at the device is directed at the central area of the microresonator beam unless otherwise specified. The metal-coated device absorbs some of the intensity-modulated light incident upon it, producing a thermal modulation, to which the microresonator beam, being constrained at both ends, responds by vibrating in a flexural mode. Any intensity modulation imposed on the reflected read beam is monitored on the spectrum analyser or CRO.

The resonance frequencies of the microresonators can be identified by sweeping the modulation frequency of the Bragg cell and observing the position of the maximum intensity modulation imposed on the read beam. The quality factor Q of each resonance can be found by measuring the 3dB bandwidth Δf of the resonance peak at frequency f_{res}, since for any resonance system [3]

$$Q = \frac{f_{res}}{\Delta f} \qquad \{4.1\}$$

For the optimised system the detected signals are typically a few tens of dB above noise levels if a few tens of microwatts are available to drive the vibrations.

4:2.2 Fibre-Optic System Using Pigtailed Source

As a further step towards the demonstration of a practical system the 820nm laser and associated launch optics were replaced by a 1.3μm STC GaInAsP 1mW pigtailed semiconductor laser.. This was designed so that the laser power output could be ramped using an external potentiometer. The silicon photodiode was replaced by a germanium photodiode with a peak response at 1.3μm. The 820nm couplers were replaced by fused fibre directional couplers with a split ratio of 50% at 1.3μm and an insertion loss at this wavelength of less than 0.1dB. The fibre is single-moded at 1.3μm. At 633nm the fibre supports four modes and the couplers have a split ratio of approximately 9:1. They are arranged so that the light from the activating (HeNe) laser passes through to the micromechanical device under study in the direction of maximum power throughput.

4:2.3 Phase-Lock System

A feedback system for dual-supply optical activation which does not require sweeping of the modulation frequency of the activating light was designed and implemented. This system uses a phase-lock loop to enable the modulating source to automatically lock onto and then track the mechanical resonance of the micromechanical device. This is feasible because in any resonance system there is a constant phase difference at the resonance frequency between the drive (in this case the modulation input to the activating laser) and the fundamental component of the output at the same frequency [3]. Near resonance this phase difference exhibits a first order linear relationship with frequency.

Figure 4.2 shows a sketch of the variation of vibration amplitude with frequency of a typical resonator under two different environmental conditions C_1 and C_2. The phase of the resonator position relative to that of the drive is also shown. The phase of the two signals can be compared by using a phase shifter to adjust the output phase by the required difference and a phase comparator. The error voltage from the phase comparator is fed into the voltage-controlled oscillator (VCO) supplying the input modulation to effect a lock.

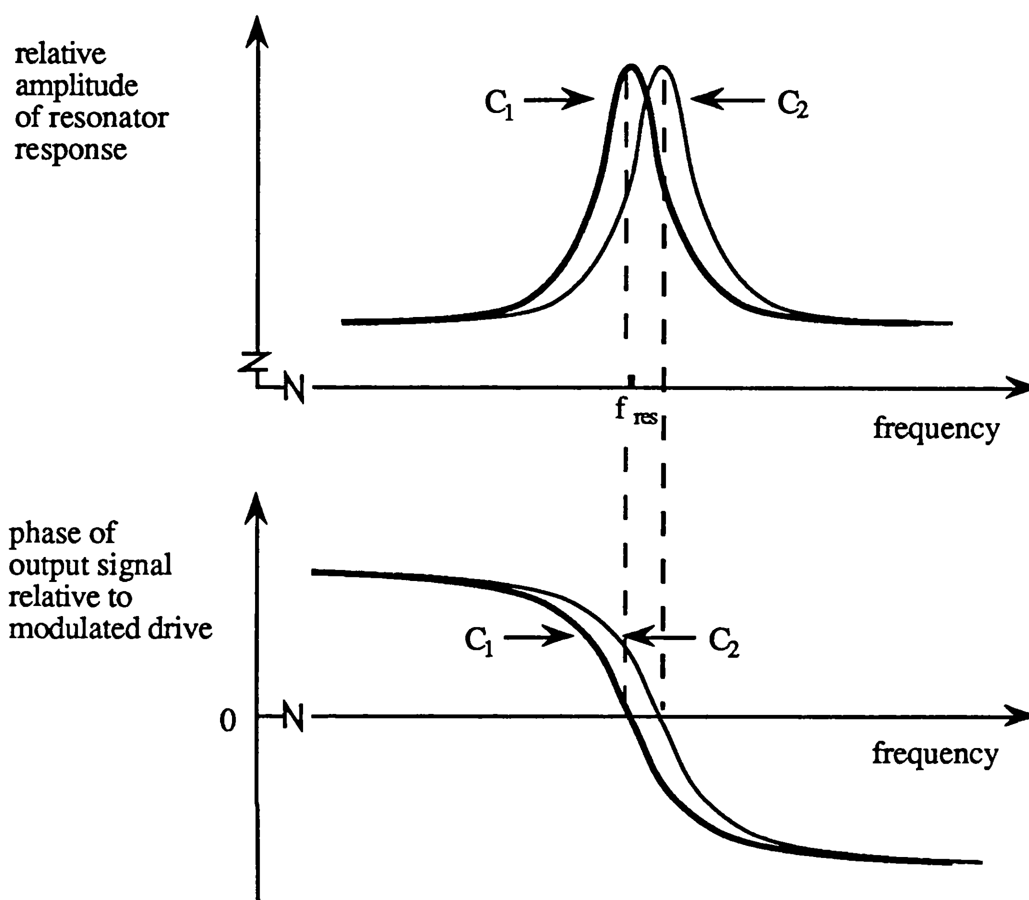

Figure 4.2: Sketch of the relationship of amplitude and phase to frequency

The system is shown schematically in figure 4.3. The phase lock loop was designed to have a centre frequency, which is the free running frequency of the VCO, adjustable in the range 90-250KHz. The detection bandwidth, which corresponds to the loop capture range, was set at 17KHz with zero skew. The lock range was measured by adjusting the centre frequency using a variable resistor in the phase lock loop circuitry, to be 21KHz.

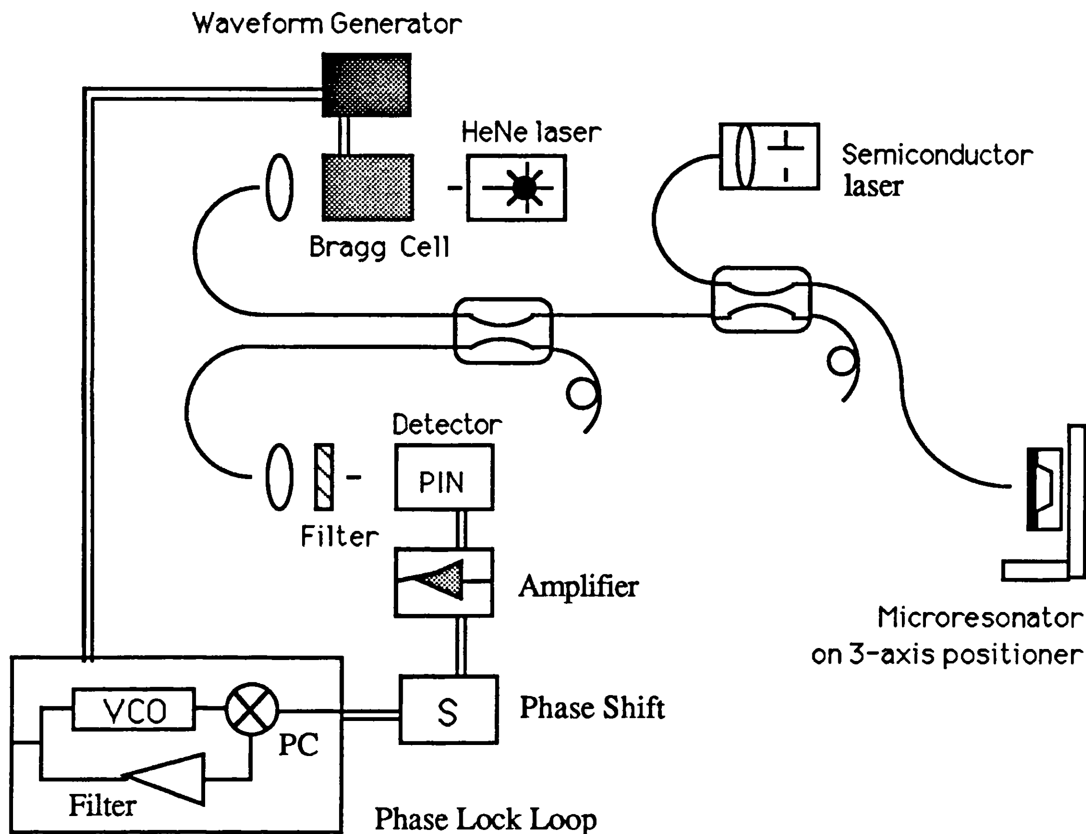

Figure 4.3: Schematic of fibre-optic system incorporating phase lock detection

The system was tested using five metal-coated silicon dioxide micromechanical resonator beams. These were characterised vibrationally initially using the frequency sweep system shown in figure 4.1. The lowest resonance frequencies of these beams were found to be between 105KHz and 163KHz, with quality factors of between 18 and 39. The SNR at resonance was between 25 and 40dB. In each case when the detection power was applied the drive modulation locked onto this frequency and remained in lock for 60 minutes. In two cases the resonance frequencies of the beams was altered by up to 4% by adjusting the temperature of the device substrates by up to 20^{0}C. In these cases lock was maintained through a full temperature cycle.

It was demonstrated that a feedback system may be used to optically drive microresonator vibrations at around 130KHz.

4.3 Vibrational Characterisation

The experimental methods described in Section 4:2 of this chapter were used to examine the vibrational behaviour of micromechanical devices. This section describes results of this examination.

4:3.1 Detection and Activation Power

The spectrum of the return signal was examined as the modulation frequency of the Bragg cell was swept steadily from 0 to a few hundred KHz. It was found that the imposed modulation on the return optical signal at the frequency of optical activation reached a maximum at certain modulation frequencies. An example of this response is shown in figure 4.4a, a spectrum analysis between 0 and 40KHz of the return signal when the activating laser is modulated at a resonance frequency of the device under test, 371KHz.

Figure 4.4b shows the response between 80 and 120KHz of a similar device. In this figure a second trace can be seen superimposed over the simple response. At each frequency this second trace holds its maximum value while the modulation frequency of the activating laser is swept across the full range of frequencies shown over a period of 60 seconds.

The magnitude of the signal maxima at these resonance frequencies could be measured on the spectrum analyser and was found to depend critically on the optical power incident on the micromechanical device. This power was measured indirectly after launch and before the device was set into vibration using a large area optical power meter. It is not possible to calculate the power of the 633nm light from a direct measurement at the free fibre end (see figure 4.1) because the split-ratio of the fibre couplers is dependent on the modal nature of the launch.

I was able to activate and detect vibrations in two separate devices at 97KHz and 137KHz. Both were silicon dioxide microbeams fabricated on silicon wafers and evaporation coated with a thin layer of aluminium, similar to those examined in section 4:3.2 below.

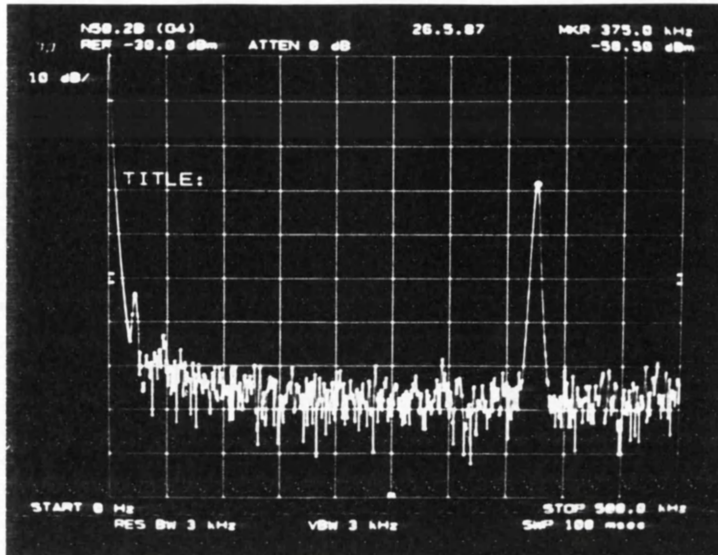

Figure 4.4a: Spectrum of reflected signal from of microresonator strip vibrating at a resonance frequency of 371KHz. Frequency 0 to 500KHz; Amplitude 10dB/division.

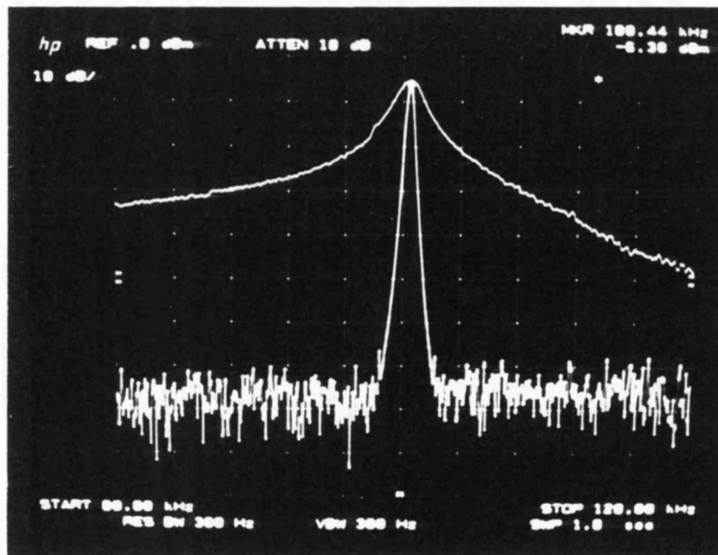

Figure 4.4b: Spectrum of reflected signal from of microresonator strip vibrating at a resonance frequency of 101KHz. Frequency 80 to 120KHz; Amplitude 10dB/division.

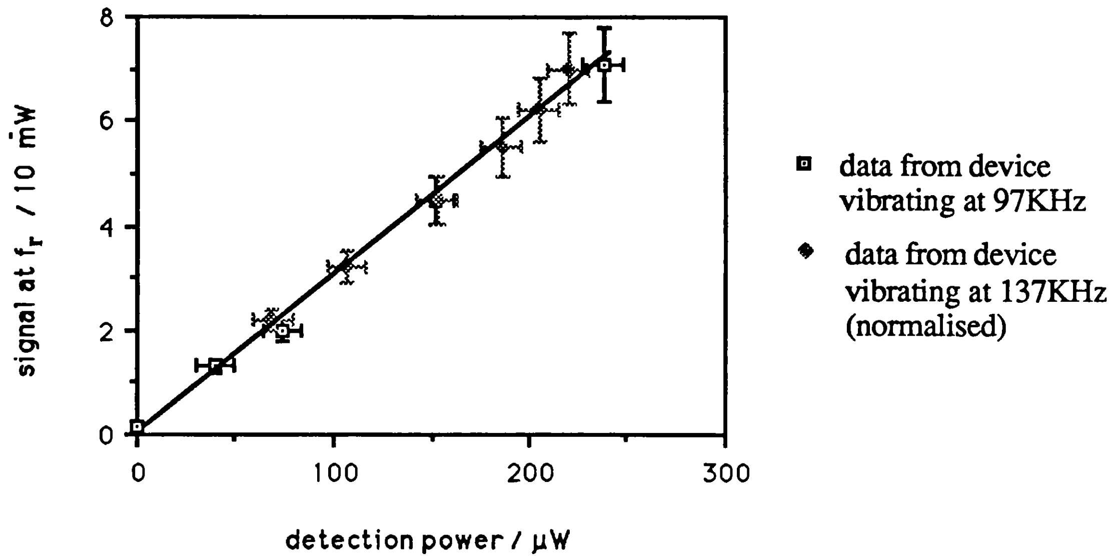

Figure 4.5: Amplitude of received signal at frequency of resonance plotted against incident power of intensity modulated drive

The return signal at the resonance frequency is plotted in absolute form against the detection power at 820nm in figure 4.5 for these two devices. The signal for the second device has been normalised at 100KHz to that for the first. In each case the signal is measured to an accuracy of ±1dB on the spectrum analyser. For the device vibrating at 97KHz the power of the 633nm laser was 240µW ±10µW throughout, for the device vibrating at 137KHz the power of the 633nm laser was 200µW ±10µW throughout. The spectrum analyser noise floor was -95dBm ±5dBm. The maximum signal-to-noise ratios measured for the two devices were 32dB and 23dB. The linear best fit curve for the combined data is also shown. It can be seen that signal amplitude rises linearly with detection power up to 200µW with a correlation coefficient of 0.99.

With the power at 820nm steady at 240μW ±10μW and 205μW ±10μW for the two devices respectively, the signal at the resonance frequency is plotted in absolute form against the activation power at 633nm in figure 4.6. The signal for the second device has been normalised at 100KHz to that for the first. The linear best fit curve for the combined data is also shown.

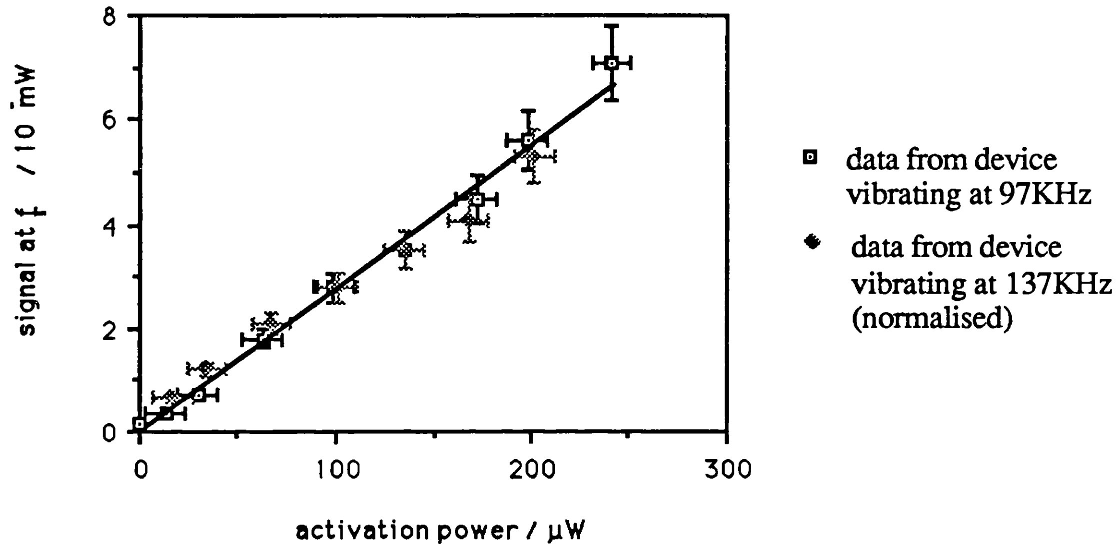

Figure 4.6: Amplitude of received signal at resonance plotted against incident power of intensity modulated drive.

It can be seen that signal amplitude rises linearly with activation power up to 240μW with a correlation coefficient of 0.99. The gradient of the curve shown in figure 4.6 is 2.9×10^{-3} W electrical / W optical for the device vibrating at 97KHz, and 1.2×10^{-3} W electrical / W optical.

4:3.2 Silicon Dioxide Microresonators: Mode Relationships

It was suggested in Chapter 3, Section 3:4.2 that the microresonators fabricated for this project may exhibit two sets of resonance frequencies related according to equation 3.2, with a non-standard end-condition parameter accounting for the webbed ends described in Chapter 2, Section 2:5. In order to test this hypothesis, the vibrational characteristics of four batches of metal-coated silicon dioxide beams, fabricated using the methods described in Chapter 2, were experimentally examined using the all-fibre system described in Section 4:2.1 above. Resonance peaks from metal-coated SiO_2 microbeams of around 30dB with quality factors around 30 were observed in the frequency spectrum of the return signal. Usually more than one mode could be excited.

The relative amplitudes of these peaks are dependent on the position of the area of incidence of the light on the beams. The relationship between position of optical activation and excitation efficiency has been examined for relatively large silicon resonators by Andres *et al.* [4]. In their case, because of the size of the resonators it was possible to use two separate fibres for activation and interrogation. This could not be done in the current experiments because of the small size of the beams considered here which have lengths comparable with the monomode fibre cladding diameter. It was therefore necessary to take a series of measurements on each device to enable all the principle modes of resonance to be observed. Preliminary investigations showed that, providing a suitable response was obtained, the position on the beam at which excitation was applied was unimportant. The observed frequencies corresponding to each particular mode from these results agreed to within $\pm 3\%$, which is within the resolution bandwidth used.

The metal-coated silicon dioxide beams in the four batches examined are described in Table 4.1, with batch standard deviation as specified in Chapter 2. Beams in the first two batches were simple beams, and those in the third and forth batches were paddle beams (illustrated in Chapter 2, Section 2:4.1, figure 2.6). The paddle beams were designed to have a wider central area to increase the intensity of the light absorbed from the activating beam and reflected from the detecting beam.

Batch 1: Simple beams of thermally grown SiO_2 (four beams):
Length 185µm; Width 5.5µm; Thickness 0.5µm
Coated with evaporated Al of thickness 200nm

Batch 2: Simple beams of thermally grown SiO_2 (six beams):
Length 230µm; Width 5.0µm; Thickness 0.5µm
Coated with evaporation coated with Al of thickness 200nm

Batch 3: Paddle beams of thermally grown SiO_2 (six beams):
Stem Length 230µm; Stem Width 5.0µm; Thickness 0.5µm
Paddle Length 40µm; Paddle Width 14µm
Coated with evaporated Al of thickness 200nm

Batch 4: Paddle beams of thermally grown SiO_2 (nine beams):
Stem Length 185µm; Stem Width 5.0µm; Thickness 0.5µm
Paddle Length 35µm; Paddle Width 12µm
Coated with sputtered Au of thickness 200nm

Table 4.1: Description of metal-coated silicon dioxide beams.

Up to six resonance frequencies were found for each beam using the frequency sweep method described above, using the 820nm laser for detection, and the mean batch values and standard deviations across the batch are tabulated in table 4.2.

Batch 1:

	f1	f2	f3	f4	f5	f6
Mean (KHz)	246	376	721	802	1430	1612
S.D. (KHz)	17	21	18	30	20	-
Quality Factor	27	35	50	56	67	65

Batch 2:

	f1	f2	f3	f4	f5	f6
Mean (KHz)	158	227	485	593	1051	1220
S.D. (KHz)	8	21	22	23	6	
Quality Factor	18	24	40	36	47	-

Batch 3 (f2,f3,f4 measured for 3 devices):

	f1	f2	f3	f4
Mean (KHz)	96	158	278	359
S.D. (KHz)	16	18	18	-

Batch 4 (f2,f3,f4 measured for 4 devices):

	f1	f2	f3	f4
Mean (KHz)	128	195	439	491
S.D. (KHz)	20	20	26	15
Quality Factor	15	19	26	41

Table 4.2: Resonance frequencies of silicon dioxide beams.

The relationship between the resonance frequencies of different modes may be compared with the standard theory given in Chapter 3, Section 3:2 (eqn.{3.2}). Microresonators studied elsewhere are commonly assumed to have clamped ends [5,6.7]. However, the devices in these publications are all larger than those studied here, and are not expected to have the complex end conditions (webbed ends) described in Chapter 2, Section 2:5. We expect the unusual condition described in Chapter 3, Section 3:4.2 to apply - essentially a combination of frequencies activated with both clamped and pinned ends.

This hypothesis is tested by comparing the experimental data with the predicted behaviour of the resonators described by the standard equation used to calculate the resonance frequencies of simple beams (eqn.{3.2}):

$$f_i = \left[\frac{\phi_i^2 \pi}{4\sqrt{3}}\right]\left[\frac{a}{L^2}\right]\sqrt{\frac{E}{\rho}} \qquad \{3.2\}$$

Values for the end condition parameter ϕ_i are substituted and the natural frequencies of each batch of devices plotted on a logarithmic scale against the relevant logarithmic end condition parameter, since from eqn.{3.2} above,

$$\ln f_i = 2 \ln \phi_i + C \qquad \{4.1\}$$

where C is a constant depending on the beam geometry and material parameters.

To test the hypothesis set out in Chapter 3, Section 3:4.2, relating to the vibration of beams mounted on webbed ends, I used the above model with ϕ_i taking the values obtained from the equation

$$\phi_i = (1+i/2) \qquad \{i = 1,2,3 \text{ etc.}\} \qquad \{4.2\}$$

Eqn.{3.2} indicates that the gradient of a logarithmic plot of resonance frequency against the end condition parameter is expected to have a gradient of two. The experimental results support this prediction. The gradients of these plots and the standard errors of the data from a linear fit for batch 1, batch 2, batch 3, and batch 4, are given in table 4.3.

Batch	gradient	standard error of data
1	1.99	0.062
2	2.23	0.060
3	1.98	0.033
4	2.12	0.080

Table 4.3: Logarithmic regressions of resonance frequencies of beams against webbed end condition parameters.

It is expected that the two separate sets of modes will have slightly different geometrical constants, reflecting the two non-standard mounting conditions described in Chapter 3, Section 3:4.2. This will give rise to a different constant C in eqn.{4.1} for the two mode sets. The even mode logarithmic frequencies will therefore be shifted with respect to the odd mode logarithmic frequencies by a constant amount

$$\Delta C = C_{odd} - C_{even} \qquad \{4.3\}$$

ΔC was calculated for each batch to minimise the standard error of the data. and the data replotted. The modified gradients and standard errors as well as the value of ΔC for batch 1, batch 2, batch 3, and batch 4, are given in table 4.4.

Batch	ΔC	gradient	standard error of data
1	0.21	2.1	0.017
2	0.23	2.23	0.060
3	0.10	2.06	0.008
4	0.27	2.35	0.010

Table 4.4: Logarithmic regressions of resonance frequencies of beams against webbed end condition parameters with arithmetic bias on even modes.

ΔC may be expressed as an effective length difference ΔL where, from eqn.{3.2}:

$$\ln(L + 2\Delta L) - \ln(L) = \Delta C \qquad \{4.4\}$$

The mean effective length difference across the four batches is 24μm, which is comparable with measured lengths of the oxide webbing (described in Chapter 2, Section 2:5).

These results give support to the validity of the standard beam theory, even in the more complex conditions encountered here.

Confirmation that the special conditions hypothesised for vibration of the beams supported on webbed ends is appropriate is obtained by comparing the experimental results with prediction from standard end conditions. If it is assumed that the beams are clamped at both ends, then we can put $\phi_i = (i+1/2)$. In this case, statistical regression gives the results given in table 4.5. It can be seen that the gradient obtained differs markedly from that predicted from standard beam theory. Further, the higher standard errors indicate that important factors have been omitted from the analysis.

Batch	gradient	standard error of data
1	1.34	0.111
2	1.20	0.166
3	1.25	0.068
4	1.34	0.140

Table 4.5: Logarithmic regressions of resonance frequencies of beams against clamped end condition parameters.

If it is assumed that the beams are pinned at each end, then we can put $\phi_i = i$. In this case, statistical regression gives the results given in table 4.6.

Batch	gradient	standard error of data
1	1.08	0.158
2	1.48	0.115
3	0.97	0.102
4	1.044	0.187

Table 4.6: Logarithmic regressions of resonance frequencies of beams against pinned end condition parameters.

These results also differ markedly from the standard beam theory. The failure of both simple assumptions to provide results consistent with the standard beam theory gives indirect support to the hypothesis associated with the webbed end condition.

Typical examples of logarithmic plots of resonance frequencies against end condition parameters are shown in figure 4.7, figure 4.8 and 4.9. Figure 4.7 shows the results from the batch 1 devices plotted using the webbed end condition parameter as described above, with the alternate modes not corrected for the different geometrical constants. Figure 4.8 shows the same data plotted with a bias on the even modes corresponding to a value of $\Delta C = 0.21$. Finally figure 4.9 shows the data plotted using the clamped end condition parameter as described above. The form of the plots is similar for all foutr batches of devices.

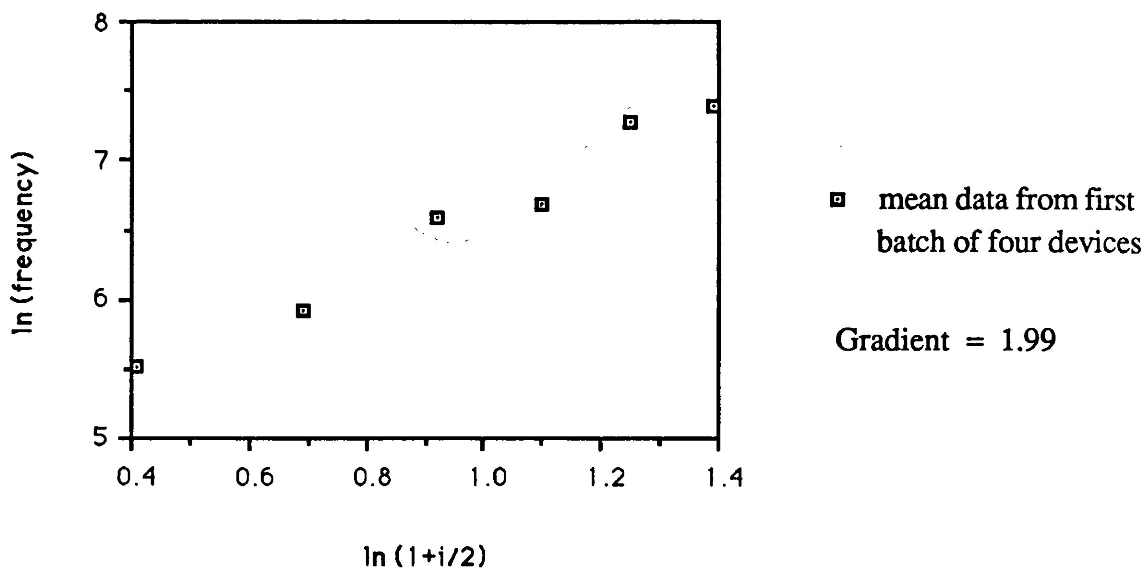

Figure 4.7: R /Al simple 185μm beams: Logarithmic plot against mode number (1+i/2).

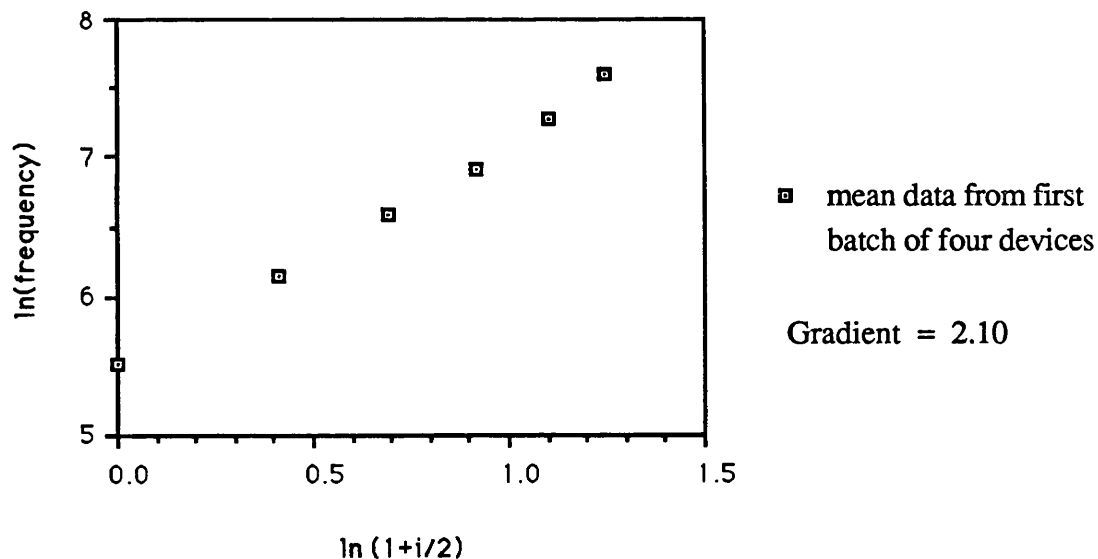

Figure 4.8: R /Al simple 185μm beams: Logarithmic plot against mode number (1 + i/2), with an arithmetic bias on even modes of 0.21.

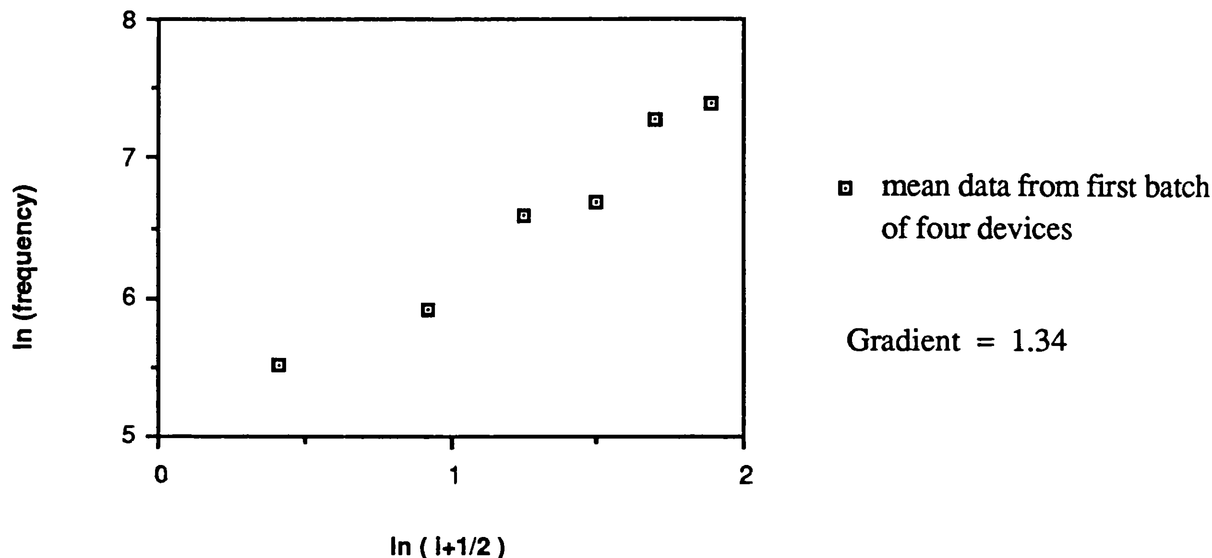

Figure 4.9: Resonance frequencies of SiO_2/Al simple 185μm beams: Logarithmic plot against mode number (i+1/2).

It should also be noted that resonance frequencies of any torsional modes would be proportional to their mode numbers, as can be seen from eqn.{3.7}, Section 3:2.2, and do not fit the experimental results. The resonance frequencies of any flexural modes in the plane of the wafer would differ from the corresponding frequencies of transverse flexural vibrations by a factor of b/a, as can be seen from eqn.{3.2}, Section 3:2.1.1. For the beams considered here, $b/a \geq 10$. It can thus be safely assumed that torsional and flexural vibrations have not interfered with the oscillations measured.

We also examine the mode relationships of a number of metal-coated silicon devices in Section 4:3.7 of this chapter.

4:3.3 Variation of Resonance Frequency with Beam Length

We are also able to test the standard theory expressed by eqn.{3.2} by comparing the resonance frequencies of metal-coated silicon dioxide beams of different lengths.

I fabricated several shorter (90μm) beams of thermally grown SiO_2, evaporation coated with aluminium. The predicted resonance frequencies of these devices are much higher than those of the previous batches since from eqn.{3.3}

$$f_i \;\alpha\; \frac{\phi_i^2}{L^2} \qquad \{4.4\}$$

I was unable to detect resonance vibrations in simple beams of this length. However a resonance was found for three triple paddle beams (batch 5), which have lower predicted resonance frequencies than the simple beams, as can be seen from the description Chapter 3, Section 3:2.1.2, and eqn.{3.3}. The dimensions are as follows:

Stem Length 90μm; Stem Width 5.0μm; Thickness 0.5μm
Central Paddle Length 11μm Central Paddle Width 18μm
Side Paddles Length 5μm Side Paddles Width 18μm
Aluminium Thickness 200nm

The resonance frequency found is given in table 4.7.

Batch of 3 devices	f / KHz
Mean	664
S.D.	30
Quality Factor	39

Table 4.7: Resonance frequencies of SiO_2/Al triple paddle 90μm beams (batch 5).

The equivalent resonance frequency for a similar beam without paddles may be extrapolated using eqn.{3.5}. In this case the measured resonance frequency f_1* is equal to 664 KHz and $M/M_b = 0.61$, whence the corrected resonance frequency (as given in eqn.{3.3}) f_i, is equal to 1080 KHz. This data can be used in conjunction with that from the devices characterised in table 4.1 to examine the dependence of the first detected resonance frequency on beam length for simple beams. The fit to eqn.{3.2} is examined by a linear regression of f_1 to L^{-2} through the origin, plotted in figure 4.10. The standard error of estimation is 6KHz. This is a good support for the relationship predicted by theory.

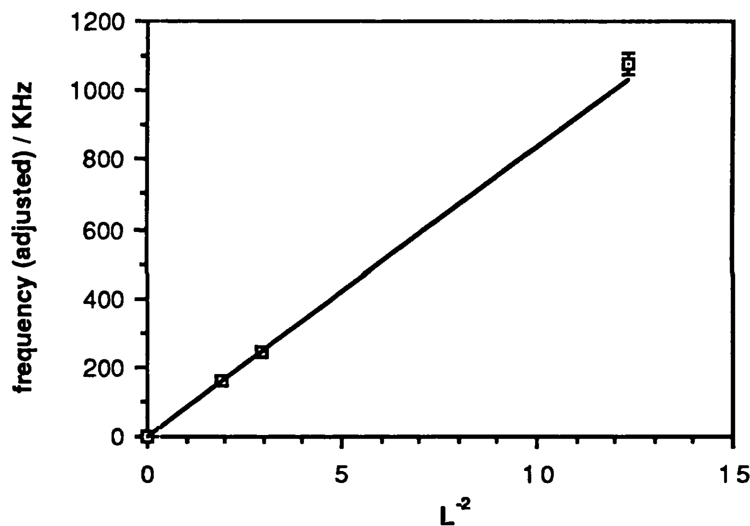

Figure 4.10: Resonance frequencies of SiO_2/Al simple beams: Linear plot against L^{-2}.

The resonance frequencies of paddle beams of different lengths may also be compared using data from table 4.1. The fit to eqn.{3.2} is again examined by a linear regression of f_1 to L^{-2} through the origin (two points only, not shown). The standard error of estimation is 5KHz, again providing good support for the predicted relationship.

Finally, the fit to eqn.{3.2} for simple beams of thermally grown SiO_2, evaporation coated with aluminium may be compared for different modes. The results are tabulated in table 4.8. The standard error is expected to be higher for higher modes since errors due to non-linearities become more pronounced there [8].

Mode	gradient / μHzm^2	standard error / KHz
1	84	1.0
2	128	13
3	248	15
4	279	59

Table 4.8: Gradient and standard error of estimation for best fits to eqn{3.2} for simple beams.

4:3.4 Variation of Resonance Frequency with Metal Thickness

Consideration of the standard equation, not corrected for fabrication-induced stress, for the resonance frequencies of simple beams (eqn.{3.2}, Chapter 3, Section 3:2.1.1) and of the correction necessary in the analysis of composite beams (eqn.{3.6}, Chapter 3, Section 3:2.1.4), indicates that the resonance frequencies of composite beams are expected to increase with increasing thickness of the metal coating layer. However, we suggested in Chapter 3, Section 3:4.1, that in the case of metal-coated silicon dioxide microbeams the metal thickness will effect the mean fabrication-induced beam stress, so that increasing the metal thickness will reduce the mean beam stress. If this effect dominates, the resonance frequencies will be expected to decrease with increasing thickness of the metal coating layer.

This hypothesis was tested by comparing the resonance frequencies of a number of

identical silicon dioxide beams coated with different thicknesses of metal.

I fabricated a further batch of silicon dioxide paddle beams with the following dimensions:

Stem Length 185μm; Stem Width 5.5μm; Thickness 0.5μm
Paddle Length 35μm; Paddle Width 12μm

Five devices are sputter-coated with 41nm of gold and the first resonance frequency of each found using the system described in Section 4:2.2 of this chapter. A further layer of gold is then sputtered onto the same wafers and the devices interrogated again. This process is continued up to a gold thickness of 340nm. The results are tabulated in table 4.9. This data is collated/extrapolated from reference [9], which describes work carried out for this project.

The data is plotted in figure 4.11 which shows a decrease in resonance frequency with increasing gold thickness.

For the devices in this same batch the experiment was repeated with evaporated aluminium in place of gold. In this case the metal was completely removed using an acid etch between each set of measurements. The resonance frequencies measured are tabulated in table 4.10 below. This data is extrapolated from [9], and plotted in the form of resonance frequency against aluminium thickness in figure 4.12.

The resonance frequency of the beams is observed to decrease with increasing metal thickness over the range examined. This result contradicts the standard theory before the effects of beam stress are included in the analysis. However it supports the analysis of beam stress given in Chapter 3, Section 3:4.1, and indicates that the effect of decreasing the beam stress by increasing the metal thickness (eqn.{3.57}) dominates that of increasing the second moment of area (eqn.{3.1}).

Batch of 5 devices

Au thickness / nm:	41	97	113	135	180	220	340
Mean / KHz	114	108	103	103	97	89	8
S.D. / KHz	25	25	24	24	23	23	21
Quality Factor	18	20	20	19	18	17	15

Table 4.9: First resonance frequencies of SiO_2 beams / KHz.
Data extrapolated from [9]

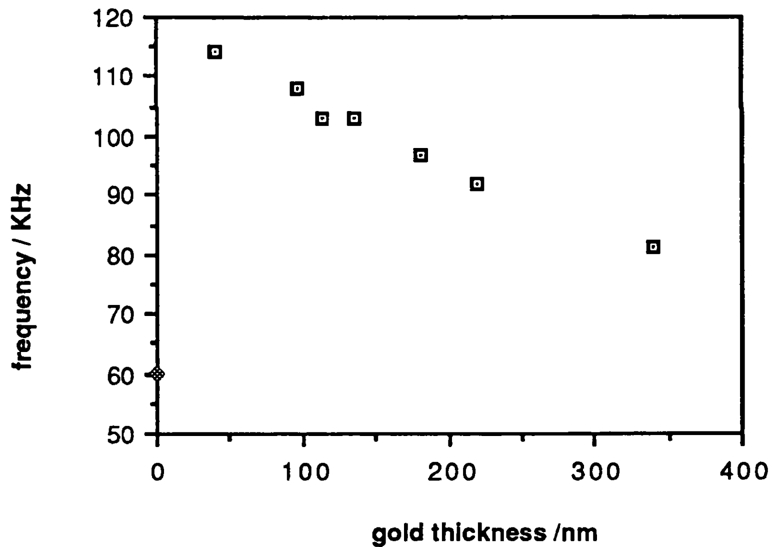

Figure 4.11: Resonance frequencies of gold coated SiO_2 beams: Linear plot against gold thickness.

Batch of 5 devices			
Al thickness / nm:	65	165	350
Mean / KHz	139	134	91
S.D./ KHz	4	44	17
Quality Factor	21	16	13

Table 4.10: First resonance frequencies of SiO_2 beams / KHz.
Data collated and extrapolated from [9]

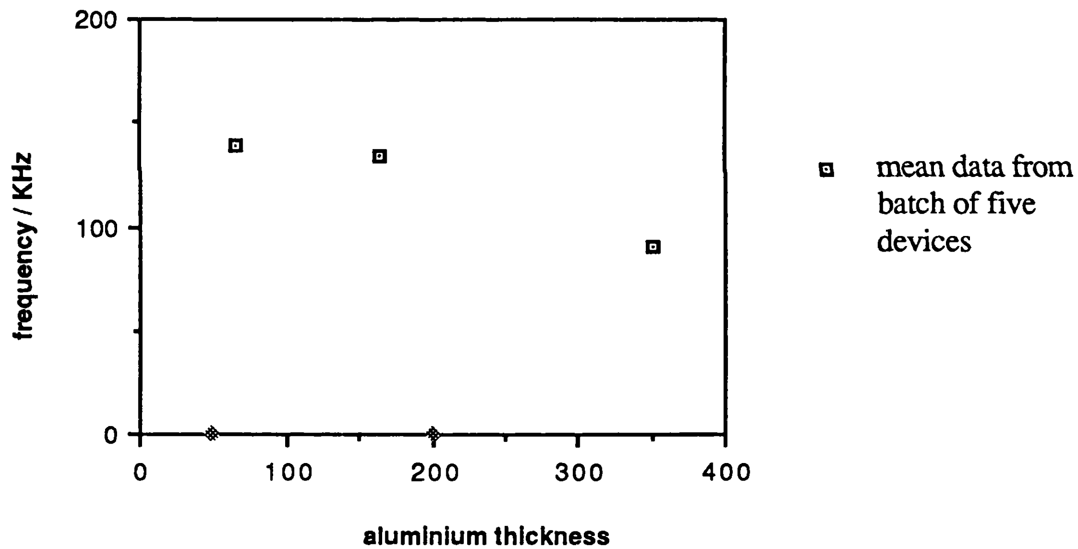

Figure 4.12: Resonance frequencies of Al Coated SiO_2 beams: Linear plot against aluminium thickness.

4:3.5 Silicon Microresonators: Mode Relationships

A brief programme of experimental work was carried out to look for evidence of the mode relationships described for metal-coated silicon dioxide microresonators in Section 4:3.2 of this chapter in metal-coated silicon microresonators.

We designed several varieties of resonator beams and incorporated these on a single photolithographic mask. The fabrication was carried out by the Southampton University Dept. of Materials Science where the necessary ion implantation ovens were available. These devices were all fabricated using Boron as an etch-stop, as described in Chapter 2, Section 2:2.2.

We experimentally examined the vibrational characteristics of several devices using the system shown in Section 4:2.1 of this chapter. For three of these devices we were able to measure more than one resonance frequency. The dimensions and resonance frequencies of these beams are tabulated in table 4.11 and table 4.12. The first is a paddle shaped beam, as shown in Chapter 2, Section 2:4.1, figure 2.6, the second non-symmetrically paddle shaped beam and the third a non-symmetrically winged beam. The designs of the non-symmetrical beams are shown in figure 4.13.

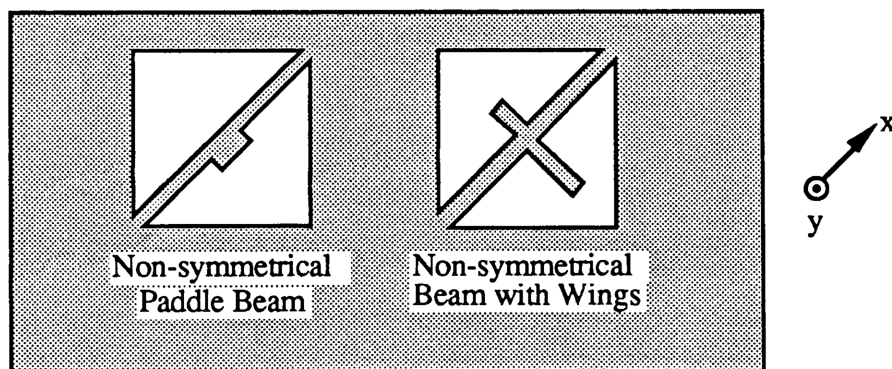

Figure 4: 13: Plan views of non-symmetrical beams.

The relationship between the resonance frequencies of different modes may be compared with that predicted using eqn.{3.11}, in the same way as for SiO_2 beams. The results of similar analyses to those carried out above are tabulated in table 4.13 , table 4.14, table 4.15 and table 4.16 below. A description of the form of this analysis and a definition of the constant C, which depends on the beam geometry and material parameters, is given in Section 4:3.2 of this chapter.

It is apparent from this analysis that those silicon devices examined exhibit broadly similar behaviour to the silicon dioxide devices considered above, although fewer devices have been examined. Where several resonances are observed, two separate sets of modes can be distinguished and the best fit is obtained to the beam theory when the new end-condition parameter is used in the model. This supports the hypothesis that the behaviour is caused by the non-standard end conditions, since the silicon devices examined in Chapter 2, Section 2:4.2, were observed to have webbed ends.

Paddled beam of silicon (#1):

Stem Length 185μm;	Stem Width 2.0μm;	Thickness 0.5μm
Paddle Length 25μm	Paddle Width 10μm	

Sputter coated with Au of thickness 200nm

Non-symmetrically paddled beam of silicon (#2):

Stem Length 185μm;	Stem Width 2.0μm;	Thickness 0.5μm
Paddle Length 31μm	Paddle Width 12μm	

Sputter coated with Au of thickness 65nm

Non-symmetrically winged beam of silicon (#3):

Stem Length 170μm;	Stem Width 2.0μm;	Thickness 0.5μm
Paddle Length (48μm+10μm)	Paddle Width 2.0μm	

Coated with evaporated Al of thickness 200nm

Table 4.11 Description of metal-coated silicon beams.

Paddled beam of silicon (#1):

	f1 / KHz	f2 / KHz	f3 / KHz	f4 / KHz	f5 / KHz
	84	227	350	492	703
Q:	42	76	100	89	180

Non-symmetrically paddled beam of silicon (#2):

	f1 / KHz	f2 / KHz	f3 / KHz	f4 / KHz
	111	269	348	574
Q:	75	75	75	125

Non-symmetrically winged beam of silicon (#3):

	f1 / KHz	f2 / KHz	f3 / KHz	f4 / KHz	f5 / KHz	f6 / KHz	f7 / KHz
	159	282	465	604	702	1174	1655
Q:	12	34	35	40	44	54	65

Table 4.12: Resonance frequencies of silicon beams.

Beam	gradient	standard error of data
#1	2.44	0.055
#2	2.27	0.064
#3	2.40	0.036

Table 4.13: Logarithmic regressions of resonance frequencies of silicon beams against webbed end condition parameters.

Beam	ΔC	gradient	standard error of data
#1	-0.11	2.43	0.048
#2	-0.21	2.09	0.029
#3	0.05	2.42	0.034

Table 4.14: Logarithmic regressions of resonance frequencies of silicon beams against webbed end condition parameters with arithmetic bias on even modes.

Beam	gradient	standard error of data
#1	0.62	0.048
#2	1.45	0.078
#3	1.35	0.090

Table 4.15: Logarithmic regressions of resonance frequencies of beams against clamped end condition parameters.

Beam	gradient	standard error of data
#1	1.29	0.044
#2	1.13	0.097
#3	1.05	0.142

Table 4.16: Logarithmic regressions of resonance frequencies of beams against pinned end condition parameters.

4:3.6 Consideration of Quality Factors

The experimentally measured values for Q may be compared with those calculated from eqn.{3.36}, which was derived in Chapter 3, Section 3:3.1.4 and is reproduced below.

$$Q \approx 0.4 \frac{a b^2}{L^2} \frac{\sqrt{E \rho}}{\eta_{air}} \qquad \{3.36\}$$

Materials data used in this calculation are included in Appendix A. Data for geometrical measurements and experimentally measured quality factors are obtained from table 4.2, batch #1 and batch #2 (Section 4:3.2 of this chapter). The devices considered here are all simple beams evaporation coated with aluminium. In addition, the aluminium coated silicon winged beam characterised in table 4.11 and table 4.12 (Section 4:3.5) is considered. The data is summarised in table 4:17.

Device	Q (calc.)	Q (meas.)
SiO_2, 185μm long	120	27
SiO_2, 230μm long	65	18
Si (winged, see above)	18	12

Table 4.17: Quality factors calculated and measured experimentally.

It appears that the quality factor is limited beyond that which is expected from a consideration of viscous damping alone. Data from table 4.2 and table 4.12 are used to plot the variation of Q with frequency. This is shown in figure 4.14 below.

The variation of Q with metal thickness (extrapolated from [9]), both for sputtered gold and evaporated aluminium, is shown in figure 4.15.

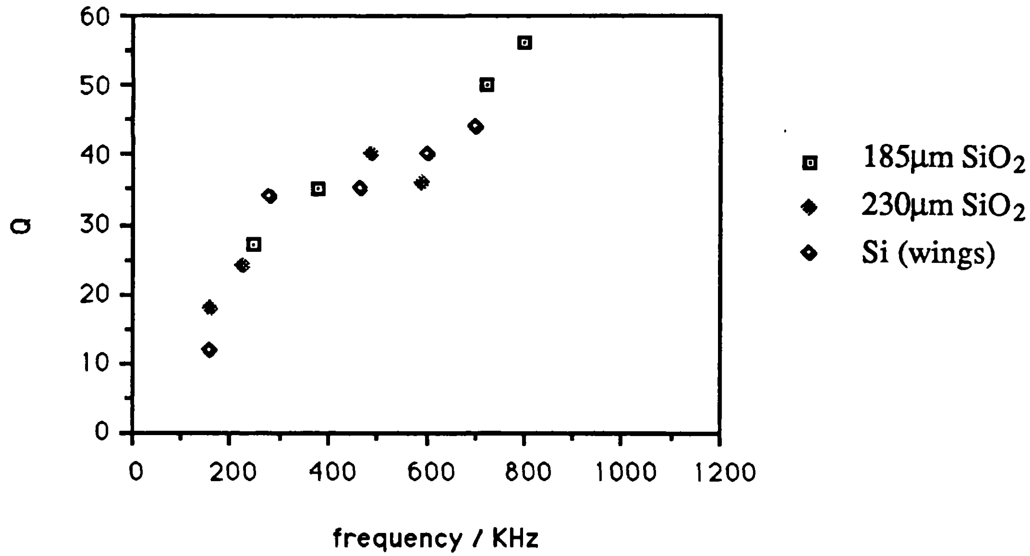

Figure 4.14: The variation of quality factor with frequency.

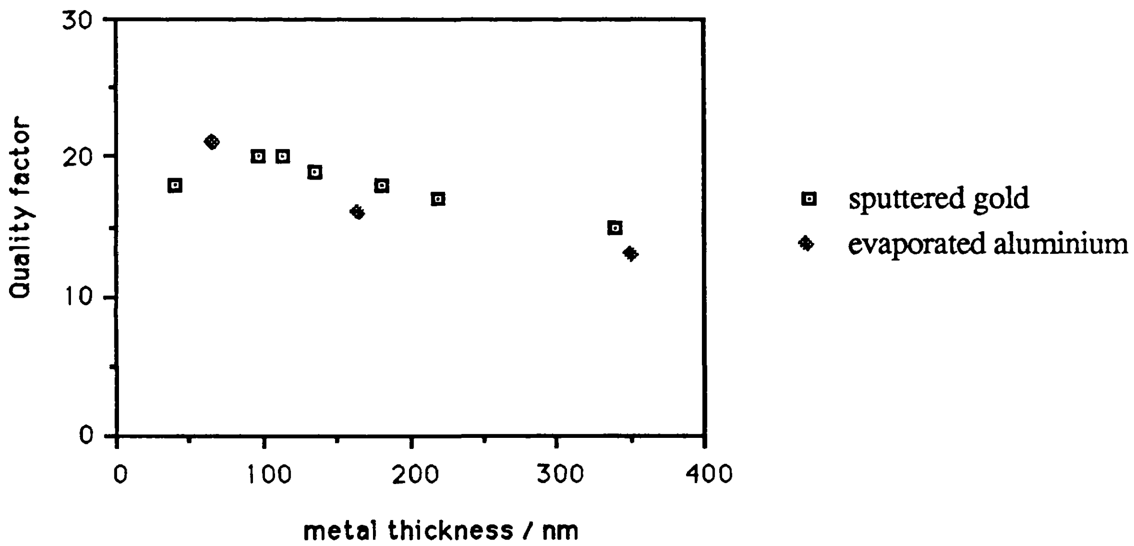

Figure 4.15: The variation of quality factor with metal thickness.

4:4 Electrical Drive

4:4.1 Capacitive Drive

Optical detection of electrically activated microresonators has been demonstrated previously [10,11]. In these cases, cantilevers were used and the vibrations detected using a bulk optical system. The electrical activation was achieved through electrostatic attraction by applying an oscillating voltage between the metallised surface and a buried p^+ layer in the silicon substrate. Experimental work has also been reported on the capacitive drive - and readout - of polysilicon microbridges [12], on the electrostatic drive of silicon structures [13,14] and on the electrostatic comb drive of polysilicon structures [15,16].

Experiments were conducted to attempt to drive beams such as those described above electrically, with the all-fibre system described used for detection of vibrations. The beams used in the work referenced involve features designed to enable electrical drive. The beams used here are more simple devices with no additional processing undertaken for these experiments.

The detection of vibrations is carried out optically using the all-fibre system described in section 3:4.1, with a single GaAs 1.5mW laser emitting at 820nm and a single fused fibre coupler. The fibre is single-moded at 820nm and the coupler has a split ratio of 50% at 820nm and an insertion loss at this wavelength of less than 0.2dB.

The activation of vibrations is achieved by applying an oscillating potential difference between the opposite faces of the silicon wafer piece on which the microresonator beam has been fabricated. The back face of the wafer piece is attached to a metal mounting-stub with a thin even layer of silver-loaded conductive paint. Using the same adhesive a thin copper wire is attached near the edge of this face and a second wire is attached near the opposite edge of the front face (figure 4.15). These are connected across the output of a function generator (hp3325A). In the same way as for optically activated vibrations, the resonance frequencies of the microresonators may be identified by sweeping the modulation frequency of the function generator output and observing the position of the maximum intensity modulation imposed on the return optical beam.

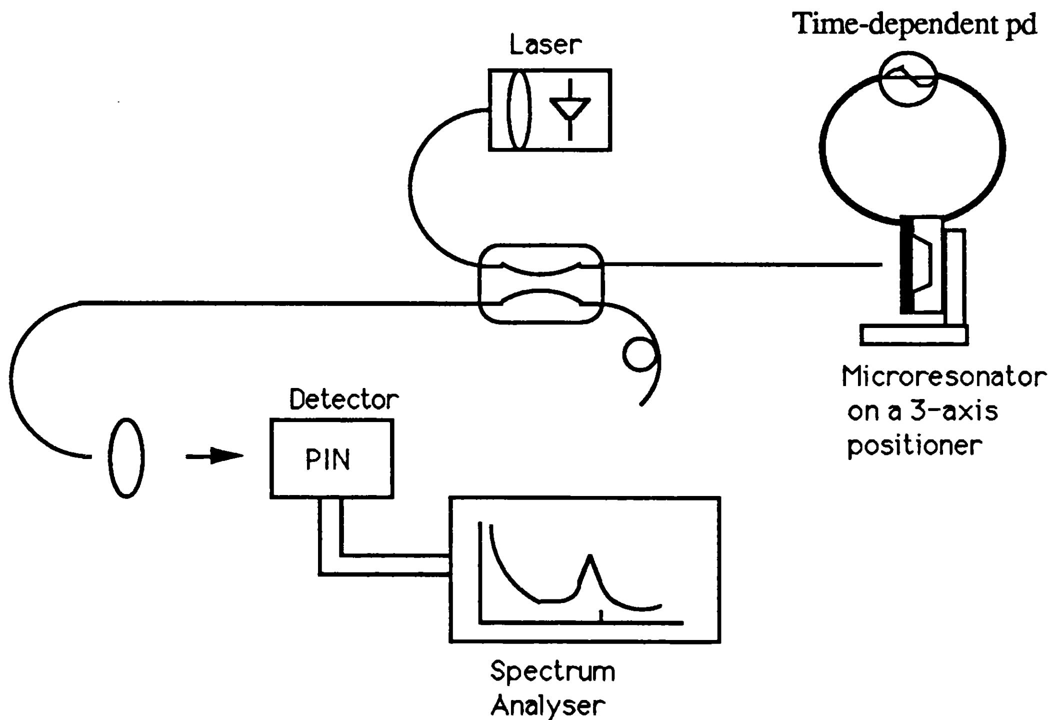

Figure 4.15 Schematic of fibre-optic system for addressing of electrically activated microresonator vibrations.

Vibrations are driven by means of the electrostatic force between the front and back surfaces of the silicon wafer. This force displaces the beam towards the back face. By applying a varying potential difference across the wafer the beam may be sustained in vibration. Since the electrostatic force is always attractive, a natural resonance frequency of the beam may be excited by applying a signal at half this frequency.

We have demonstrated the capacitive drive of aluminium coated silicon dioxide microresonator paddle beams. These beams I fabricated as described in Chapter 2, Section 2:4.1. Vibrations are excited at the resonance frequency with the drive at this frequency and at half this frequency. The peak-to-peak potential difference applied is typically 20V. At 2V peak-to-peak a signal of 5dB above noise is observed. The response to a signal at the resonance frequency is thought to be a result of a resistive drive mechanism, as described below.

4:4.2 Resistive Drive

Experimental work on the activation of silicon microresonator beams by direct electrothermal methods has been reported [17,18]. This work used resistors diffused into [17] or deposited onto [18] the beams. In our work we have demonstrated that it is possible to excite vibrations in simple metal-coated silicon beams such as those described for the optical excitation work, with no further processing steps required. In addition the detection of vibrations is carried out optically, using the all-fibre system described in Section 4:2.1 of this chapter. The activation of vibrations is achieved in the same way as for the capacitive drive described above, but in this case the copper wires are both attached on the front face of the wafer. Any resonance frequencies may be identified in the same way.

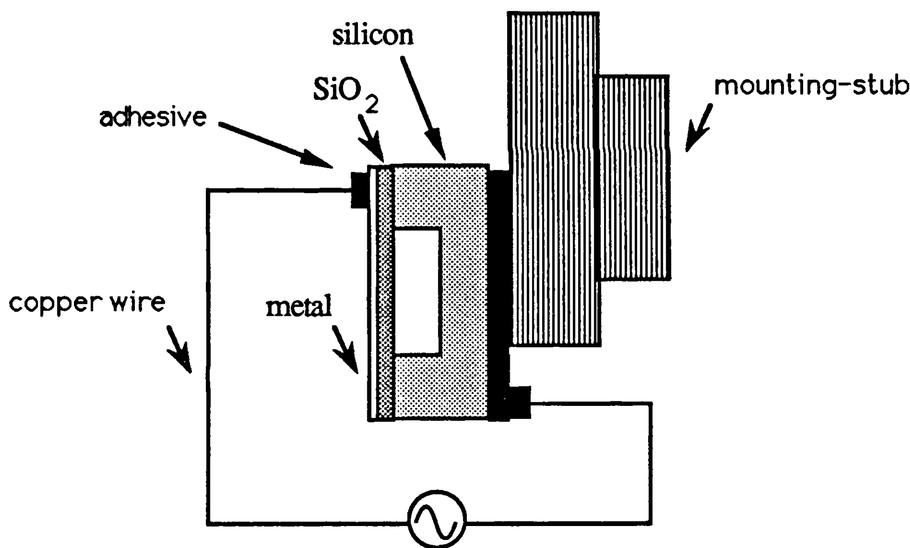

Figure 4.16: Schematic of the attachment of wires to a silicon wafer piece for activation of microresonator vibrations.

In this case vibrations are driven by means of the thermal expansion produced when the metal coating of the beam is heated by passing of an electric current. Because the heating produced from an electric current varies with the square of the current, the

drive signal must again be at half the resonance frequency of the beam. Alternatively if a bias voltage is applied, then there will be a component of the temperature variation at the same frequency as the drive.

We have demonstrated the resistive drive of simple chromium coated silicon microresonator beams, of similar geometry to those excited optically.

4:5 Conclusions

An all-fibre system for the activation and detection of microresonator vibrations has been developed. The photothermal activation of beams around 200μm long, 5μm wide and 0.5μm thick has been demonstrated, first with beams of thermally grown silicon dioxide either evaporation coated with aluminium or sputter coated with gold, then with beams of metal-coated silicon. The behaviour of some of these beams has been compared with the beam theory described in Chapter 3. In the case of beams of metal coated thermally-grown silicon dioxide, two separate sets of resonances have been identified for all the beams examined. An alternative end-condition parameter is proposed which models this behaviour to a better fit than the standard conditions. This is observation is thought to be a result of the webbed end condition described in Chapter 2, which is significant in devices of these dimensions. The silicon beams examined also exhibit this behaviour.

Variation of resonance frequency with beam length and width were also examined, and these relationships fit the beam theory described in Chapter 3. The variation of frequency with metal thickness on a thermally-grown silicon dioxide beam is also examined and accounted for, considering the fabrication-induced stresses in the resonator. The quality factors were considered and found to depend on frequency, and on metal thickness. Further work is required to optimise the quality factor for a prototype device. Finally silicon dioxide and silicon devices such as those described above have been driven electrically.

We may conclude that there is a range of materials available from the manufacturing technologies developed for the microelectronics industry from which beams may be

fabricated which can be driven into resonance vibrations optothermally using an all-fibre system. However extreme care must be exercised in the fabrication since the behaviour of the beams of dimensions small enough to be driven using very low levels of optical power, and to be compatible with the dimensions of an optical fibre, is clearly critically dependent on their geometrical properties.

It is clearly unrealistic to expect the integrity of in-house fabrication to match that of commercial batch-production. Effort was therefore focussed next on considering some sensing possibilities of the microresonators, and then on developing a new optical scheme and activation method which might allow sensors to be multiplexed.

References for Chapter 4

1. S.Venkatesh *et al.*; "*Fibreoptic Detection Of Optothermal Vibrations*"; Technical Digest of OFS '86, Tokyo, PD-2 - PD-5, 1986
2. S.Venkatesh *et al.*; "*Optically Activated Resonator Sensors*"; Proc. SPIE Conference on Fibre Optic and Laser Sensors III, San Diego, pp110-113, 1985
3. S.P.Timoshenko *et al.*; "Vibration problems in Engineering"; John Wiley and Sons, 1974
4. M.V.Andres *et al.*; "Optical Activation of a Silicon Vibrating Sensor"; Elec. Lett., Vol.22(21), pp1097-1099, 1986
5. K.T.V.Grattan *et al.*; "Optically Powered Sensors Based on Resonant Structures: Mathematical Analysis"; SPIE Vol.949, Fibre Optics 1988, pp152-161

6. K.E.B. Thornton *et al.*; "*Temperature Dependance Of Resonance Frequency In Optically Excited Diaphragms*"; Electronics Lett., Vol.22, pp 1232-1234, 1987
7. R.T.Howe & R.S.Muller; "*Resonant Polysilicon Micromechanical Beams*"; J.Electrochem.Soc., vol.130, pp1420-1423, 1983
8. Blevins; "Formulas for Natural Frequency and Mode Shape"; Van Nostrand Reinhold Company, New York, 1979
9. P.Zouganeli; "Materials for Metal Coaing of a Fibre Optic Microresonator Pressure Sensor"; M.Sc.Thesis, Dept. Elec. Eng., University College, London, 1988 (unpublished)
10. K.E.Petersen; "*Young's modulus measurements of thin films using micromechanics*"; J. Appl Phys, Vol 50, 1970, pp 6761-6766.
11. Petersen, K E: "*Silicon as a mechanical material*"; Proc. IEEE, Vol 70, No 5, 1982, pp 420-457.
12. R.T.Howe & R.S.Muller; "*Polycrystalline Silicon Micromechanical Beams*"; J.Electrochem.Soc. 130, p 1420, 1983
13. J.C.Greenwood; "*Etched Silicon Vibrating Sensor*"; J.Phys.E.: Sci.Instrum., Vol.17, pp650-652, 1984
14. J.C. Greenwood; "*Resonant Silicon Sensors at STL* ; Abstracts of Eurosensors, 3rd Conf. on Sensors and their Applications, Cambridge, 1987, pp14-15
15. W.C.Tang *et al.*; "*Laterally Driven Polysilicon Resonant Microstructures*"; IEEE Micro Electromechanical Systems Workshop, Salt Lake City, Utah, 1989, pp53-59
16. W.C.Tang *et al.*; "*Electrostatic-Comb Drive of Lateral Polysilicon Resonators*"; Abstracts of 5th International Conference on Solid State Sensors and Actuators (Transducers '89), Montreux 1989, pp138-140
17. M.B.Othman & A.Brunnschweiller; "*Electrothermally Excited Silicon Beam Mechanical Resonators*"; Electronics Lett., Vol.23, pp728-730, 1987
18. R.J.Wilfinger *et al.*; "*The Resonistor: A Frequency Selective Device Utilizing the Mechanical Resonance of a Silicon Substrate*"; IBM Res.&Dev., vol.12, pp113-118, 1968

CHAPTER 5: PRESSURE AND TEMPERATURE SENSITIVITIES OF MICRORESONATORS

5:1 Introduction

5:2 Analysis

- 5:2.1 Effect of Applied Pressure
- 5:2.2 Effect of Change in Temperature

5:3 Experimental Method

5:4 Experimental Results

- 5:4.1 Effect of Applied Pressure
  - 5:4.1.1 Silicon resonators
  - 5:4.1.2 Silicon dioxide resonators
- 5:4.2 Effect of Change in Temperature
  - 5:4.2.1 Silicon resonators
  - 5:4.2.2 Silicon dioxide resonators

5:5 Discussion

- 5:5.1 Effect of Applied Pressure
- 5:5.2 Effect of Change in Temperature

5:6 Conclusions

References for Chapter 5

CHAPTER 5

PRESSURE AND TEMPERATURE SENSITIVITIES OF MICRORESONATORS

5:1 Introduction

Fibre-optic microresonators such as those examined as described in the previous chapter have a wide range of potential applications as sensors. The experimental programme described in this chapter was undertaken in order to determine their suitability for development in these roles.

We have considered both the effect of a differential pressure applied across the silicon wafer on which the microresonator beam is fabricated, and of a change in device temperature, on the resonance frequencies of these devices. The vibration frequencies of the microresonators are dependent not only upon the dimensions of the structure and the material properties, mass and end-conditions of the beams, but also upon any forces that may be acting on the structure. Both temperature and differential pressure will cause a change in beam stress and thus in the resonance frequency. They may therefore be measured since they will induce changes in the resonance frequency.

It is also important to consider the effect of these environmental parameters when the sensors are used for other applications. In this way cross-sensitivity may be minimised or compensation schemes can be investigated.

First the pressure and temperature sensitivities of beams have been derived. Both silicon and silicon dioxide beams have been considered. In the case of metal-coated silicon beams it has been possible to do this from standard expressions used for macrostructures. Metal-coated silicon dioxide beams must be treated differently since, as has been pointed out in Chapter 2, Section 2:3, they are deflected by the fabrication process. As a result of this feature they are expected to be insensitive to applied pressure, and this is discussed later in this chapter. The temperature sensitivity of a metal-coated oxide beam, however, is derived from the expression for beam stress in

a deflected beam whuch we derived in Chapter 3.

Secondly both temperature and pressure dependence of the resonance frequencies of silicon and silicon dioxide microbeams have been demonstrated. The resonance frequency of an optically excited and interrogated silicon diaphragm has been previously shown experimentally to be temperature dependent [1]. We have carried out all the demonstrations using the monomode fibre-optic system for activation and interrogation of vibrations developed for the characterisation of the devices.

Finally measurements of temperature and pressure sensitivities are made and a comparison made between silicon and silicon dioxide microbeams. These measurements are also compared with the predictions made by the analysis.

It may be noted that at the same time as the experimental work on this project was carried out, work was undertaken at Strathclyde University which demonstrated the temperature and pressure dependence of a silicon microresonator structure using a bulk optical system for activation and detection of vibrations [2,3]. Although a model was suggested to relate resonance frequency of the structure to applied pressure, no theoretical analysis has been proposed to model the temperature dependence of the resonance frequency of microstructures.

5:2 Analysis

We wish to derive expressions for the pressure sensitivities and temperature sensitivities of silicon and silicon dioxide beams, in order to make predictions about the way in which these devices might behave, and to be able to compare experimental results from our devices with the predicted behaviour.

5:2.1 Effect of Applied Pressure

First we analyse the effect of applied pressure on the stress in, and hence on the resonance frequencies of, straight simple microresonator beams.

The pressure is assumed to be applied across a circular wafer on which the beam has been fabricated, clamped round its circumference. The thickness of the beam is assumed to be negligible compared with the wafer thickness. The clamped wafer is illustrated in figure 5.1. The resonator beam is shown a distance r from the centre of the wafer.

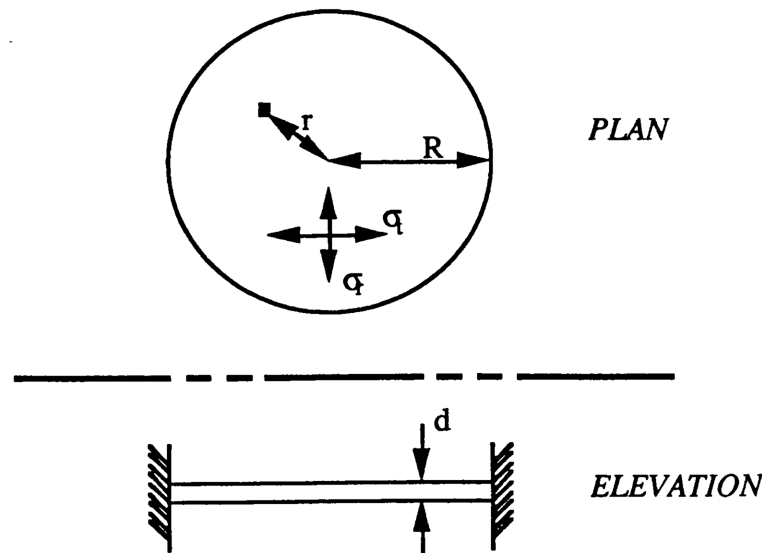

Figure 5.1: Schematic of circular wafer across which a differential pressure is applied.

A differential pressure ΔP applied across a circular wafer clamped at the circumference will cause a stress σ varying along the wafer radius. The radial and tangential components of this stress are [4]:

$$\sigma_{rad} = \frac{3\,\Delta P\,R^2}{8d^2}\left[(3+\nu)\frac{r^2}{R^2} - (1+\nu)\right] \qquad \{5.1\}$$

$$\sigma_{tan} = \frac{3\,\Delta P\,R^2}{8d^2}\left[(1+3\nu)\frac{r^2}{R^2} - (1+\nu)\right] \qquad \{5.2\}$$

where R is the radius of the wafer exposed to pressure, d is the wafer thickness and ν is Posson's ratio of the wafer material. Thus the orientation of the resonator beam on the wafer also effects the magnitude of the applied stress. It can be seen that across the wafer there are regions of compression, near the edges, and tension, near the centre.

As we have described in Chapter 3, Section 3:2.1.3, the stress induced in the resonator beam material will result in a change of resonance frequency. The magnitude of this change for a simple beam of rectangular cross-section is given in terms of the stress in eqn.{3.5} in Section 3:2.1.3. It can be seen that the change in frequency is proportional to the stress. It can also be seen that if the beam is in an area of tension, the frequencies will be raised; if the beam is in an area of compression the frequencies will be lowered. This is illustrated in figure 5.2, which shows the variation of frequency shift with position for a tangentially and for a radially oriented beam on a wafer subjected to a given differential pressure, calculated from eqn.{5.1} and eqn.{5.2}.

The effect of the etch pit under the beam is neglected since the size of the pit is relatively small. The stress at the centre of the wafer may then be derived from eqn.{5.1} to be

$$\sigma_c = \frac{3R^2}{8d^2}(1+\nu)\Delta P \qquad \{5.3\}$$

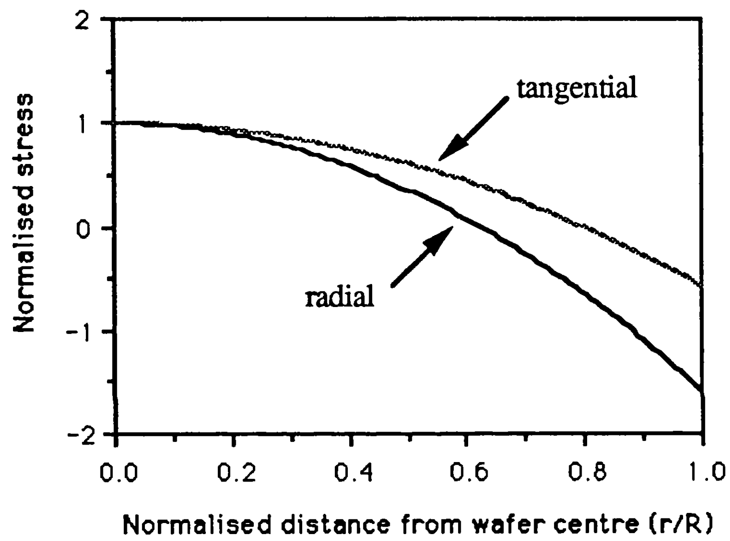

Figure 5.2: Dependence of frequency shift with a given applied pressure on beam position and orientation (for $\nu = 0.3$)

The stress in a thin layer of material of Young's modulus E_x different from that of the principle wafer material E_s, such as silicon dioxide on a silicon wafer, is expected to differ from the stress in the adjacent material by a factor of E_x/E_s so that the stress in this material at the centre of the wafer will be

$$\sigma_c = \frac{3R^2}{8d^2}(1+\nu)\Delta P \frac{E_x}{E_s} \qquad \{5.4\}$$

If the effect of the etch pit below the resonator beam is ignored, then this stress σ_T may be considered to be the stress in the beam. In this case the shift in resonance frequency, Δf, for a beam of rectangular cross-section subjected to this increase in stress σ_T, can then be calculated using eqn.{3.5}, from Section 3:2.1.3, as

$$\frac{\Delta f}{f_0} = c'(1+\nu)\frac{L^2}{a^2}\frac{R^2}{d^2}\frac{\Delta P}{E} \qquad \{5.5\}$$

where f_0 is the resonance frequency of the relaxed beam; c' is a constant with value 0.0551; E is the Young's modulus of the principle wafer material; and a is the total beam thickness.

This expression is expected to apply to silicon beams such as those examined in this project, and a programme of experimental work has been carried out to test this. The results of this work are described later in this chapter in Section 5:4.1.1.

This expression however is expected not to apply to silicon dioxide beams for the following reason. It has been discussed in Chapter 3, Section 3:4.1, that silicon dioxide beams are deflected as a result of the relief of fabrication-induced compressive stress even when no external pressure is applied. They are not therefore put under the same tension as the surrounding wafer. The effect of an applied differential pressure across the wafer is expected to be a change in the degree of bend of the beam. Any change in resonance frequency must then result from a change in the residual stress remaining in the bent beam. This residual stress is thought to be about two orders of magnitude lower than the relieved compressive stress [5] and the change in resonance frequency is expected to be almost negligible. A programme of experimental work has also been carried out to test this. The results of this work are described later in this chapter in Section 5:4.1.2.

5:2.2 Effect of Change in Temperature

We now analyse the effect of temperature the resonance frequencies of straight simple microresonator beams. It is proposed that the variation of resonance frequency with temperature is due to a combination of the thermal dependence of material parameters - Young's modulus and density - and the thermal dependence of beam stress.

We consider first the variation due to the thermal dependence of material parameters. The resonance frequencies of transverse vibrations of a simple homogeneous beam are given in Chapter 3, Section 3:2.1.1. From eqn.{3.2} in Section 3:2.1.1 we can write that for a simple homogeneous beam of length L and thickness a, the natural frequencies f_i of transverse flexural vibrations will obey the relationship

$$f_i \propto \left[\frac{a}{L^2}\right]\sqrt{\frac{E}{\rho}} \qquad \{5.6\}$$

where E is the Young's modulus and ρ is the density of the beam.

The change in frequency Δf due to the material linear expansivity α and a fractional change in Young's modulus ΔE for a change in temperaure ΔT may therefore be given by

$$\frac{\Delta f}{\Delta T} = \frac{1}{2}\left[\frac{\Delta E}{\Delta T} + \alpha\right] \qquad \{5.7\}$$

For a two-material beam a weighted mean of the thermal coefficients may be used as first approximations to be substituted into the eqn.{5.7}, so that for example the linear expansivity of the beam may be given by

$$\alpha_{overall} \approx \frac{a_s\alpha_s + a_m\alpha_m}{a_s + a_m} \qquad \{5.8\}$$

where a_s is the substrate thickness, a_m is the metal thickness, α_s is the expansivity of the substrate and α_m is the expansivity of the metal.

We consider now the variation due to the thermal dependence of beam stress. We have described in Chapter 3, Section 3:4.1, that in the absence of an external stress imposed on the microstructure, the beam is under fabrication-induced stress at room temperature [6]. We have also shown in Section 3:2.1.3 that standard beam theory predicts an increase in the resonance frequency of a prismatic beam with tension. The tension in the thin metal film is expected to be reduced as the temperature of the beam is raised and from eqn{3.5}, in Section 3:2.1.3, we can see that for a straight beam this will reduce the mean beam tension and therefore reduce the resonance frequency.

A general expression for the mean stress in a metal-coated silicon beam is given in Chapter 3, Section 3:4.1, eqn.{3.37}, and from this we can write

$$\sigma = \frac{a_m\sigma_B + a_s\sigma_A}{(a_m + a_s)} \qquad \{5.9\}$$

where σ_A is the magnitude of the fabrication-induced compression in the beam substrate material (in this case silicon), and σ_B is the magnitude of the fabrication-induced tension in the metal.

The thermal dependence of mean beam stress σ is given by

$$\frac{d\sigma}{dT} = \frac{\partial\sigma}{\partial\sigma_A}\frac{\partial\sigma_A}{\partial T} + \frac{\partial\sigma}{\partial\sigma_B}\frac{\partial\sigma_B}{\partial T} \qquad \{5.10\}$$

Whence, using eqn.{3.9},

$$\frac{d\sigma}{dT} = \frac{a_s}{(a_m + a_s)}\frac{\partial\sigma_A}{\partial T} + \frac{a_m}{(a_m + a_s)}\frac{\partial\sigma_B}{\partial T} \qquad \{5.11\}$$

The fabrication-induced stress in the silicon is not thermal in origin and the thermal dependence of the fabrication-induced stress in the metal is expected to dominate. Therefore we can write, for a metal-coated silicon beam,

$$\frac{d\sigma}{dT} \approx \frac{a_m}{(a_m + a_s)}\frac{\partial\sigma_B}{\partial T} \qquad \{5.12\}$$

The temperature coefficient of the resonance frequency of a metal-coated silicon beam due to the thermal dependence of beam stress is therefore expected to be greater for a greater metal coating thickness. Measurements of the temperature coefficients of resonance frequencies of silicon beams with different metal coating thicknesses are described in Section 5:4.2.1 of this chapter.

Again, the situation is expected to be different for a silicon dioxide beam. An increase in temperature for a metal-coated oxide beam is again expected to reduce the tension in the metal. However it has been suggested in Chapter 3, Section 3:4.1, that this fabrication-induced metal tension keeps the silicon dioxide beam substrate under compression by reducing the extent of the beam deformation. In this case an increase in temperature which reduces the metal tension will result in a reduction of the compression in the oxide. It is therefore expected that the polarity of the temperature coefficient of resonance frequency due to stress changes will depend on the relative thickness of the metal and the oxide.

The thermal dependence of the stress in a metal coated silicon dioxide beam may be expresses in terms of the relative thicknesses of the metal and the oxide in the following way. Again we can relate the thermal dependence of the mean beam stress σ in terms of the thermal dependences of the fabrication induced stresses in the oxide σ_A and in the metal σ_B using eqn.{5.10}. In addition we may use the expression for σ derived in Chapter 3, Section 3:4.1.2; eqn.{3.58}, which is transcribed below:

$$\sigma = \left\{ \frac{a_m}{a_m + a_s} \right\} \sigma_B - \sigma_A + \frac{\left\{ \sqrt{\sigma_A} + h\sqrt{\sigma_A - \sigma_B} \right\}^2}{(1+h)^2} \qquad \{5.13\}$$

Now the partial derivative of the mean beam stress with respect to the magnitude of the fabrication induced stress in the oxide may be obtained from this expression to be

$$\frac{\partial \sigma}{\partial \sigma_A} = -1 + \frac{1}{(1+h)^2}\left[1 + h\left[\frac{\sqrt{\sigma_A - \sigma_B}}{\sqrt{\sigma_A}} + \frac{\sqrt{\sigma_A}}{\sqrt{\sigma_A - \sigma_B}} \right] + h^2 \right]$$

{5.14}

where $h \equiv (a_m/a_s)^3$. Then if $\sigma_B \ll \sigma_A$

$$\frac{\partial \sigma}{\partial \sigma_A} \approx 0$$

{5.15}

Similarly from eqn.{5:13}

$$\frac{\partial \sigma}{\partial \sigma_B} = \frac{a_m}{(a_m + a_s)} + \frac{h}{(1+h)^2}\left[\sqrt{\frac{\sigma_A}{\sigma_A - \sigma_B}} + h \right]$$

{5.16}

Then if $\sigma_B \ll \sigma_A$

$$\frac{\partial \sigma}{\partial \sigma_B} \approx \frac{a_m}{(a_m + a_s)} - \frac{h}{(1+h)}$$

{5.17}

so that, for a metal-coated oxide beam, using eqn.{5.10},

$$\frac{d\sigma}{dT} \approx \left[\frac{a_m}{(a_m + a_s)} - \frac{h}{(1+h)} \right] \frac{\partial \sigma_B}{\partial T}$$

{5.18}

It can be seen from this expression that the polarity of the thermal dependence of beam stress for a metal-coated silicon dioxide beam does indeed depend on the relative thicknesses of the oxide and the metal. Measurements of the temperature coefficients of resonance frequencies of silicon dioxide beams with different metal coating thicknesses are described in Section 5:4.2.1 of this chapter.

It can also be seen, by comparing eqn.{5.18} with eqn.{5.12}, that we expect silicon and silicon dioxide beams to behave differently in response to a change in temperature. This is further discussed in Section 5:5.2 of this chapter.

5:3 Experimental Method

This chapter includes a description of experimental work carried out in order to demonstrate and measure the sensitivities of silicon and silicon dioxide micobeams to applied pressure and to temperature. All this work was carried out using the all-fibre two source system described in Chapter 4, Section 4:2.2. As described there, the microbeam vibrations were activated using a modulated helium-neon laser at a wavelength of 633nm and detected using a semiconductor laser at a wavelength of 1.3μm. Both laser beams were guided by an optical fibre single moded at 1.3μm, the end of which was held a few microns from the metal-caoted surface of the microresonator under test.

To measure the sensitivity of beam resonance frequencies to applied pressure a differential pressure was applied across the wafer thickness. This was achieved by the application of pressure to the back of the wafer while the front was exposed to the atmosphere.

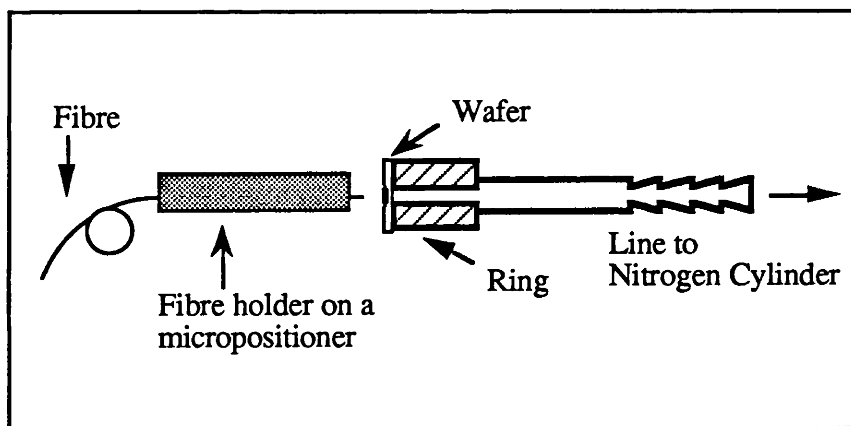

Figure 5.3: Apparatus for application of differential pressure across a silicon wafer with fibre probe.

Samples used consisted of pieces of irregular shape cut from silicon wafers on which microresonators had been fabricated, as described in Chapter 2, Section 2:4. These samples were mounted on small metal rings with a circular cross-section using a commercial epoxy. A range of metal rings were used with internal diameters of approximately 1mm. The rings were designed to be connected to a nitrogen cylinder via a tube. This is illustrated in Figure 5.3. In this way the portion of the wafer positioned over the central aperture in the metal ring would act as a pressure diaphragm, which would tend to bend as a differential pressure was applied across it. It can be seen that the front of the wafer, that is the side on which the resonators have been fabricated, may be freely accessed by the fibre probe.

Clearly it was necessary to mount the wafer on the metal ring in such a way that the microresonator under test was positioned over the central aperture, on the pressure diaphragm. It was not possible to make an accurate measurement of the position and orientation of the beams on the wafer relative to this aperture, since it was situated on the other side of the wafer, but the resonator under test was generally positioned as close to the aperture centre as possible. The pressure was measured using a simple gauge in units of p.s.i. to an accuracy of ± 1 p.s.i., where 1 p.s.i. = 6.895 bar.

The effect of temperature on resonator operation was investigated in the following way. The wafer piece was mounted on a Peltier heating block. To attach the wafer a thin layer of heat-sinking compound was used. To monitor the temperature a thermocouple was fixed to the metal-coated surface of the wafer within 6mm of the resonator, measured using an optical microscope. The temperature at this point could be measured to an accuracy of ±0.05K. Good thermal contact was ensured by fixing the thermocouple tip with thermally conductive glue. After each change was made in the heating block current, 3 minutes were allowed for the temperature to stabilise before measurements were taken.

5:4 Experimental Results

5:4.1 Effect of Applied Pressure

5:4.1.1 Silicon Resonators

The pressure sensitivity of a fibre-optic silicon microresonator was initially demonstrated using a beam fabricated on a silicon wafer of thickness 380μm. The microresonator beam examined was sputter-coated with gold and had small central wings, as illustrated in figure 3.2, Chapter 3, Section 3:2.1.2. These wings may allow additional absorption of the activating light, since they increase the surface area of the microresonator, but are expected to have negligible effect on the beam stress and on the predicted pressure coefficient of resonance frequency. The dimensions of this beam were as follows:

Stem Length 170μm; Stem Width 1.5μm; Thickness 0.5μm
Wing Length 15μm; Wing Width 1.5μm
Sputtered Gold Thickness 65nm

The wafer piece was mounted on a metal ring with an internal diameter of 2mm, as described in the previous section. The calculated shift in resonance frequency for such a beam positioned at the wafer centre, from eqn.{5.5}, is approximately 2.4% per bar.

The experimentally measured lowest resonance frequency of the mounted device was found to be 247KHz. A differential pressure of 4 bar was applied across the full wafer thickness. The resonance frequency rose from 247KHz to 250KHz. This shift corresponds to 0.3% per bar.

Having demonstrated that the resonance frequency did indeed shift with applied pressure, further measurements were made with other devices to determine first whether there was a discrepancy between the experimentally measured sensitivities and those predicted, and secondly whether the sensitivity could be increased.

It can be seen from eqn.{5.5} in Section 5:2.1 that the pressure sensitivity of resonance frequency may be expected to increase with decreasing wafer thickness. In order to achieve a higher sensitivity, the backs of a number of wafers on which resonators had been fabricated were chemically thinned down to about one half of the full wafer thickness of 380μm. The chemical process used is described in Chapter 2, Section 2:4.1.

The pressure sensitivities of four such devices were measured and compared with the sensitivities predicted using eqn.{5.5}. In all cases the relationship between the first experimentally measured resonance frequency and the applied differential pressure across the wafer was found to be linear over the range 0 - 4 bar with negligible hysteresis.

Three of these four samples were positioned on separate metal rings so that the microresonator under test was as near to the centre of the ring as possible. The dimensions of these three devices are given in table 5.1. The first measured resonance frequency of each microresonator, the measured pressure sensitivities and those predicted using eqn.{5.5} are given in table 5.2. The agreement between the measured and predicted values can be seen to be good. For two of these devices the resonance frequency is plotted as a function of applied pressure in figure 5.4 and figure 5.5.

The foutrh device was a microresonator situated on the same wafer piece as the first, about 200μm (estimated using an optical microscope) from the edge of the aperture in the metal ring. This beam exhibited a pressure sensitivity -3.1% per bar over the range 0 - 2 bar. The negative pressure sensitivity is thought to indicate that the resonator is in an area of compression of the wafer, as illustrated in figure 5.2.

The lowest resonance frequencies of the four devices were also measured before they were fixed to the metal rings. In each case the frequencies were shifted during the process of epoxy bonding. The mean difference in resonance frequency between bonded and unbonded devices was measured to be 7%.

These results are discussed further in Section 5:5.1 of this chapter.

Device	#2	#3	#4
Device geometry	paddled	simple	simple
Stem length / μm	165	170	175
Stem width / μm	2.0	2.0	2.0
Silicon beam thickness / μm	0.5	0.5	1.0
Paddle length	15	-	-
Paddle width	12	-	-
Metal coating	aluminium	aluminium	aluminium
Metal thickness / nm	200	200	250
Wafer thickness / μm	180	180	150
Aperture radius / μm	900	300	1000

Table 5.1: Dimensions of three devices tested for pressure sensitivity.

Device	#2	#3	#4
Lowest resonance frequency / KHz	210	235	426
Calculated frequency shift / % per bar	5.2	0.58	3.4
Measured frequency shift / % per bar	4.1	0.6	2.8

Table 5.2: Frequency shifts with applied pressure for three devices

Note: Frequency shifts have been calculated using eqn.{5.5}

Frequency shifts have been measured over a range 0 - 4 bar.

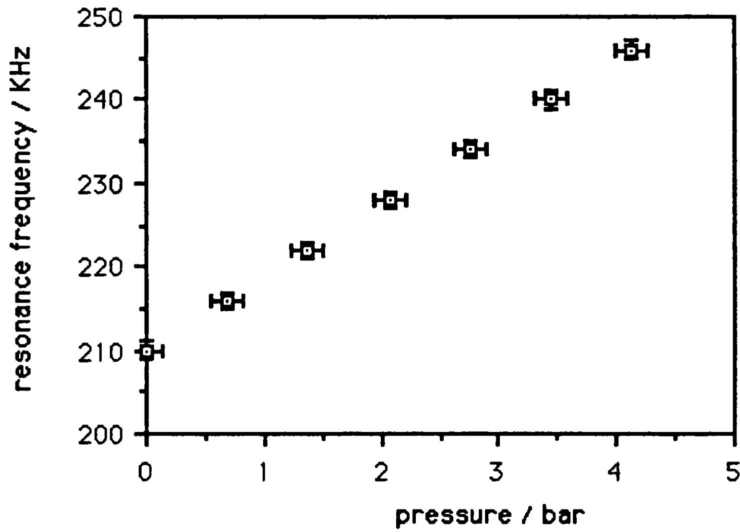

Figure 5.4: The pressure sensitivity of a silicon beam resonator device.
Note: the device is described as device #2 in table 5.1.

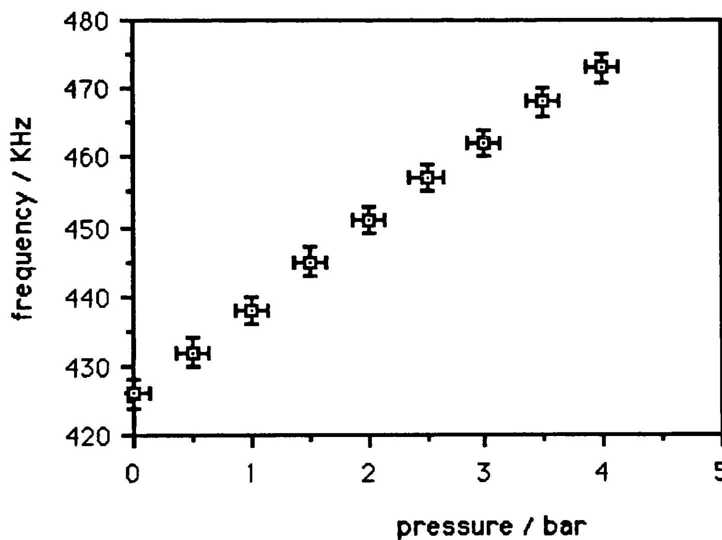

Figure 5.5: The pressure sensitivity of a silicon beam resonator device.
Note: the device is described as device #4 in table 5.1.

5:4.1.2 Silicon Dioxide Resonators

The pressure sensitivity of beam resonators fabricated from silicon dioxide thermally grown on a silicon wafer was also measured. The direct application of eqn.{5.5} suggests that the pressure sensitivities of SiO_2 beams will be comparable with those of equivalent Si beams. However, as described in Section 5:2.1 of this chapter, the sensitivities are expected to be significantly lower than this estimate because of fabrication-induced deformation.

A series of samples of silicon dioxide beams were examined using the set-up described above. These beams were of similar dimensions to the silicon ones described above and coated with a thin layer of evaporated aluminium or sputtered gold. One such beam is described as follows:

Length 185μm; Width 5.5μm; Thickness 0.5μm
Aluminium Thickness 200nm
Wafer thickness (d) 380μm Radius (R) 2500μm
Lowest resonance frequency: 230KHz
Calculated frequency shift (eqn.{5.5}): 11% per bar

The wafer pieces were mounted on metal rings with internal diameters of up to 5mm, as described in the previous section, in each case with the microresonator under test positioned near the centre of the aperture. Differential pressures of up to 4 bar were applied across the full wafer thickness of 380μm. The calculated shift in resonance frequency for the beam described above, from eqn.{5.5}, is approximately 11% per bar.

The experimentally measured lowest resonance frequency of the beam described above was found to be 230KHz. For all the microresonators examined, no shift in the resonance frequency was observed above the resolution bandwidth of 2KHz. It is clear that the pressure sensitivities of these microresonators are small compared with those of the silicon devices described in the previous section. It was however thought that it might be possible to observe a resonance frequency shift with applied pressure by decreasing the wafer thickness, as described in the previous section.

In order to achieve a higher sensitivity, the wafer thinning technique described in Chapter 2, Section 2:4.1, was again used.

The pressure sensitivities of three further devices were measured. These three microresonators were all situated on the same wafer piece which had been thinned to 150μm and was bonded to a metal ring with an internal diameter of 5mm. Each of these beams had a wider central area, as illustrated in figure 3.2, Chapter 3, Section 3:2.1.2, which may allow additional absorption of the activating light but is expected to have negligible effect on the beam stress and on the predicted pressure coefficient of resonance frequency.

The wafer piece was positioned on the metal ring so that one of the three microresonators under test was as close as possible to the centre of the aperture. The other two microresonators were each about 200μm (estimated using an optical microscope) from the centre of the aperture. The three beams may be described by the following dimensions:

Stem Length 180μm;	Stem Width 5.0μm;	Thickness 0.5μm
'Paddle' Length 35μm;	'Paddle' Width 12μm	
Aluminium Thickness 200nm		
Wafer thickness (d) 150μm	Radius (R) 2500μm	

The calculated shift in resonance frequency for such a beam positioned at the wafer centre, from eqn{5.5}, is approximately 64% per bar. This is relatively high because of the low wafer thickness and the large aperture radius.

In all cases a shift in resonance frequency could be measured when a pressure of 4 bars was applied across the wafer. The sensitivity of the lowest resonance frequency of the microresonator positioned near the centre of the ring's aperture was found to be 1.7% per bar over the range 0 - 4 bar. The relationship was linear over this range with negligible hysteresis. Figure 5.6 shows frequency plotted against applied pressure for this device.

The other two devices exhibited a pressure sensitivity of 0.3% per bar and of 0.5% per bar over the same range.

The lowest resonance frequencies of these silicon dioxide devicewere not effected by the process of epoxy bonding to the metal rings.

Although a frequency shift has been observed by increasing the device sensitivity, in all cases the measured shift is significantly lower than that which would be predicted by direct application of eqn.{5.5}, which does not account for the fabriction-induced beam deformation. This is in contrast with the results from metal-coated silicon beams described in the previous section.

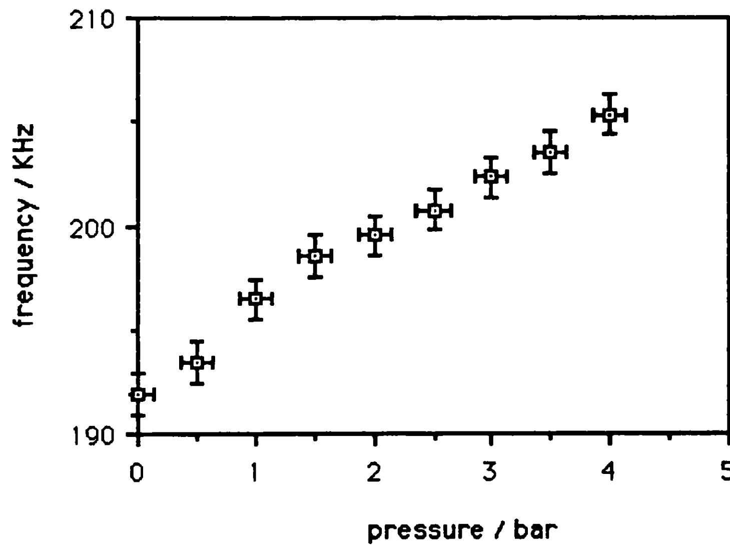

Figure 5.6: The pressure sensitivity of a silicon dioxide beam resonator.

5:4.1 Effect of Change in Temperature

5:4.2.1 Silicon Resonators

The pressure sensitivity of a fibre-optic silicon microresonator was demonstrated with three metal-coated beams. These beams each had a wider central area, as illustrated in figure 3.2, Chapter 3, Section 3:2.1.2. The dimensions of all three beams were as follows:

Stem Length 175μm; Stem Width 3.5μm; Thickness 1.0μm
'Paddle' Length 21μm; 'Paddle' Width 8.0μm

The beams were coated with different thicknesses of metal and in each case the lowest resonance frequency was measured over a range of temperatures as described in Section 5:3 of this chapter. The temperature coefficients of resonance frequency were not generally constant over the range 5 to 90^{0}C. However the first order coefficient was measured for each of the three microresonators and these results are given in table 5.3. The frequency is plotted against temperature for the devices described as #5 and #7 in this table, in figure 5.7 and figure 5.8.

It can be seen that the smallest temperature coefficient of resonance frequency is observed for the microresonator with the lowest metal coating thickness. These results are discussed further in Section 5:5.2 of this chapter.

Device	#5	#6	#7
Metal coating	aluminium	aluminium	gold
Metal thickness / nm	200	100	20
Measured frequency shift / % per °C	-0.17	-0.1	-0.01
Temperature range	5 - 60°C	25 - 80°C	25 - 90°C

Table 5.3: Frequency shifts with temperature for three devices.

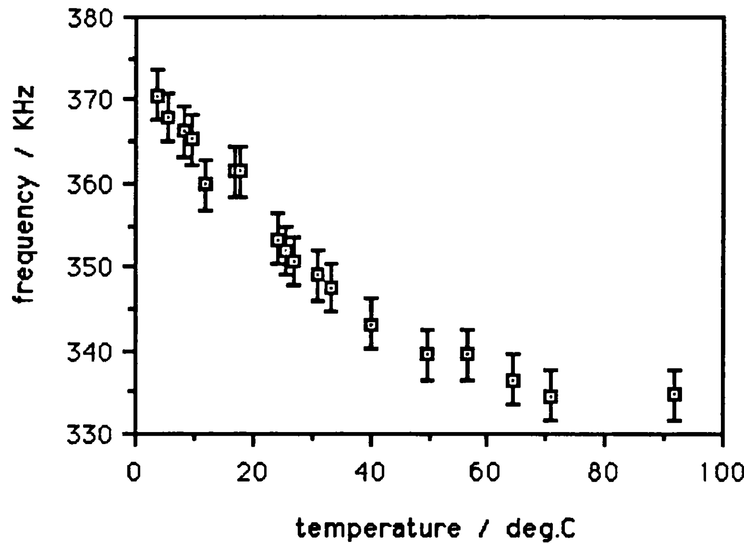

Figure 5.7: The temperature sensitivity of an aluminium-coated silicon beam resonator.

Note: the device is described as device #5 in table 5.3.

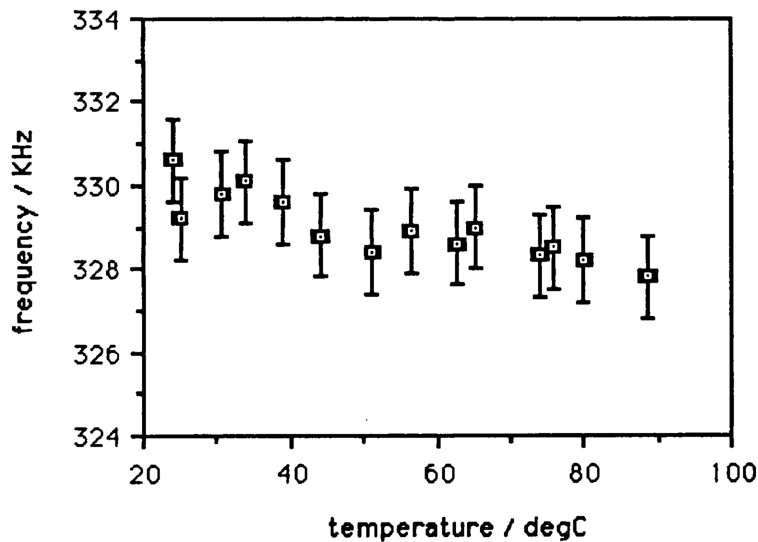

Figure 5.8: The temperature sensitivity of a gold-coated silicon beam resonator.

Note: the device is described as device #7 in table 5.3.

5:4.2.2 Silicon Dioxide Resonators

The pressure sensitivity of a simple fibre-optic silicon dioxide microresonator was also demonstrated using the experimental set-up described in Section 5:3 of this chapter. This beam is described by the following dimensions:

Stem Length 185μm; Stem Width 5.5μm; Thickness 0.5μm
The silicon dioxide device was coated with 200nm of evaporated aluminium.

The resonance frequency was measured over a temperature range of 23 to 68^{0}C. The resonance frequency is plotted against temperature over this range in figure 5.9. The temperature coefficient of resonance frequency between 23 and 68^{0}C is -0.15% / ^{0}C.

It was noted that this temperature coefficient of frequency, measured for a beam with the silicon dioxide thickness greater than the metal coating thickness, was negative. This is in agreement with the polarity predicted by using eqn.{5.18}, which describes the temperature coefficient in terms of the relative thicknesses of the silicon dioxide and the metal coating, and was derived in Section 5:2.2 of this chapter.

The validity of this prediction was further explored by the examination of a silicon dioxide beam with the silicon dioxide thickness less than the metal coating thickness. The dimensions of this resonator, which was a paddle beam, were as follows:

Stem Length 175μm; Stem Width 2.5μm; Thickness 0.15μm
Paddle Length 21μm; Paddle Width 8.0μm
This silicon dioxide device was coated with 200nm of sputtered gold.

The resonance frequency of this beam is plotted against temperature in figure 5.10. The temperature coefficient of resonance frequency between 25 and 90^{0}C is +0.62% /^{0}C.
The polarity of this coefficient, which is opposite to those measured for the silicon beams described in the previous section and to that of the silicon dioxide beam described above, is in agreement with the theory developed in Section 5:2.2 of this chapter, and with eqn.{5.18}. The results are further discussed in Section 5:5.2.

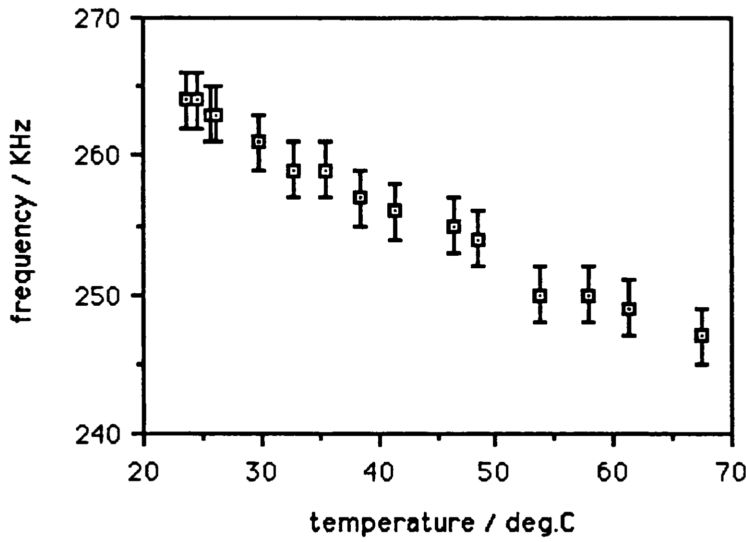

Figure 5.9: The temperature sensitivity of an aluminium-coated silicon dioxide beam resonator.

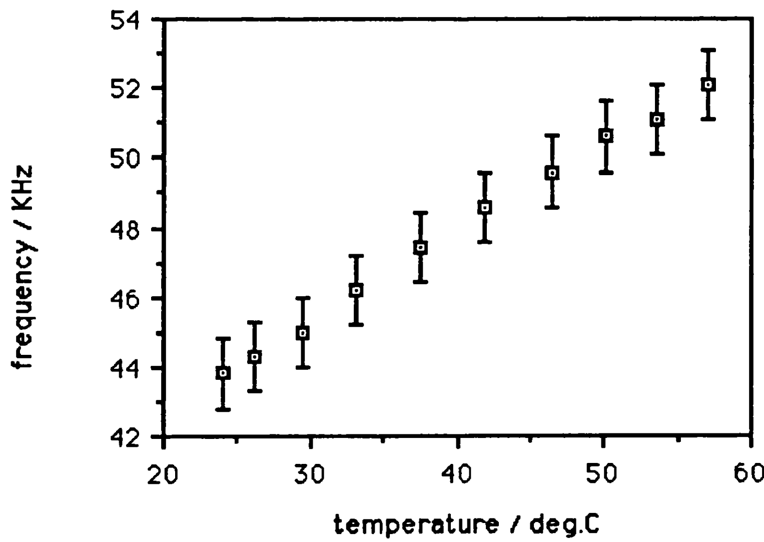

Figure 5.10: The temperature sensitivity of a gold-coated silicon dioxide beam resonator.

5:5 Discussion

5:5.1 Effect of Applied Pressure

Microresonator beams have been demonstrated acting as pressure sensors, activated and interrogated using a fibre-optic system.

The metal-coated silicon devices examined exhibit sensitivities to applied pressure in broad agreement with those predicted by standard beam theory. Discrepancies are attributed principally to the uncertainty in the position and orientation of the beams on the silicon wafers, which the theory indicates is significant, as well as uncertainty in the physical constants of silicon and the precise dimensions of the device. Beams on different parts of the same wafer are shown to exhibit pressure sensitivities of opposite polarity, as the theory predicts. In addition the standard theory ignores the effect of the etch pit beneath the resonator beam. To optimise the pressure sensitivity reliably it will be desirable to position the beam in the centre of the wafer.

A further problem is that additional stress is introduced to the beams during the process of epoxy bonding the wafers to the mounting ring. This stress has been seen to cause a significant change in resonance frequency. The sensors are expected to be exposed to hostile, or even abrasive, environments, and the bond attaching the silicon-based structure to the fibre must be strong. In biomedical applications the use of epoxies or other organic adhesives which may give rise to contaminations are not suitable, but for other applications, adhesives were thought to be be the most convenient answer to the bonding problem. The most promising alternative is anodic bonding [7] which, however, is a much more complex process involving the application of an electric field at an elevated temperature.

In order to maximise the pressure sensitivity of a silicon beam structure for pressure measurement applications, it is desirable to use as thin a diaphragm as possible. It has been shown that the pressure sensitivity may be significantly increased by thinning the wafer on which the device is fabricated. This can be seen from eqn.{5.5}. The chemical thinning method used, although successful, produced wafers of uneven thickness and with a rough surface. Furthermore, it was not

possible to produce wafers less than 150μm thick. These problems could be overcome by wafer polishing, by which wafers may be thinned to less than 40μm. Diaphragms around 25μm thick can also be fabricated using a chemical etch-stop method [3]. It can also be seen from eqn.{5.5} that the pressure sensitivity will ncrease with the slenderness ratio, that is the ratio of the length to the thickness, of the beam. Further experimental work is needed to show these relationships empirically and to design an optimised pressure sensor.

The metal-coated silicon dioxide beams are shown to exhibit a significantly lower pressure sensitivity of resonance frequency. This is thought to be a result of the beam deformation induced during fabrication, which prevents transmission of the wafer surface stress to the beam. Any change in resonance frequency must then result from a change in the residual stress remaining in the bent beam. Silicon is therefore a more suitable material for microresonator pressure sensors than thermally-grown SiO_2. The low pressure sensitivity of oxide beams may be of potential advantage in other applications, for example where epoxy bonding is an attractive method of fixing the sensor structure to the optical fibre probe. No shift in resonance frequency of oxide beams was observed when these structures were epoxy bonded to the metal mounting ring.

5:5.2 Effect of Temperature Change

Microresonator beams have also been demonstrated acting as temperature sensors, activated and interrogated using a fibre-optic system.

The variation of resonance frequency with temperature is shown to be due to a combination of the thermal dependence of material parameters and the thermal dependence of the beam stress. The variation in frequency due to the thermal dependence of material parameters may be calculated using eqn.{5.7} and eqn.{5.8}. Data for coefficients of linear thermal expansivity α [8] and thermal variation of Young's modulus Θ [9,10] are shown in table 5.1.

Material	α / ppm K^{-1}	Θ / ppm K^{-1}
Si	2.3	-52
SiO_2	0.4	192
Al	14	-480
Au	24	-480

Table 5.1: Material data for linear thermal expansivity and thermal variation of Young's modulus for some microrsonator beam materials. [References 8,9,10]

It has been pointed out [11] that although most materials have a negative temperature coefficient of Young's modulus, SiO_2 has a quite large positive coefficient. It is therefore possible to design a composite structure with zero nett thermal dependence of material parameters. However this cannot be done with a metal-coated silicon beam unless account is taken of the thermal variation of the beam stress.

The variation in frequency due to the thermal dependence of material parameters is calculated in this way for the silicon and silicon dioxide beams examined in this chapter. The coefficient for the metal-coated silicon dioxide beams is more critically dependent on the relative thicknesses of the oxide and the metal because of the opposite polarities of the temperature coefficients of the Young's moduli of these different materials. The calculated magnitude of this coefficient for the beams examined is never greater than 0.02% / ^{0}C, and for the silicon beams the coefficient is always negative.

These calculations show that both for silicon and for silicon dioxide beams the thermal dependence of material parameters cannot fully account for the observed frequency shifts. It is postulated that the thermal dependence of beam stress is also a

significant factor in determining the thermal variation of resonance frequency for both silicon and silicon dioxide beams.

The fabrication-induced stress in the resonator, which has been discussed in Chapter 3, Section 3:4.1, is also expected to be affected by a change in temperature. The thermally-induced component of the fabrication-induced metal stress is thought to be related to the difference between the ambient temperature and the metal recrystallisation temperature [12]. The tension in the thin metal film is thus expected to fall as the temperature of the beam is raised. The thermal dependence of the fabrication-induced stress in the silicon is assumed to be negligible and an expression has been derived relating the thermal dependence of beam stress to the thermal dependence of the fabrication-induced metal stress (eqn.{5.8}). From this expression, therefore, it can be seen that the fabrication-induced beam stress will fall as the temperature of the beam is raised. The resonance frequency will also fall as a result of the change in fabrication-induced stress as the temperature of the beam rises (eqn.{3.57}, Section 3:4.1.2, Chapter 3).

The experimental results, which show a negative temperature coefficient of resonance frequency for metal-coated silicon beams, support this conclusion. The magnitude of this frequency change will depend on the temperature variation of the metal stress, for which no published values are available. It can be seen from eqn.{5.8} that as the metal thickness a_m becomes very small compared with the silicon thickness a_s, then the temperature coefficient of resonance frequency becomes very small also. The experimentally measured temperature coefficient of resonance frequency for a 1μm thick silicon beam sputter-coated with 20nm of gold is -0.01%/^{0}C, which is close to the value derived above for the variation in frequency due to the thermal dependence of material parameters.

The temperature sensitivity of a silicon beam pressure sensor may thus be reduced by minimising the thickness of the metal coating. Alternatively a compensation scheme may be incorporated in the sensor head. An example of such a method is the excitation of a beam and a cantilever using a single multimode fibre, the separate frequency signals from which are to be decoded electronically away from the sensor head to provide a compensated measurement of pressure.

An increase in temperature for a metal-coated oxide beam will reduce the tension in the metal, but this will result in a reduction of the compression in the oxide so that the polarity of the temperature coefficient of resonance frequency due to stress changes will depend on the relative thickness of the metal and the oxide. Expressions have been derived relating the thermal dependence of beam stress to the thermal dependence of the fabrication-induced metal stress and to the thermal dependence of the fabrication-induced oxide stress (eqns.{5.14}-{5.18}).

It can be seen from eqn.{5.18}, relating the thermal dependence of beam stress $d\sigma/dT$ to the thermal dependence of the fabrication-induced stress in terms of the metal thickness a_m and the oxide thickness a_s that:

if $0 < a_m < a_s$ then $d\sigma/dT > 0$

if $a_m > a_s > 0$ then $d\sigma/dT < 0$

if $a_m = a_s$ then $d\sigma/dT = 0$.

The experimental results presented support this pattern, and show that the temperature coefficient of resonance frequency for a metal-coated silicon dioxide beam may be positive or negative.

The temperature sensitivity of the fabrication-induced stress in the metal is assumed to be constant with temperaure (i.e. $\partial^2\sigma_B/\partial T^2 = 0$), and the equation (eqn.{5.18}) is differentiated with respect to a_m/a_s. We find that $d\sigma/dT$, and therefore the temperauture coefficient of resonance frequency, is a maximum (greatest positive magnitude) when $a_m \approx 0.44\, a_s$ and a minimum (greatest negative value) when $a_m \approx 2.3\, a_s$. Further work is required to explore the validity of this relationship experimentally. It is important to note that the temperature sensitivity of resonance frequency is critically dependent on the metal thickness. For an SiO_2 beam temperature sensor, the integrity of the fabrication process is therefore important, unless the sensor heads can be individually callibrated. For other applications, the theory indicates that it is possible to fabricate a beam with temperature coefficient close to zero by coating the oxide with an equal thickness of metal. An alternative is to use a compensation scheme such as that proposed for silicon devices above.

5:6 Conclusions

We have successfully demonstrated fibre-optic metal-coated silicon microresonator beams, and fibre-optic metal-coated silicon dioxide microresonator beams, acting as sensors. The sensitivity of the devices to pressure and to temperature has been demonstrated in both cases.

We have also analysed the effect of an applied differential pressure and of a change in temperature on these two types of microresonator. We have found that the metal-coated silicon beams exhibit a significantly higher pressure sensitivity of resonance frequency than the metal-coated silicon dioxide beams. This is thought to be a result of the silicon dioxide beam deformation induced during fabrication.

We conclude that silicon is therefore a more suitable material for microresonator pressure sensors than thermally-grown SiO_2. Further work is needed to optimise these devices as pressure sensors. We have found that the temperature sensitivity of a silicon beam pressure sensor may be reduced by minimising the thickness of the metal coating.

The low pressure sensitivity of oxide beams may be of potential advantage in other applications, for example where epoxy bonding is an attractive method of fixing the sensor structure to the optical fibre probe. No shift in resonance frequency of oxide beams was observed when these structures were bonded to the metal mounting ring.

An expression has been derived to relate the temperature sensitivity of resonance frequency to the temperature for these devices. Initial experimental results have been in agreement with the pattern predicted by this theory. The temperature sensitivity of resonance frequency is shown to be critically dependent on the metal thickness. For an SiO_2 beam temperature sensor, the integrity of the fabrication process is therefore important, unless the sensor heads can be individually callibrated. For other applications, the theory indicates that it is possible to fabricate a beam with temperature coefficient close to zero by coating the oxide with an equal thickness of metal. An alternative is to use a compensation scheme.

References for Chapter 5

1. K.E.B. Thornton *et al.*; "*Temperature Dependance Of Resonance Frequency In Optically Excited Diaphragms*"; Electronics Lett., Vol.22, pp 1232-1234, 1987
2. D. Uttamchandani *et al.*; "*Optically Excited Resonant Diaphragm Sensor*"; Electronics Lett. Vol. 23, pp 1333-1334, 1987
3. K.E.B. Thornton *et al.*; "*Novel Optically Excited Resonant Pressure Sensor*"; Electronics Lett., Vol.24, pp 573-574, 1988
4. A.C.M.Gieles and G.H.J.Somers 1973; "*Miniature pressure tranducers with silicon diaphragm*"; Philips Tech. Rev., vol. 33, pp14-20, 1973
5. S.C.H.Lin and I.Pugacz-Muraszkiewiz; "*Local stress measurement in thin thermal SiO_2 films on Si substrates*"; J.Appl. Phys., vol.43, pp119-125, 1972
6. L.Eckertova "Physics of Thin Films" ; Plenum Press, New York, 1977
7. W.K.Liu; "Si-Silica Fibre Bonding Investigations"; M.Sc. Thesis submitted to the University of London, 1987 (unpublished)
8. G.W.C.Kaye & T.H.Laby; "Physical and Chemical Constants"; Longmans, Green & Co., London, 12th ed., 1959
9. F.E.Fowle; "Smithsonian Physical Tables"; The Smithsonian Institution, Washington City, 8th ed., 1933
10. H.J.McSkimin; "*Measurement of Elastic Constants at Low Temperatures by means of Ultrasonic Waves - Data for Silicon and Germanium Single Crystals and for Fused Silica*"; J.Appl.Phys., Vol.24, pp988-997, 1953
11. M.B.Othman and A.Brunnschweiler; "*Electrothermally Excited Silicon Beam Mechanical Resonators*"; Electronics Lett., Vol.23, pp 728-729, 1987
12. H.P.Murbach & H.Wilman; "*The Origin of Stress in Metal Layers Condensed from the Vapour in high Vacuum*"; Proc.Phys.Soc.London, Vol.66B, pp905-910, 1953

CHAPTER 6: SELF-EXCITATION OF MICRORESONATORS

6:1 Introduction

6:2 Analysis

6:2.1 Mechanism of self-excitation

6:2.2 Conditions for self-excited vibrations

6:3 Experimental Method

6:4 Experimental Results

6:4.1 Initial observation of self-excitation

6:4.2 Further observations

6:4.3 Temperature variation of frequency

6:4.4 Multiplexing of self-excited devices

6:5 Conclusions

References for Chapter 6

CHAPTER 6

SELF-EXCITATION OF MICRORESONATORS

6:1 Introduction

In the previous chapter the results of experimental measurements of the sensitivity of beam microresonators were described. It was demonstrated that the frequency outputs from silicon devices were sensitive to and thus suitable to measure pressure, and that silicon dioxide devices were relatively insensitive to pressure and thus potentially robust and suitable to measure temperature in a range of environments. In Chapter 1, Section 1:7, a number of other potential applications of fibre-optic microresonator sensors were also discussed.

All the work in this project described previously has made use of a two-source fibre-optic system. The first optical source is intensity-modulated to drive the resonator vibrations. The second optical source emits unmodulated light which has intensity modulation imposed on it by reflection from the vibrating surface of the microresonator beam.

In order to simplify the requirements of the fibre-optic system, it would be attractive to demonstrate microresonator vibrations using a single, unmodulated, optical source. This may be accomplished if self-excited resonators are used, maintaining themselves at resonance by optical feedback. This feedback might be provided by a Fabry-Perot interferometer [1] formed between the partially reflective surface of the microresonator and another reflective surface in the system, such as the fibre end a few microns from the microresonator. The use of these interferometric fringes as a source of temporal intensity modulation was suggested in Chapter 3, Section 3:4. The amplitude of resonant vibration of microresonators, such as those considered in this chapter, was calculated to be of the order of 100nm, which is comparable with the spatial period of the interferometric fringes.

Such a system of optical self-excitation has been formally proposed by R.M.Langdon *et al.*, and experiments reported using a bulk optical system and polyester cantilevers

10mm long, which could be self-excited for short periods [2]. They reported that they were unable to achieve self-excitation of microresonators.

In this chapter a single-source fibre-optic system is described in which self-excitation of metal-coated silicon dioxide devices was achieved, the required feedback being provided by a Fabry-Perot cavity formed between the microresonator surface and the end of the optical fibre.

The effect of temperature on resonator operation has also been investigated. In this way a self-excited temperature sensor is demonstrated.

The use of self-excitation would also help to overcome a practical problem with regard to multiplexed operation. The conventional need for a source modulated at the resonance frequency of the micromechanical device imposes complex requirements on multiplexed sensor systems. This is because each sensor being multiplexed will have a different resonance frequency at which it must be excited and which has to be monitored. This problem is overcome if self-excited sensors are used, since no source modulation is required. In this chapter the multiplexing of two microresonator devices using a single optical source is also demonstrated.

6:2 Analysis

6:2.1 Mechanism of Self-Excitation

We consider microresonator beams maintained at resonance by optical feedback provided by a interferometric fringes formed between the partially reflective surface of the microresonator and the fibre end a few microns from the microresonator.

We initially assume that the end face of the fibre is flat and parallel to the surface of the vibrating microbeam, and that the activating light traverses the gap between these surfaces as a parallel beam. The position of the resonator relative to the fibre end is shown in figure 6.1. The light is assumed to be incident at the beam centre.

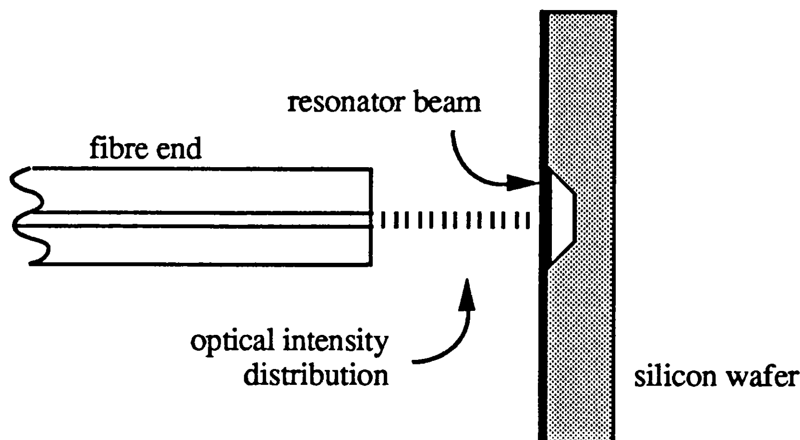

Figure 6.1: Sketch of fibre end and silicon wafer.

The total absorbed optical intensity can be calculated as a series of terms in the usual way for a Fabry-Perot interferometer [1], so that the light absorbed at the metal-coated surface of the resonator can be written:

$$\Psi_{abs.} = \beta \Psi_0 \left\{ 1 + r_1^2 r_2^2 - 2 \cos \{4\pi d/\lambda\} \right\}^{-1} \qquad \{6.1\}$$

where β is the coefficient of absorption at the metal-coated surface of the beam, d is the distance between the metal-coated surface of the beam and the fibre end, λ is the wavelength of the light, r_1 is the reflection coefficient at the fibre end, and r_2 is the reflection coefficient at the metal-coated resonator.

If $r_1 r_2 \ll 1$, then we can write the approximate relationship

$$\Psi_{abs.} \propto 1 + \frac{2r_1 r_2}{1 + r_1 r_2} \cos \{4\pi d/\lambda\} \qquad \{6.2\}$$

The light absorbed will therefore depend on the distance between the beam surface and the fibre end according to the same relationship. Figure 6.2 shows the form of the absorption as a function of this distance.

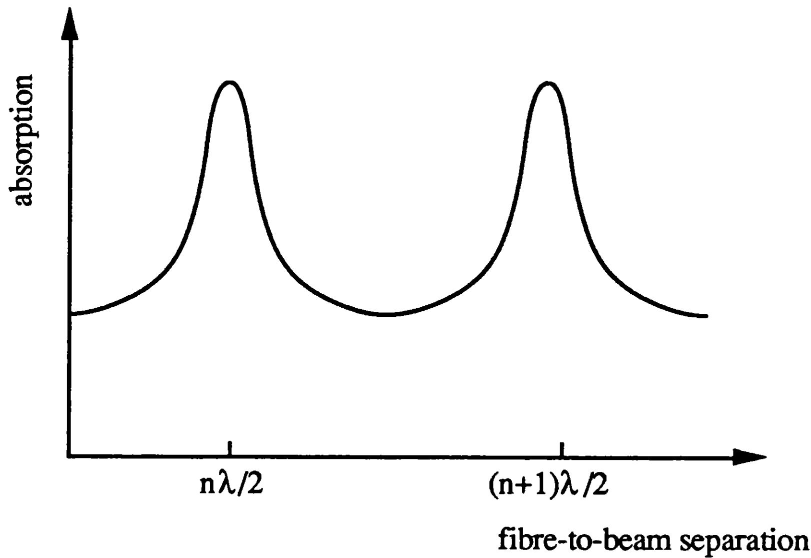

Figure 6.2: Absorption of light at resonator surface as a function of distance between the beam and the fibre end.

We consider the resonator vibrating harmonically at a frequency f. Then the absorbed intensity $\Psi_{abs.}$ will vary harmonically with time according to the relationship

$$\Psi_{abs.} \propto 1 + \frac{2r_1r_2}{1 + r_1r_2} \cos\left\{\frac{4\pi}{\lambda}(D + y_0 \sin 2\pi ft)\right\} \qquad \{6.3\}$$

where y_0 is the amplitude of the vibrations, and D is the mean distance between the beam and the fibre end. The beam will thus effectively experience a temporally varying intensity absorption.

It can be seen that near a point of inflexion on the absorption curve shown in figure 6.2, the relationship between absorption and fibre-to-beam separation is approximately linear over a small range. The laser sources used throughout the experimental work described in this project emit light at wavelengths of the order of 1μm. The period of the absorption curve shown in figure 6.2 is then approximately 500nm. We assume that the amplitude of vibrations is of the order of 100nm, as

indicated by the analysis in Chapter 3, Section 3:3.1. It can be seen that if the mean separation between the beam and the fibre is near to an inflexion point on the absorption curve of figure 6.2, then the temporally varying intensity absorption experienced by the beam may then approximate to a sinusoidal variation at a frequency f. Thus the form of the optical drive experienced by the vibrating microresonator is similar to that of a modulated optical source.

6:2.1 Conditions for Self-Excited Vibrations

The temporally varying intensity absorbed by the resonator will sustain the beam in resonant vibrations in the same way as an externally modulated drive (described in Chapter 3, Section 3:3.1) if two conditions are satisfied. First the phase relationship between the optical intensity variation and the position of the beam must be such as to maintain vibrations, rather than to damp them. Secondly the optical power must be sufficient to sustain vibrations.

We first consider the phase condition. We know from standard theory that at resonance the displacement of any resonator must lag the drive by $\pi/2$ radians. The thermal drive of the resonance vibrations is assumed to be of the same phase as the mean beam temperature. Therefore, for resonant vibrations to be maintained, the displacement of the beam centre must lag the mean beam temperature by $\pi/2$ radians.

The phase relationship between the optical intensity and the mean beam temperature can be found from the analysis of the opto-thermal conversion of energy described in Chapter 3, Section 3:3.1. We may write, directly from eqn.{3.12} and eqn.{3.31}, that for an intensity modulated optical drive,

$$\Psi_{act.} \propto (1 + m \cos \omega t) \qquad \{6.4\}$$

where $\Psi_{act.}$ is the optical intensity incident on the resonator beam, m is the modulation index, and ω is the angular modulation frequency; and also that

$$T_{mean} \propto \cos (\omega t - \pi/2) \qquad \{6.5\}$$

where T_{mean} is the oscillatory component of the mean beam temperature.

Comparison of eqn.{6.4} and eqn.{6.5} indicates that the mean beam temperature lags the incident optical intensity by $\pi/2$ radians. Therefore, for resonant vibrations to be maintained, the displacement of the beam centre must lag the incident optical intensity by a total of π radians.

This condition will be met for amplitudes of vibration significantly smaller than the wavelength of the light, as we have assumed, when the maximum of incident optical intensity corresponds to the minimum beam centre displacement from the fibre end, and the minimum of incident optical intensity corresponds to the maximum beam centre displacement from the fibre end. This will be true, as can be seen by examination of figure 6.2, if the mean distance between the beam surface and the fibre end is near to the point of inflexion at which

$$d = \frac{4n\lambda + 1}{8} \qquad \{6.6\}$$

Secondly we consider the optical power necessary to sustain vibrations. We substitute into eqn.{6.3} typical values for the coefficients of reflection at the fibre end and at the metal-coated surface of the beam, $r_1 = 0.2$ and $r_2 = 0.95$, and derive an expression for the fractional change in absorbed intensity as

$$\frac{\Delta\Psi_{abs.}}{\Psi_{abs._0}} = \frac{0.37\left\{\cos\left(4\pi\left(D+y_0\right)/\lambda\right) - \cos\left(4\pi\left(D-y_0\right)/\lambda\right)\right\}}{1 + 0.37\cos\left(4\pi D/\lambda\right)} \qquad \{6.7\}$$

We investigate the case where D is defined as equal to d given in eqn.{6.6}, and substitute $\lambda = 1.3\mu m$ and $y_0 = 100nm$ into eqn.{6.7}, whence

$$\frac{\Delta\Psi_{abs.}}{\Psi_{abs._0}} \approx 0.44 \qquad \{6.8\}$$

This fractional change in absorbed intensity, which corresponds to a modulation index of 0.22, is of the same order as we have used in driving microresonator vibrations from an externally modulated optical source in previous experimental work described in Chapter 4. We therefore expect to be able to sustain self-excited vibrations by using a comparable optical power.

The condition for self-excitation can be expressed in terms of the central beam

deflection per unit drive power X', the fractional change in absorbed intensity per unit central beam displacement $\Delta\Psi'$, and the total power input P_{in} so that for sustained vibrations

$$X' \,.\, \Delta\Psi' \,.\, P_{in} \; > \; 1 \qquad \{6.9\}$$

A first order estimate of the minimum power required is may be made by obtaining a value for the deflection per unit drive power from Chapter 3, Section 3:3.1, so that

$$X' \;\approx\; 100\text{nm} / 100\mu\text{W} \;=\; 1\mu\text{m} / \text{mW} \qquad \{6.10\}$$

The fractional change in absorbed intensity per unit beam displacement is estimated from eqn.{6.8}, so that

$$\Delta\Psi' \;\approx\; 0.44 / 100\text{nm} \;=\; 4.4 / \mu\text{m} \qquad \{6.11\}$$

In this way the minimum power required to sustain vibrations is found from eqn.{6.9} to be of the order of 200μW.

6:3 Experimental Method

The first experiments on self-excited vibration [3] were performed using the two-source fibre-optic system described in Chapter 4, Section 4:2.1, and shown in figure 4.2. In this case an unmodulated GaAs 1.5mW laser emitting at 820nm was used as the source, and light from the modulated HeNe laser was blocked at the Bragg cell so that it was not launched into the fibre. The fibre used was single-moded at 820nm.

Further experimental work was carried out [3] using the fibre-optic system shown schematically in figure 6.3. Initially a 1.3μm S.T.C. GaInAsP 1mW pigtailed semiconductor laser was used as the source in this system. The light was coupled into a fused fibre directional coupler using a x20 microscope objective. In further experiments a 2mW HeNe laser emitting at 633nm was used. At 633nm the fibre supported four modes of propagation and the coupler had a split ratio of approximately 9:1 at this wavelength. The coupler was arranged so that in this case 90% of the launched power propagated in the direction of the wafer.

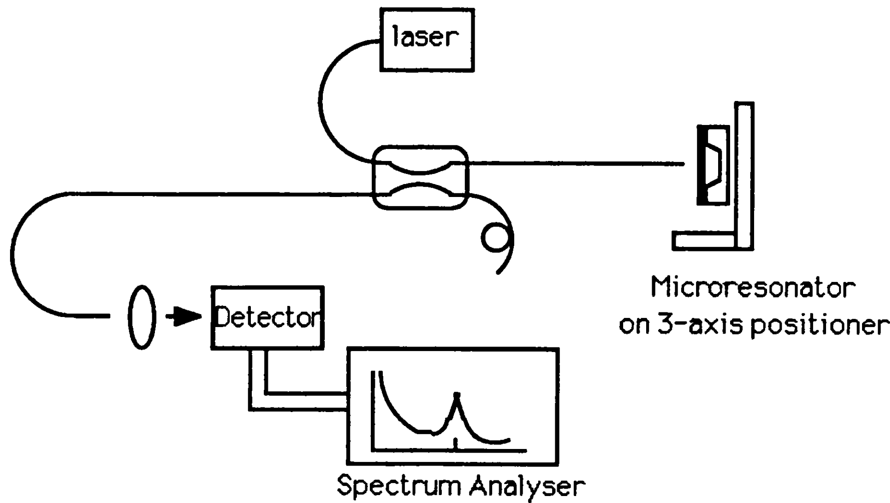

Figure 6.3: Schematic of single-source fibre-optic system.

The fibre end from one of the coupler output ports was held within a few microns of the surface of the micromechanical device under study. Precautions in the positioning and preparation of the fibre end were taken in the same way as has been described in Chapter 4, Section 4:2.1. An interferometer is formed between the fibre end and the microresonator as described in Section 6:2.1. of this chapter.

The non-linearity in the intensity distribution pattern set up between the fibre end and the strip surface, means that the reflected light coupled back into the fibre will be modulated at multiples of the resonance frequency of the microresonator. The relative magnitudes of the signal peaks at these frequencies will therefore depend upon the position of the vibrating strip on the intensity distribution pattern.

Unmodulated light from the laser was directed at the central area of this strip. An all-monomode system was also used to excite microresonator vibrations with an unmodulated 1.3μm semiconductor pigtailed laser. In this case the devices under test were mounted on a three-axis voltage-controlled micropostioner so that the strip could be positioned accurately and the dependence of the output signal on its position relative to the fibre end could be examined. Translations of the order of 50nm could be measured. A second device could also be held on a similar voltage-controlled

micropositioner a few microns from the free fibre end from the second output port of the fibre coupler (see figure 6.3). Resonance frequencies were measured on a spectrum analyser using a resolution bandwidth of 100Hz.

The effect of temperature on self-excited resonator operation was investigated in the same way as has been described in Chapter 5, Section 5:3.

6.3 Experimental Results

6:3.1 Initial observation of self-excitation

Self-excited vibrations of a microresonator were first observed in June 1979, in the course of this work. The fibre-optic system used was the the two-source fibre-optic system described in Chapter 4, Section 4:2.1, and shown in figure 4.2, with the modulated HeNe laser was blocked at the Bragg cell so that it was not launched into the fibre. The activating source was an unmodulated GaAs 1.5mW laser emitting at 820nm, and the fibre used was single-moded at 820nm.

The microresonator under test was a simple beam of thermally grown silicon dioxide coated with evaporated aluminium. The silicon dioxide beam was approximately 200μm long, 5μm wide and 0.5μm thick, and the aluminium coating was approximately 200nm thick. This beam was initially examined using the modulated HeNe laser at 200μW to excite vibrations, and the unmodulated GaAs laser at 200μW to detect vibrations. The lowest resonance frequency measured for this device was 202KHz, with a signal-to-noise ratio (SNR) of 42dB. When the modulated source was blocked a 5dB signal was still observed, indicating self-excited vibrations. The signal could be maintained at this level for periods of a few seconds only.

Similar observations were made with several aluminium-coated silicon dioxide beams of the same type. Further investigations and detailed observations could not be made because of the magnitude and instability of the signals observed. It was expected that the signal magnitude might be increased if the central beam deflection per unit drive power was increased.

6:3.2 Further observations

We consider the analysis of the opto-thermal conversion of energy described in Chapter 3, Section 3:3.1, with a view to increasing the signal from a self-excited microresonator. It can be seen from eqn.{3.8} that the mean oscillatory temperature of the beam, and hence the central beam deflection, will increase with decreasing beam specific heat capacity. The specific heat capacity may be reduced by using gold instead of aluminium as a metal layer. A further reduction may be made by reducing the thickness of the silicon dioxide, as can be seen from eqn.{3.29}.

It may be noted that a metal-coated oxide beam with a thinner oxide layer will also have significantly lower resonance frequencies. This is a result not only of the decrease in overall thickness of the beam, which can be seen to reduce the resonance frequencies from eqn.{3.2} in Chapter 3, Section 3:2.1.1, but also of the reduced fabrication-induced tension in the metal coating, as discussed in Chapter 3, Section 3:4.1.2. It was also considered that the resonance frequencies could be still further reduced, as indicated by eqn.{3.3}, and the optical absorption maximised, by using paddle beams as described in Chapter 3, Section 3:2.1.2.

We therefore fabricated several batches of thinner silicon dioxide paddle beams using the techniques described in Chapter 2, Section 2:5. The oxide thickness of all these devices was approximately 0.15μm, and they were coated with sputtered gold of thickness approximately 0.2μm. The beams examined were approximately 190μm long and 2.5μm wide at each end, with a paddle of length 20μm and width 14μm.

The fibre system was simplified as shown in figure 6.3, and an unmodulated HeNe laser, as described in Chapter 4, Section 4:2.2, was used as the optical source. The detector was based on a silicon *pin* photodiode. At the wavelength of this laser, which was 633nm, the fibre used could support four modes.

The fibre end was held approximately 5μm from the surface of a typical beam with dimensions as described above, and unmodulated light from the semiconductor laser was directed at the central area of the beam. The beam examined was found to be driven into vibration in response to unmodulated HeNe light incident on the central

paddle of the beam. The spectrum of the reflected light signal for an incident intensity of 600μW is shown in figure 6.4. A number of peaks can be seen at integer multiples of the resonance frequency of the beam as expected. The quality factor of the vibrations was estimated from a trace of the lowest frequency peak, that is at the fundamental resonance frequency of the strip, to be about 50. Self-excitation was sustained at the resonance frequency of this beam with an observed SNR of 40dB over a period of several hours.

Further measurements on similar microresonator beams were made [4,5] using a 1.3μm pigtailed semiconductor laser, as described in Chapter 4, Section 4:2.2, as the optical source, and replacing the detector with a germanium photodiode with a peak response at 1.3μm. The fibre used in this system was single-moded at 1.3μm. This allowed a significant increase in optical power incident on the resonator, up to approximately 1mW.

At an incident power of 250μW a series of evenly spaced resonance peaks could be observed on the spectrum analyser, as the strip vibrated in its fundamental flexural mode at about 14KHz. This response is shown in figure 6.5. The signal-to-noise ratio (S.N.R.) of the primary peak was measured on the spectrum analyser to be greater than 60dB.

The presence of the response signal was found to be dependent on the lateral position of the fibre end relative to the resonator beam surface. Observation of self-excitation was only possible when the fibre end was positioned within an area of approximately 18μm length and 12μm width, corresponding approximately to the beam paddle dimensions.

The amplitude of the peaks was also found to depend critically and cyclically on the distance between the fibre tip and the surface of the microresonator. This is illustrated in figure 6.6, which shows the relationship between the distance of the fibre tip from the microresonator and the number of signal maxima from the reference position over a distance of approximately 15μm. The distance was measured to an accuracy of ±100nm, and to this accuracy there was no observed hysteresis on this curve. The mean distance between maxima was 640nm for 1.3μm light.

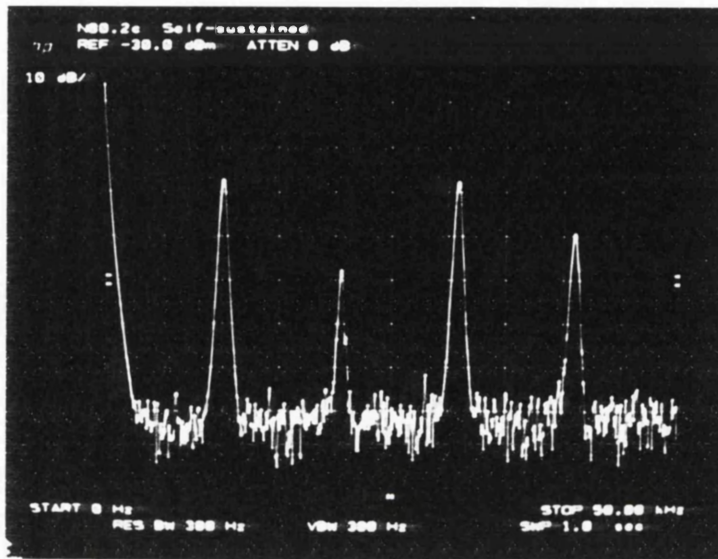

Figure 6.4: Spectrum of reflected light signal from a self-excited microresonator, frequency range 0 to 50KHz, amplitude 10dB/division.

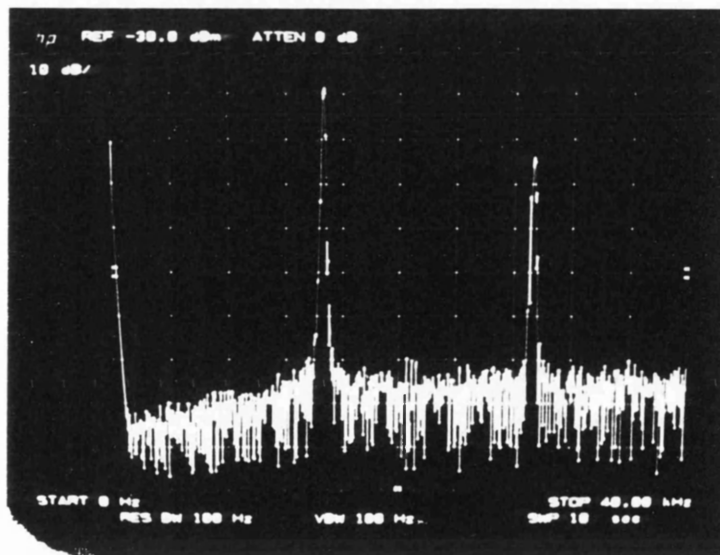

Figure 6.5: Spectrum of reflected light signal from a self-excited microresonator, frequency range 0 to 40KHz, amplitude 10dB/division.

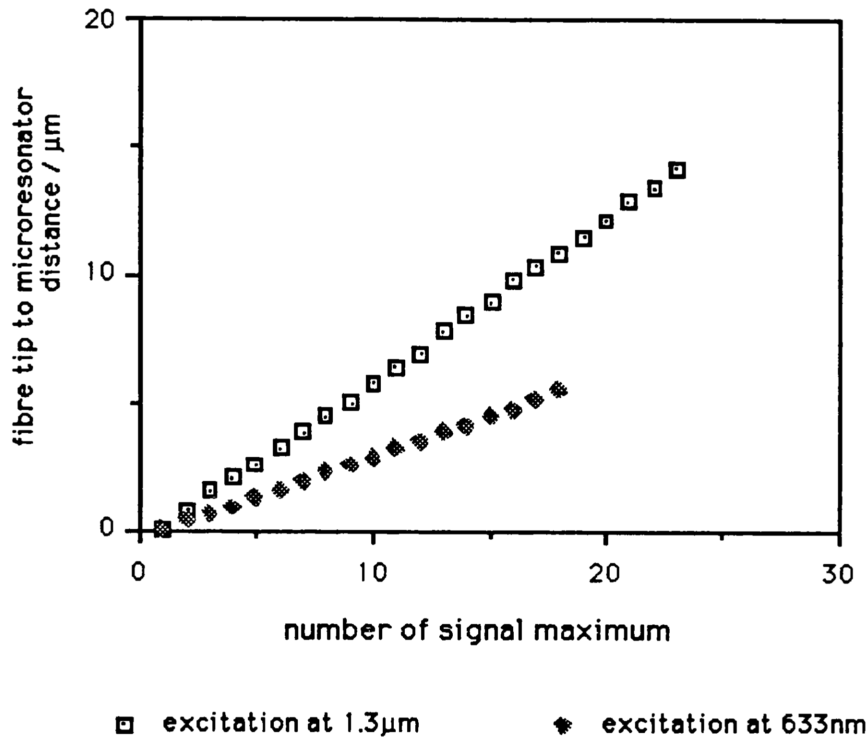

Figure 6.6: Distance between signal maxima.

A similar series of measurements were carried out for a beam excited by an unmodulated source at 633nm, and a similar plot corresponding to this case is shown on the same figure. In this case the mean distance between maxima was 320nm.

The maxima and minima observed were defined much more sharply for the monomode (1.3µm) system. In this case as the fibre tip was moved away from the position of a signal maximum the signal became unstable and distorted, eventually vanishing. This is expected because, as we have shown in Section 6:2 of this Chapter, self-excited vibrations are only possible at certain positions on the absorption curve shown in figure 6.2. An oscilloscope trace of the signal at a position of maximum response is shown in figure 6.7. The beam was then moved away from the fibre end through a distance of approximately 200nm. An oscilloscope trace of the signal at this position is shown in figure 6.8.

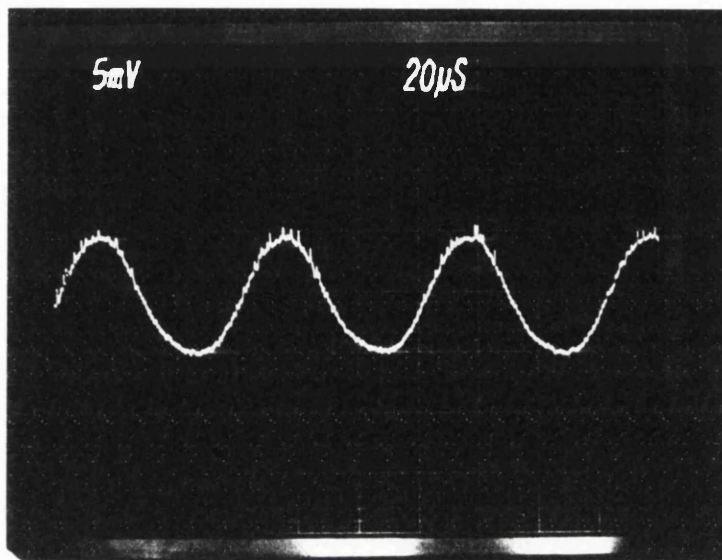

Figure 6.7: Reflected signal from self-excited microresonator at a position of maximum response, timebase 20µsec/division.

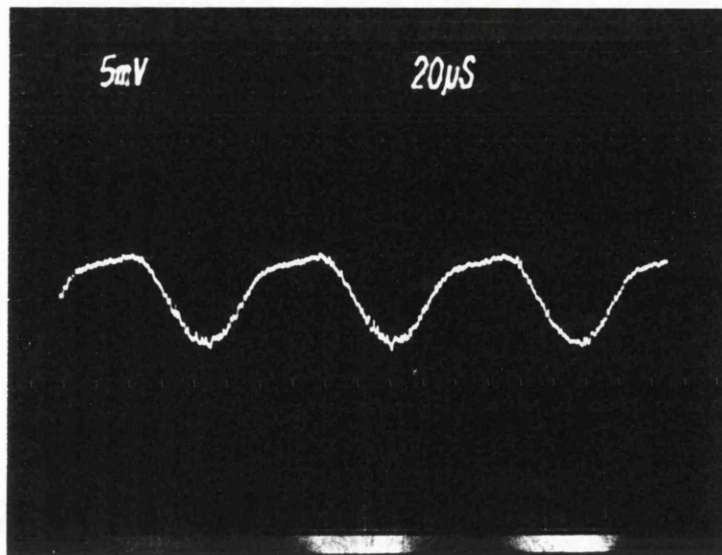

Figure 6.7: Reflected signal from self-excited microresonator near a position of maximum response, timebase 20µsec/division.

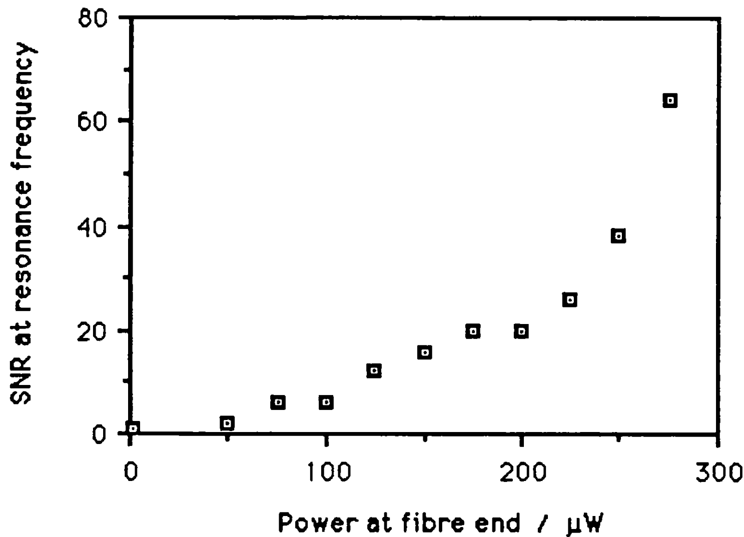

Figure 6.9: Signal magnitude against optical power at 1.3μm for a self-excited device.

The variation of SNR at the resonance frequency of a similar beam with the optical power at the fibre end was also measured and is shown in figure 6.9. It can be seen that above 200μW the signal magnitude increases rapidly with power.

We note here that experimental observations of a silicon micororesonator pressure sensor have recently been reported elsewhere [6]. The system used for this work was a bulk optical one, but it built on some of the results described in this chapter to show that self-excited vibrations could be sustained in metal-coated silicon beams in the same way as we have described here.

6:3.3 Temperature variation of frequency

The variation in microresonator response with temperature was also investigated using different strips with similar dimensions. The variation of resonance frequency with temperature is shown in figure 6.10. Over the range of temperatures used, the variation is linear. The temperature coefficient of resonance frequency was measured from the graph to be 0.20KHz / °C ±0.01KHz / degC, or 0.44% / °C. The SNR remained constant over this temperature range.

This strip was also examined using a modulated optical source to excite vibrations, as described in Chapter 4, Section 4:2.1. The temperature variation of the resonance frequency was measured for the beam using the two-source system described in Chapter 5, Section 5:3, to be 0.45% / °C. This is the same temperature variation of resonance frequency, to within experimental error, as measured for the self-excited beam.

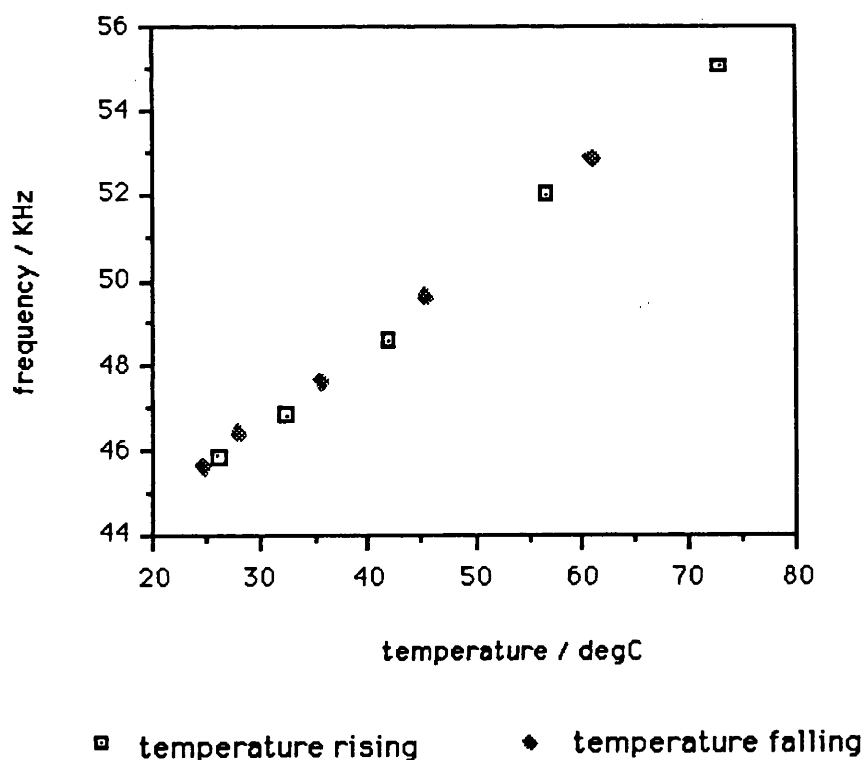

Figure 6.10: Variation of resonance frequency with temperature.

6:3.4 Multiplexing of self-excited devices

In a further experiment, two microresonators were self-excited on the same fibre network. The fibre-optic system used is shown in figure 6.11.

These microresonators were of the same material composition and similar geometry to those described above, but were of different thicknesses. The resonance frequencies of these devices were measured separately using the system shown in figure 6.7 with a spectrum analyser resolution bandwidth of 300Hz to be 22KHz and 30KHz. The different resonance frequencies allowed the two return signals to be distinguished when the multiplexing system shown in figure 6.11 was used. The combined response was displayed on the spectrum analyser and is shown in figure 6.12 and, over a wider frequency range, in figure 6.13. On this second trace signal peaks can be seen at the two resonance frequencies and also at double these frequencies, in line with the results described above.

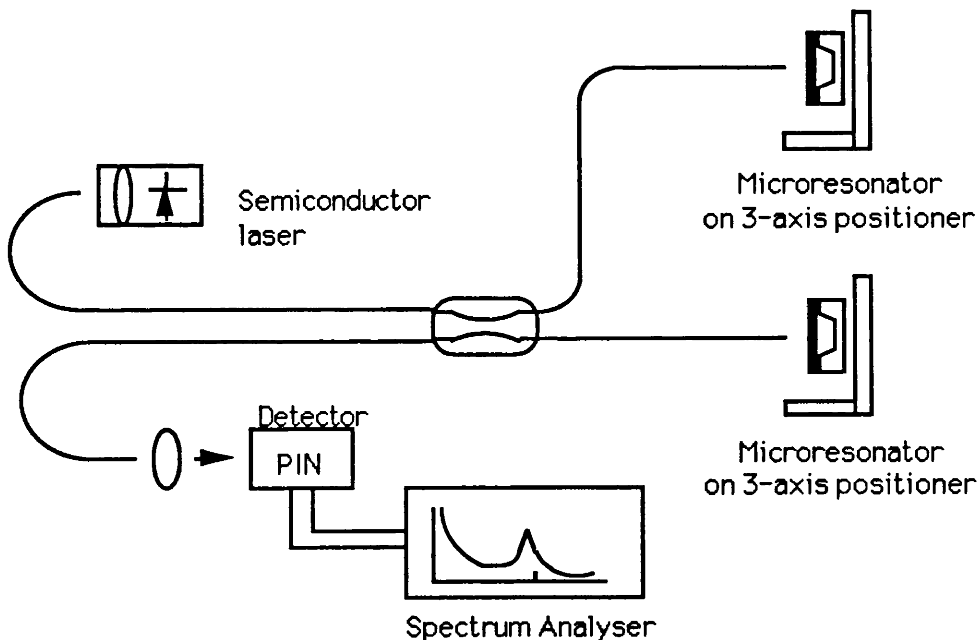

Figure 6.11: Single-source system with two microresonators.

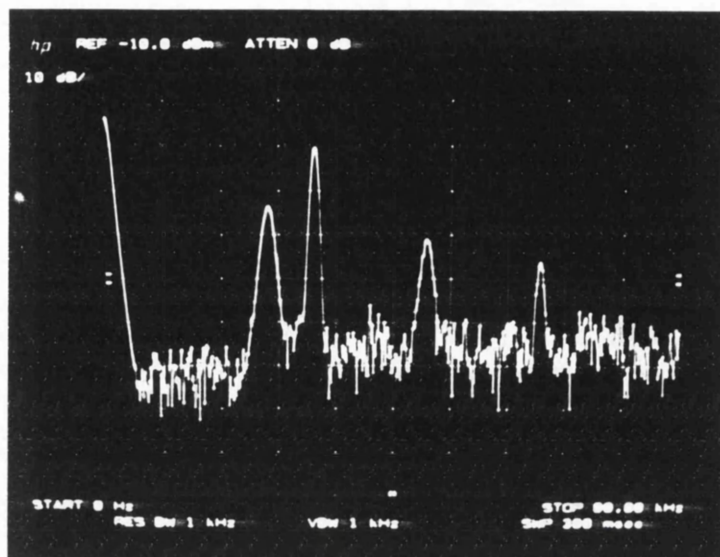

Figure 6.12: Reflected signal from two multiplexed self-excited microresonators, frequency range 0 to 40KHz, amplitude 10dB/division.

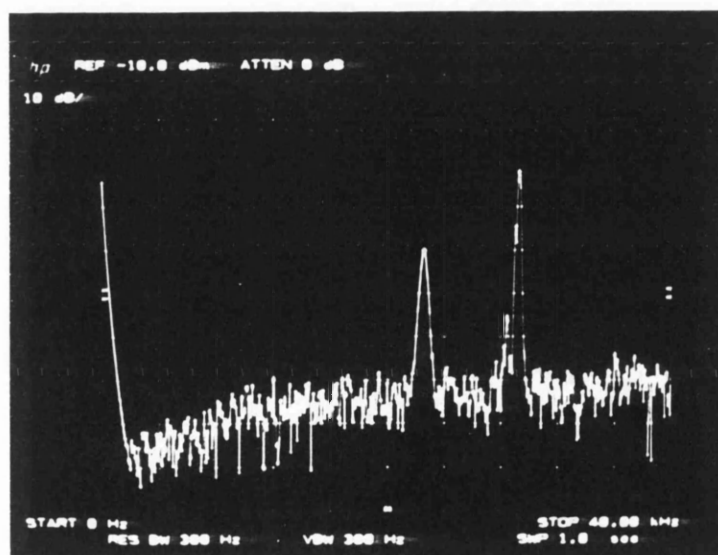

Figure 6.13: Reflected signal from two multiplexed self-excited microresonators, frequency range 0 to 80KHz, amplitude 10dB/division.

3.4 Conclusions

We have proposed a possible mechanism for sustaining fibre-optic microresonators in resonant vibrations using a single unmodulated source. This enables a significant reduction in system complexity to be made. We have derived conditions for sustaining these vibrations, and shown that these conditions may be satisfied using a simple fibre system with an optical power incident on the resonator beam of approximately 200μW.

Self-excitation of metal-coated silicon dioxide microresonators has been demonstrated using an all-fibre system. Two types of optical excitation have been investigated, using single- and multimode optical sources. The signal-to-noise ratio has been considerably improved by using thinner paddle beams and by increasing the incident optical power. The predicted relationship between the distance between the fibre end and the metal-coated surface of the resonator beam and the response signal maxima is observed both using light at 633nm and at 1.3μm.

The temperature variation of the resonance frequency of a self-excited beam has been shown to be consistent with results obtained using a modulated optical activation source. A temperature coefficient of resonance frequency of 0.44% / ^{0}C has been measured.

The suitability of these devices for multiplexing has been shown experimentally for the first time.

References for Chapter 6

1. A.Yariv; "Optical Electronics"; CBS College Publishing, New York, 1985
2. R.M.Langdon and D.L.Dowe; "*Photoacoustic oscillator sensors*"; Proceedings of the SPIE Conference on Fibre Optic Sensors II, The Hague, 1987, pp867-93
3. N.A.D.Stokes *et al.*; "*Self-Excited Vibrations of Optical Microresonators*"; Electronics Lett., Vol.24, pp777-778, 1988
4. N.A.D.Stokes *et al.*; "*Self-Excitation in Fibre-Optic Microresonator Sensors*"; Conf. on Solid-State Sensors and Actuators (Transducers '89), Montreux, June 1989
5. N.A.D.Stokes *et al.*; "*Study of Optical Self-Excitation in Micromachined Resonator Sensors*"; Sensors and Actuators, vol.A, no.21, pp369-372, 1990
6. L.M.Zhang *et al.*; "*Optically Powered Silicon Microresonator Pressure Sensor*"; Springer Proceedings in Physics, vol.44, pp470-477, 1989

CHAPTER 7

SUMMARY, CONCLUSIONS AND RECOMMENDATIONS

This project has set out to examine the behaviour and performance of an important and novel type of device. We have demonstrated that fibre-optic microresonators may be exploited as sensors which combine the advantages both of fibre-optic sensors and of resonators. As such they offer potential performance advantages unique to this type of device.

The availability of batch fabrication facilities for micron-scale silicon devices throughout the electronics industry, and the mass-production of high quality optical fibre precipitated by the communications industry, allow the possibility of cheap, reliable quality sensors of this type. Although concentrated development work is needed to produce marketable devices, fibre-optic microresonators have an exciting future.

Previous work demonstrated that vibrations of microbeams could be activated and detected optically [1]. The work carried out as part of this study has built on this beginning, extending it in several directions.

A range of different microresonator designs have been examined, with a view to optical activation and detection of vibrations. The devices were variously shaped beams of metal-coated silicon or metal-coated silicon dioxide fabricated on silicon wafers. The fabrication of the silicon dioxide structures was carried out in-house as part of this work.

A number of features were observed and measured, which were subsequently shown to affect the device performance. These include an overhang of the beam substrate material around the etched pit in the silicon wafer. At the beam ends this overhang took a complex shape called webbing.

In addition the silicon dioxide beams fabricated in-house were observed to be

deflected from the surface plane of the silicon wafer. This is consistent with the effect of a compressive stress, induced in the oxide during the thermal growth process, and relieved when the silicon beneath the beams is removed. In line with prediction, no such deflection was observed for the silicon beams. The difference between silicon and silicon dioxide microresonators influences their suitability for different sensing applications.

The physical process of optical activation of microresonator beams such as those fabricated for this project was modelled analytically for the first time. This analysis showed that a modulated optical intensity incident on the beam surface from a fibre end positioned within a few microns would set up a periodically varying temperature distribution along the beam length. The resulting thermal expansion of the beam would then cause mechanical vibrations. An expression for the quality factor of resonant vibrations was derived, and from this the amplitude of vibrations at the mechanical resonance frequencies of the microresonator beams which could be excited was estimated to be approximately 100nm. The analysis is expected to be a useful tool in the design of new sensors of this type. An analysis using similar methods to investigate the behaviour of larger optically excited microresonators has recently been reported elsewhere [2], yielding comparable results.

It was not possible to predict the absolute resonance frequencies of the beams fabricated, since these are dependent on the residual stresses induced by the fabrication processes and whilst such stresses may be measured and accurately predicted for devices batch-produced using reliable high-quality equipment, it is unrealistic to expect the integrity of in-house fabrication to match that of commercial batch-production. In addition, the behaviour of the beams of these dimensions is also critically dependent on their geometrical properties. However it was possible to draw general conclusions from the behaviour of the microresonators.

The stresses in a composite deflected beam were analised for the first time as part of this project. We predicted, in opposition to the standard theory of straight beams, that an increase in metal coating thickness on a silicon dioxide beam may cause a decrease in resonance frequency.

A monomode fibre-optic system was developed in order to test the hypotheses suggested by the fabrication and modelling work, and to enable an examination of the resonators experimentally. Initially the optical activation of metal-coated silicon microresonators and metal-coated silicon dioxide microresonators was demonstrated.

It was possible to excite several modes in many of the microresonators, and by comparing the frequencies of these different modes it was shown that, as had been suggested by consideration of the webbed beam ends, more modes could be excited than would be expected if the beam ends were clamped or pinned in a conventional manner. Both metal-coated silicon beams and metal-coated silicon dioxide beams examined exhibited this behaviour. However the resonance frequencies remain widely spaced. No uncertainty due to mode switching is therefore expected to interfere with practical devices of this type.

Variation of resonance frequency with beam length was examined, and the relationship was shown to fit the standard theory used for macrostructures which has been developed elsewhere [3]. The variation of frequency with metal thickness on a thermally-grown silicon dioxide beam was also examined and found to support the results of the analysis of the deflected beam which we had derived. This is in contrast to the standard relationship expected for silicon (straight) beams. The quality factors were considered and found to depend on frequency, and on metal thickness.

The effects of an applied pressure difference across the device wafer and of a change in temperature were predicted by analysis and then measured both for silicon and for silicon dioxide devices using the fibre-optic system.

Shifts in frequency with applied pressure of the order of 5% per bar were calculated for the silicon beams, and it was predicted that the sensitivity could be increased significantly by wafer thinning. These predictions were supported by experimental results. It is predicted that the sensitivity could be increased to approximately 0.5% per millibar by careful device design. The results and analysis of the effect of prssure on silicon devices are confirmed by independent work carried out by Thornton *et al.* at Strathclyde University [4]. They reported a pressure sensitivity of similar micoresonator device, activated using a bulk optical system, of 0.027% per millibar.

Shifts in frequency with applied pressure for silicon dioxide beams, which had not been investigated elsewhere, were expected to be significantly lower because of the beam deflections, and this hypothesis was also supported by the experimental results. It may therefore be concluded that further work on microresonator pressure sensors should concentrate on silicon devices, and that such sensors would offer significant advantages over the current alternatives. In particular they exhibit immunity to elctromagnetic interference effects, and offer a solution to the problem of miniaturisation. The miniaturisation of currently used electrically powered resonators is limited by the size of the resonator element itself, whilst fibre-optic pressure sensors have been based reflective pressure membranes and use fibre bundles [5]. The demonstration of the pressure sensitivity of fibre-optic microresonators is expected to be the beginning of a significant amount of work on fibre-optic microresonator pressure sensors.

Further analysis of the deflected metal-coated silicon dioxide beams showed that the temperature sensitivity of the resonance frequencies of such resonators would depend critically on the metal and oxide thicknesses. This was supported by experiment, and the temperature sensitivities of the resonance frequencies of both silicon and silicon dioxide beams were measured. It is suggested that, since their sensitivity to pressure changes is negligible, the oxide devices are more suitable in temperature sensing applications. The low pressure sensitivity of oxide beams may also be of potential advantage where epoxy bonding is an attractive method of attaching the sensor structure to the optical fibre probe, since in a silicon device such a process has been shown to induce additional residual stresses which will affect the performance.

The principal sensing applications are the measurement of pressure and the measurement of temperature. There is considerable demand for a range of novel pressure sensors, whilst a more specialist demand exists for temperature sensors operating in hostile environments. The different devices investigated here show a suitability for separate markets. This is particularly significant in view of the need for sensors which respond to a specific measurand. Other sensors, particularly fibre-optic intrinsic sensors, suffer from problems of cross-sensitivity.

Considerable development work remains to be done to optimise performance and

produce prototype sensors for these applications. This includes consideration of methods for the attachment of the microfabricated sensor head to the fibre, and some work on this has been carried out based on some of the results of this project [6].

The amplitude of vibrations was shown to be of the same order as the spatial period of interferometric fringes which could be set up by an optical beam of steady intensity between the fibre end and the strip surface. It was suggested that not only detection but also activation of vibrations may be possible by using these fringes as a source of temporal intensity modulation.

The work described on the two-source fibre-optic system was the first to demonstrate fibre-optic silicon and silicon dioxide microrsonators. We also suggested that microresonator vibrations could be excited using a single, unmodulated, optical source. This might be accomplished by using the spatially varying intensity distribution set up between the fibre end and the micoresonator surface, as proposed earlier. Such a system was designed and the self-excitation of metal-coated microresonators demonstrated for the first time. The effect of temperature on resonator operation was also investigated. In this way a self-excited temperature sensor was demonstrated.

Self-excited sensors also allow for a simple multiplexing system to be set up. The multiplexing of two microresonator devices using a single optical source was demonstrated. Further work is recommended to establish that these important advantages can be exploited in a practical system. Already, building on work described as part of this project, a self-excited optically powered silicon microresonator pressure sensor has been demonstrated elsewhere [7].

To conclude, we have helped to show that fibre-optic microresonators are an attractive option for a range of applications, conveniently exploiting the advantages both of fibre-optic sensors and of resonator sensors as described in Chapter 1. Further, we have proposed and demonstrated a unique multiplexing method for these sensors. We expect silicon dioxide devices to fill a specialist niche in the temperature measurement market. We also expect extensive effort in the future to be directed at the optimisation of silicon devices in two directions. The first of these is that of

cheap, robust and disposable sensors which can be fixed using a fibre-optic connector onto the associated unit of instrumentation which will include the optical components. The second is that of very reliable and accurate sensors which can uniquely cope with harsh environments or demanding specifications. The work undertaken in this project indicates that fibre-optic microresonators have the potential to meet these requirements.

References for Chapter 7

1. S.Venkatesh *et al.*; "*Optically Activated Vibrations in a Micromachined Silica Structure*"; Electronics Lett., Vol.21, pp315-317, 1985
2. K.T.V.Grattan *et al.*; "OPtically Powered Sensors Based on Resonant Structures: Mathematical Analysis"; SPIE Vol.949, Fibre Optics 1988, pp152-161
3. S.P.Timoshenko *et al.*; "Vibration problems in Engineering"; John Wiley and Sons, 1974
4. K.E.B. Thornton *et al.*; "*Novel Optically Excited Resonant Pressure Sensor*"; Electronics Lett., Vol.24, pp 573-574, 1988
5. L.H.Lindström; "*Miniaturized Pressure Transducer Intended for Intravascular Use*"; IEEE Trans. Biomedical Eng., BME-17, pp207-219, 1970.
6. W.K.Liu; "Si-Silica Fibre Bonding Investigations"; M.Sc. Thesis submitted to the University of London, 1987, unpublished
7. L.M.Zhang *et al.*; "Optically Powered Silicon Microresonator Pressure Sensor"; "Springer Proceedings in Physics, Vol.44: Optical Fibre Sensors", ed. H.J.Arditty, J.P.Dakin & R.Th.Kersten, Springer-Verlag Berlin, Heidelberg, 1989, pp470-477

APPENDIX A: Materials data

The following is a tabulation of the dataused for numerical calculations but not included in the main body of the text of this thesis.

Material:	Silicon	Silicon dioxide	Gold	Aluminium
Young's modulus (E) / 10^{10}Pa:	19	7	8	7
Density (ρ) / 10^3kgm^{-3}:	2.3	2.2	19.3	300
Thermal conductivity (k) / Wm^{-1}K^{-1}:	157	0.22	300	220
Thermal expansivity (α) / 10^{-6}K^{-1}:	2.3	0.4	14	24
Specific heat capacity (C) / Jkg^{-1}K^{-1}:	750	750	130	900

Viscosity of air (η_{air}): 1.8 x 10^{-5} Pa sec.

APPENDIX B: Publication List

The following is a list of the publications, including conference procedings, arising out of this Ph.D, in chronological order.

1. N.A.D.Stokes, R.M.A.Fatah and S.Venkatesh; "*Self-Excited Vibrations of Optical Microresonators*"; Electronics Lett., Vol.24, pp 777-778, 1988
2. R.M.A.Fatah, N.A.D.Stokes and S.Venkatesh; "*Activation of Silicon Micromechanical Resonators in Fibre Optic Systems*"; European Fibre Optic Communication and Local Area Networks Exposition, Amsterdam, June 1989
3. N.A.D.Stokes, R.M.A.Fatah and S.Venkatesh; "*Self-Excitation in Fibre-Optic Microresonator Sensors*"; Conf. on Solid-State Sensors and Actuators (Transducers '89), Montreux, June 1989
4. R.M.A. Fatah, N.A.D.Stokes and S.Venkatesh; "*All-Fibre-Optic Microresonator Sensor System*"; Symposium on Sensors and their Application, Kent, Sept.1989
5. N.A.D.Stokes, R.M.A.Fatah and S.Venkatesh; "Study of Optical *Self-Excitation in Micromachined Resonator Sensors*"; Sensors and Actuators, vol.A, no.21, pp369-372, 1990
6. N.A.D.Stokes and R.M.A. Fatah; "*Optical Activation of Silicon Micromechanical Resonators: End Conditions*"; Electro-Optics and Laser int. conf., Birmingham, March 1990

The following has been submitted:

7. R.M.A. Fatah and N.A.D.Stokes; "*Electrostatic Activation of a Micromechanical Resonator*"; submitted to European Fibre Optic Communication and Local Area Networks Exposition, Munich, June 1990

Errata

Page 13, line 4, to read: "...using an interferometric technique"

Page 27, line 2, to read: "...low etch rate planes intersect the wafer surface at 90°...".

line 7, to read: "...(111) etch planes **normal** to the wafer surface plane..."

Page 45, line 3, to read: "...specified in section 2:4.1 of this chapter..."

line 13, to read: "class **100/10,000** clean-room environment..."

Page 53, line 9, to read: "where M_b and M are respectively..."

Page 59, eqn.{3.18}: here β is the fraction of incident intensity absorbed.

Page 61, line 8: "figure 2.3" to read "figure 3.4"

Page 62, Table 3.1: "$u_{therm.}$" to read "$z_{therm.}$"

Page 73, line 8: "...the **net** stress is compressive..."

Page 77, Reference 4: authors to read: "C.R.**Petts** & H.K.Wickramasinghe"

Page 94, Table 4.4, line 2 to read: " 2 0.23 2.33 0.014 "

Page 96, line 13, to read: "is similar for all **four** batches of devices."

Page 97, Figure 4.7, first line of caption to read:

"Resonance frequencies of SiO_2/Al simple 185μm beams"

Page 97, Figure 4.8, first line of caption to read:

"Resonance frequencies of SiO_2/Al simple 185μm beams"

Page 103, Table 4.9, line 2, column 7, to read "80" [*not* "8"]

Page 111, line 2: References [10,11] refer to Chapter 1 references [10,11].

Page 142, line 5, to read: "**increase** with the slenderness ratio..."

Page 143, Table 5.1, second line of caption to read: "...for some **microresonator**"

Page 157, line 6, to read: "...were first observed in June **1987**..."

Page 175, Table, line 2, column 4, to read "2.7" [*not* "300"]

Addendum

The following paragraphs are added to Chapter 2:

We have described in this chapter that all the silicon dioxide beams examined are deflected because of the release of fabrication-induced compression in the silicon dioxide. This can be described as a buckling of the beams under the compressive load. The critical conditions for this buckling are dependent not only on the load, but also on the beam's dimensions and end conditions.

For a beam clamped at both ends, Euler buckling will occur at a critical stress $\sigma_{crit.}$ if [39]:

$$\sigma_{crit.} = \frac{\pi^2 E a^2}{3 L^2} \qquad \{2.1\}$$

We put $\sigma_{crit.} = 2.5 \times 10^8$ Nm^{-2} (see section 2:3 of this chapter), and $a = 0.5\mu m$. Then the beam will buckle if

$$L > 15\mu m.$$

The beams examined are of length greater than 80μm, and we therefore expect buckling in all cases, as has been observed.

It is noted that although the stress in the beams has been mostly relieved, they remain in a buckled state and will therefore deflect more readily in the presence of any further axial stress. There is however no danger of plastic deformation since the compressive stress is substantially below the plastic yield stress of the silicon dioxide, so that transverse elastic vibrations can occur, as described in subsequent chapters, about the equilibrium position of the deflected beam.

Reference

39. S.Timoshenko; "Theory of Elastic Stability", McGraw-Hill, New York, 1936